PHYSICAL AND NUMERICAL MODELLING

OF 3-D FLOW AND MIXING PROCESSES

IN CONTACT TANKS

A thesis submitted to Cardiff University

In candidature for the degree of

Doctor of Philosophy

by

William Bonino Rauen

B.Sc., M.Sc.

Division of Civil Engineering, Cardiff School of Engineering

Cardiff University

August 2005

UMI Number: U584730

UMI

Dissertation Publishing

ProQuest

PHYSICAL AND NUMERICAL MODELLING OF 3-D FLOW AND MIXING PROCESSES IN CONTACT TANKS

William Bonino Rauen

ABSTRACT

The flow pattern in contact tanks (CTs) can exhibit complex hydrodynamic and mixing processes, typically with the occurrence of recirculating flow and dead zones, shear and wall generated turbulence, as well as regions with relatively low horizontal velocities and others with fairly high vertical accelerations. The characterisation of these phenomena is of paramount importance for an integrative understanding of their effects on the performance of CTs, demanding the use of sophisticated investigative techniques, such as the direct assessment of the velocity field and use of appropriate and refined numerical schemes. Nonetheless, thorough comparisons of the performance of CTs against the predictions of complex three-dimensional (3-D) numerical hydrodynamic and solute transport models have yet to be reported.

A physical and numerical investigation of the 3-D hydrodynamic and mixing processes in contact tanks was undertaken in this study. Physical experimentation has been carried out for various configurations of a prototype CT, providing data for the validation of numerical model results. These included velocity measurements with an Acoustic Doppler Velocimeter, as well as assessments of solute transport processes by using tracer techniques. A 3-D Computational Fluid Dynamics model has been developed, based on the finite volumes method and using a low Reynolds number k-ε turbulence model, in addition to a depth-averaged eddy viscosity approach. The Reynolds-averaged Navier-Stokes equations have been discretised using the SIMPLER algorithm and solved in a line-by-line fashion for a non-uniform mesh configuration. The parameter C_μ for the k-ε model has been calculated as a function of local turbulence quantities.

A sensitivity analysis of the predicted results has been undertaken for the variation of the Schmidt number and type of turbulence model. The numerical model predictions have been validated against analytical and empirical results for benchmark flow problems, as well as for hydrodynamic and solute transport data from various prototype CTs. An encouraging agreement has been observed between the data and corresponding numerical model predictions.

Keywords: Computational Fluid Dynamics, Numerical Modelling, Physical Modelling, Contact Tanks, Hydrodynamics, Hydraulic Efficiency, Solute Transport, Mixing Processes, Finite Volume Method, Acoustic Doppler Velocimetry, Tracer Techniques

ACKNOWLEDGEMENTS

To Esther,

FOR HER UNCONDITIONAL LOVE AND SUPPORT

Para Esther,

POR SEU AMOR E SUPORTE INCONDICIONAIS

CONTENTS

Chapter 3:   Experimentation Methods 34

Chapter 4:   Governing Equations 57

LIST OF FIGURES

NOTATION

a	coefficient of discretised governing equation
A	cross-section area
A_{in}	inlet cross-section area
b	bottom face in discretisation mesh; mass source in discretised equation
B	bottom cell in discretisation mesh; width of channel
c	turbulent fluctuation of concentration; Chezy coefficient
C	mean concentration
C_0	average initial tracer concentration
C_μ, $C_{1\varepsilon}$, $C_{1\varepsilon}$	coefficients of the k-ε turbulence model
d	dispersion number
D	generalised diffusion coefficient
D_L	longitudinal dispersion coefficient
e	east face in discretisation mesh
E	east cell in discretisation mesh
$E(\theta)$	normalised tracer concentration
f_μ, f_1, f_2	damping functions of low Reynolds number k-ε models
f_e	interpolation factor for interface viscosity
F	mass flux term
$F(\theta)$	normalised accumulated tracer concentration
g	acceleration of gravity
G	turbulence generation term
H	depth of flow
i, j	direction in Cartesian tensor notation

k	turbulent kinetic energy
k^+	normalised turbulent kinetic energy
k_{in}	inlet turbulent kinetic energy
L	length of flow; width of compartment
M	injected tracer mass
Mo	Morrill index
n	north face in discretisation mesh; Manning's resistance coefficient
N	north cell in discretisation mesh
N_x, N_y, N_z	number of grid points in the corresponding Cartesian direction
P	static pressure; centre cell in discretisation mesh; Peclet number
P^*	starred-pressure in SIMPLER algorithm
P'	pressure correction in SIMPLER algorithm
q_{out}	flow rate at outlet section
Q	flow rate
Q_h	flow rate per unit depth
Re	bulk Reynolds number
Re_t, R_t, R_y	turbulence Reynolds numbers
R_{hin}	inlet hydraulic radius
REC	tracer mass recovery index
s	south face in discretisation mesh
S	generalised source term; south cell in discretisation mesh
S_c, S_p	source term coefficients
t	time; top face in discretisation mesh
T	top cell in discretisation mesh; theoretical residence time in basin
u	velocity in discretised momentum equation
u^*	starred-velocity in SIMPLER algorithm

$\hat{u}$	pseudo-velocity in SIMPLER algorithm
u_i, u_j	turbulent fluctuation of U_i, U_j
U	longitudinal / streamwise velocity component
U^+	normalised streamwise velocity
U_0	bulk velocity
U_f	friction velocity
U_i, U_j	velocity component in governing equation in Cartesian tensor notation
U_{in}	inlet bulk velocity
U_m	maximum velocity of a velocity profile
V	lateral velocity component
V_w	wetted volume of basin
w	west face in discretisation mesh
W	vertical velocity component; west cell in discretisation mesh
x	longitudinal / streamwise coordinate of the Cartesian system
x_i, x_j	coordinate in governing equation in Cartesian tensor notation
y	lateral coordinate of the Cartesian system; distance to nearest wall
y^+	normalised distance to nearest wall
z	vertical coordinate of the Cartesian system
δ_{ij}	Kronecker delta
δ_x	distance in computational grid
Δt	time step
$\Delta x, \Delta y, \Delta z$	mesh spacings in the corresponding Cartesian direction
ε	dissipation rate of turbulent kinetic energy
ε^+	normalised dissipation rate

ε_{in}	inlet dissipation rate
ϕ	generalised variable
Γ	turbulent mass diffusivity
κ	von Kármán constant
λ	molecular diffusivity
μ	dynamic viscosity
ν	effective viscosity
ν_l	kinematic viscosity of fluid
ν_t	eddy viscosity
θ	normalised time
θ_i, θ_{10}	short-circuiting indicators
ρ	specific mass of fluid
σ^2	dispersion index; mixing indicator
σ_{ADV}	uncertainty of ADV measurements
σ_c	deviation coefficient
$\sigma_k, \sigma_\varepsilon$	constants of the k-ε turbulence model
σ_t	turbulent Schmidt number
$\sigma_u, \sigma_v, \sigma_w$	error of ADV measurements of velocity turbulent fluctuation
$\sigma_U, \sigma_V, \sigma_W$	error of ADV measurements of mean velocity

Chapter 1

Introduction

1. INTRODUCTION

Access to safe potable water has become an issue of major worldwide concern, even though the average demand for water per inhabitant does not appear to have changed significantly in recorded history. For instance, the daily average per capita consumption of water reported for the city of Rome in AD 97 was 144 litres (Droste, 1997), while for present day consumption the estimated worldwide figure is around 250 litres/person/day for urban areas (WHO/UNICEF, 2000). The average per capita demand in rural areas is generally lower, however, by 2007 more than 50% of the world's population will be living in urban areas, much of which will be in developing countries (UN, 1997). Due mainly to population growth, pollution, climate change and political inertia, in 2025 two thirds of the world's population could be living in water scarce areas, while by 2050 an estimated 7 billion people in 60 countries at worst could face water scarcity, and at best 2 billion people in 48 countries (UNESCO, 2003).

In the past, good quality water was generally available to meet demand with minimal treatment being required. However, since mainly the second half of the 20th century an unprecedented increase in water consumption levels has necessitated considerable advancements to be made in the treatment process of water for consumption (Binnie et al., 2002).

Worldwide, the standards for drinking water can differ substantially, with the quality of supply water ranging from a wholesome level directed by strict regulations in

developed countries, to only meeting the basic international guidelines (WHO, 2004) in less-developed communities.

Likewise, the requirements for drinking water treatment processes vary depending upon the characteristics of the raw water. Among the impurities commonly found in raw water are pathogenic micro-organisms, which are potentially transmitters of waterborne diseases. The inactivation of such agents in the water destined for human consumption is known as disinfection, and is generally a key stage of every water treatment process (Gray, 1999).

The disinfection of drinking water generally takes place in contact tanks. Contact tanks (CTs) are typically rectangular basins where baffles can be introduced in order to increase the length-to-width ratio of flow, for which a channel or pipe is used as the inlet device and an overflow weir is installed at the outlet. A typical contact tank can vary considerably in size, from a relatively small unit such as the 16m x 7.5m x 4.8m Embsay Contact Tank (Teixeira, 1993) for a small community, to much larger units such as the 91m x 46m x 2.5m Elan Contact Tank (Thayanithy, 1984) to attend a larger population. According to the current British Standard on disinfection, the objective of a contact tank is "to maintain the microorganisms in the effluent stream in intimate contact with the disinfecting chemical for the required period" (BSI, 2003). Typical contact times of 15min or more generally give sufficient time for the inactivation of micro-organisms to take place in a contact tank.

As shown by White (1998), "historically chlorine has been the world's most used disinfectant". Chlorination of drinking waters has become a worldwide practice, since shortly after the chemical was first used as a germicide in the 19th century. In spite of the discovery in the 1970s of health hazardous chlorination by-products (CBP), other technologies have been developed and applied for disinfection purposes, such as ozonation, ultraviolet radiation and ultrasonics, but these technologies have not generally replaced "chlorine's near universal use" (White, 1998), either as the sole disinfectant in a water treatment plant or in conjunction with other technologies. It is generally accepted that the advantageous use of chlorination greatly surpasses the risks to health associated with the CBP formation (WHO, 2004) and, thus, the chlorine contact tank is, according to White (1998), "an integral part of the water treatment process".

Reactions between chlorine compounds and microorganisms are very complex and time-dependent (White, 1998). Thus, it is of paramount importance to optimise the hydraulic behaviour of CTs, aiming to (Teixeira, 1993): i) maximise the level of microbial inactivation, i.e. maximise the disinfection efficiency; ii) minimise operational costs, e.g. with reagents; and iii) minimise the formation of CBP. The ideal performance of CTs is regarded as being achieved when all of the molecules passing through the tank have near equal residence times, for an idealised flow pattern known as plug flow.

With regard to the design of CTs, the British Standard advises: "A disinfection contact tank should be designed to avoid short circuiting and should be as near to a plug

flow system as is practicable. It will normally be a pipeline or a serpentine chamber"
(BSI, 2003).

Therefore, the hydraulic optimisation of CTs requires mitigating the occurrence of short circuiting (and mixing) in the flow chamber, so that the flow pattern tends towards plug flow and the tank's hydraulic efficiency is optimised. As pointed out by Teixeira (1993), the hydraulic efficiency is "a measure of the degree of similarity between the characteristics of the actual and ideal flow for a given unit". The CT geometry, inlet and outlet configuration, and the use and location of baffles and diffusers have all been shown to play a key role in the establishment of the actual flow structure and patterns within contact tanks.

In connection with the hydraulic efficiency of CTs, Teixeira (1993) comments on important insights that have been achieved with the use of tracer techniques in "black box" assessments of CTs. However, more sophisticated investigative techniques have been required in order to allow detailed assessments of the flow through characteristics in CTs to be undertaken. Such techniques can involve direct velocity field measurements, – e.g. by using laser or acoustic anemometry, and/or by the use of numerical models of the hydrodynamic and mixing processes in CTs. Nonetheless, the availability of reliable hydrodynamic data for use in the verification of obtained numerical model predictions is limited and, hence, thorough comparisons of the performance of CTs against the predictions of complex three-dimensional (3-D) numerical hydrodynamic models have yet to be reported.

In connection with this lack of application of complex 3-D numerical models to the design of CTs, it is known that the relatively high vertical accelerations normally occurring in such flows generally require the numerical model to be non-hydrostatic in nature, i.e. based on solving the full 3-D governing equations, in order to allow for a hydrodynamic pressure distribution. Furthermore, peculiarities of the flow in CTs, such as the reported occurrence of recirculating flow and dead zones, shear and wall generated turbulence, as well as regions with relatively low flow velocities (Teixeira, 1993) demand the use of appropriate and refined numerical schemes.

It was in this context that the main aims of this research study were defined as being: i) to improve our understanding of the hydrodynamic and mixing processes in CTs with complex 3-D flow structures, and using both physical and numerical modelling techniques to analyse these systems; and ii) to develop and test a new, purpose built, fully 3-D numerical model capable of simulating flows in CTs with the characteristics described above, i.e. where the flow regimes span from laminar to transitional and fully rough turbulent flow regimes.

The thesis comprises nine chapters, including this Introduction. In Chapter 2 the literature review encompasses recent advancements in hydraulic and numerical modelling studies of CTs, as well as aspects related to the physical and numerical modelling of contact tanks. In Chapter 3 the experimentation methods and materials used in this study are described. An outline of the mathematical model used to describe the hydrodynamic and solute transport processes in CTs is made in Chapter 4, while the numerical model development is explained in Chapter 5. The physical experimentation

results are presented and discussed in Chapter 6 and in Chapter 7 the numerical model is validated using analytical and empirical results from benchmark flow problems. The application and testing of the numerical model to simulate flow conditions in CTs, with 2-D and 3-D flow models, is discussed in Chapter 8. The main conclusions of this study and recommendations for further research are given in Chapter 9.

Chapter 2

Literature Review

2.1. INTRODUCTION

The literature review included herein provided the basis for the development of this study. Recent research advances in physical experimentation techniques and numerical modelling predictions of processes in Contact Tanks (CTs) are outlined in sections 2.2 and 2.3 respectively. In section 2.4 details are given of the acquisition of velocity and tracer concentration data. Numerical modelling developments are then discussed further in section 2.5.

2.2. ADVANCEMENTS IN PHYSICAL EXPERIMENTATION OF HYDRODYNAMIC AND SOLUTE TRANSPORT PROCESSES IN CONTACT TANKS

Teixeira (1993) undertook a state-of-the-art review of the main CT research advancements thus achieved, reporting on a number of investigations that had been carried out mainly using tracer-based assessments of the hydraulic efficiency of CTs (Louie and Fohrman, 1968; Sawyer and King, 1969; Marske and Boyle, 1973; Kothandaraman et al., 1973; Hart et al., 1975; McNaughton and Gregory, 1977; Trussell and Chao, 1977; Hart and Gupta, 1978; Hart, 1979a; Hart, 1979b; Hart and Vogiatzis, 1982; Sepp, 1981; Thayanithy, 1984; Falconer and Tebbutt, 1986). In some of these studies the improvements in hydraulic efficiency achieved for the tanks have been linked to predictions of the disinfection efficiency for the respective CT (Trussell and Chao, 1977; Hart, 1979a; Sepp, 1981; Hart and Vogiatzis, 1982) by using either batch reaction models, such as the Chick-Watson model (Gyürék and Finch, 1998), or hydrodynamic-kinetic models of chemical reaction engineering (Danckwerts, 1953; Wehner and Wilhelm, 1956; Levenspiel, 1999).

Past studies focused mainly on the influence of a number of geometrical features on the hydraulic performance of CTs. The most important effects were recorded for factors such as the length-to-width ratio of the flow, the inlet configuration and the use of guide vanes and diffusion walls in the contact tanks. Semi-empirical relationships have been developed to aid the design of CTs based on one or a few parameters (Marske and Boyle, 1973; Trussell and Chao, 1977), however, none of these relationships are general enough to include all of the most influential aspects. Further insight in this area has demanded the application of more sophisticated assessment and analysis techniques.

Teixeira carried out direct measurements of the 3-D turbulent flow field in a prototype CT using Laser Doppler Anemometry (LDA), as well as using the conventional approach of hydraulic assessment based on fluorescent tracer techniques (Teixeira, 1993; Shiono and Teixeira, 2000). The unit investigated by Teixeira was a 1:8 prototype of the Embsay Contact Tank operated by Yorkshire Water, and had 8 compartments with an open channel at the inlet.

The LDA characterisation carried out indicated that the mean flow field in the tank had a strongly 3-D character in the first three compartments, in which relatively large regions were occupied by reversing flow structures (Teixeira, 1993). Furthermore, an inlet weir located just upstream of the inlet section to the tank was shown to cause relatively high levels of shear-generated turbulence in Compartments 1 and 2 of the tank.

An assessment of the vertical distribution of the resultant velocities measured in several compartments indicated that the mean flow could be regarded as vertically uniform from Compartment 5 up to the mid-length of Compartment 8. In the second half of this final compartment a 3-D flow field was established due to the outlet weir effects.

Teixeira also investigated aspects related to the magnitude of the reversing flow due to the 3-D effects in Compartments 1 and 2, as well as the flow's mixing characteristics. The author concluded that the inlet design was the main responsible factor for the departure of the flow pattern from plug flow (Teixeira, 1993). In addition, Teixeira found that for the same value of the length-to-width ratio it the longitudinal baffling tended to provide a higher hydraulic efficiency than cross-baffling for that particular tank. This conclusion corresponded to the outcome of a similar investigation carried out by Marske and Boyle (1973).

Stevenson (1995) and Johnson et al. (1998) applied hydrodynamic-kinetic models to estimate the influence of the dispersion number on the disinfection efficiency of a number of CT configurations. Both studies showed that improving the hydraulic performance of a CT beyond a certain level did not significantly increase its overall disinfection efficiency, which indicated that hydraulic optimisation must be considered together with process performance. Trussell and Chao (1977) had derived a similar conclusion, introducing the concept of a "rational design procedure".

Johnson et al. (1998) suggested that the most cost-effective value for the dispersion number was d = 0.02, which was twice the optimal value recommended by Trussell and

Chao. According to Trussell and Chao, the estimated gain in terms of the disinfection efficiency when the dispersion number varied from 0.01 to 0.001 was only 5-6%, while varying the value from 0.1 to 0.01 increased the disinfection by approximately 60%.

Siqueira (1998) and Teixeira and Siqueira (2005) investigated the statistical representativeness of a number of hydraulic efficiency indicators (HEI) found in the literature. Siqueira conducted tracer experiments with model water treatment tanks that provided flow patterns ranging from close to completely mixed flow to tending towards plug flow. Amongst the HEI parameters evaluated, the most suitable short-circuiting and mixing indicators for use in the interpretation of tracer experiments were θ_{10} and σ^2 respectively. The most important feature of the HEI parameters recommended by Siqueira was the fact that their formulations were based on the whole retention time distribution (RTD) curve or, at least, on a considerable section of it. The use of parameters defined based on only one point of the RTD curve was not encouraged as it might induce misleading conclusions due to a relatively low reproducibility (Teixeira and Siqueira, 2005).

However, it has been suggested that the parameter that indicates the start of the tracer passage through a monitoring section, i.e. θ_i, could also be used in situations when quick estimates of the advective effects of the flow are required (Siqueira, 1998). Furthermore, for situations of relatively low mixing levels, i.e. flow patterns tending to plug flow, the author recommended the analysis to be mainly based on the Morrill index (Mo) to evaluate the mixing levels, since in such situations σ^2 is reportedly prone to a relatively high variability (Teixeira and Siqueira, 2005).

Rauen (2001) investigated the effects of scale and experimentation flow rate on the dynamic similitude and estimated disinfection efficiency of undistorted model contact tanks. Fluorescent and saline tracer techniques were deployed, with the analyses being based on the obtained RTD curves and HEI results. A new deviation parameter was proposed for use in the comparative analyses of RTD curves, namely the percentile area deviation (PAD) coefficient. Based on the analyses carried out by Rauen it was found that, for an assessed flow pattern with a relatively high mixing level, i.e. tending to completely mixed, then scale effects were negligible for the range adopted in the study. On the other hand, for plug flow units the short-circuiting and mixing levels tended to increase as the scale factor was increased above 1:16, with the next ratios used being 1:24 and 1:50 respectively. The variation of the experimentation flow rate promoted by Rauen was within the range 50% to 150% of the respective Froudian value for the tanks (Hart and Gupta, 1978; Kawamura, 1991). No significant influence was detected on the short-circuiting and mixing levels in the model tanks due to such a variation.

In the following section the recent progress achieved on the numerical modelling of hydrodynamic and solute transport processes in CTs, as reported in the literature is discussed.

2.3. ADVANCEMENTS IN NUMERICAL MODELLING OF HYDRODYNAMIC AND SOLUTE TRANSPORT PROCESSES IN CONTACT TANKS

Teixeira (1993) reported on a few published studies dealing with the numerical modelling of hydrodynamic and solute transport processes in a prototype CT (Falconer and Liu, 1987; Falconer and Liu, 1988). Other studies had previously adopted a

mathematical (theoretical) approach to predict the outlet tracer concentration distribution for a field scale CT (Hart and Vogiatzis, 1982) and for Falconer and Liu's tank (Falconer and Tebbutt, 1986). The scope of these numerical and theoretical investigations was two-dimensional depth-integrated (2-DH) and one-dimensional (1-D) respectively.

Wang (1995) developed a 2-DH numerical model named CONTANK, which was aimed at simulating the hydrodynamic, solute transport and disinfection processes in CTs. The influence of various turbulence models and advection-diffusion schemes was evaluated, with the results being compared with data from Teixeira (1993). The discretisation of the governing equations was performed using finite differences, while the Alternating Direction Implicit (ADI) method was used in solving systems of discretised equations.

Among the findings of Wang's study was that a horizontal recirculation zone measured in the prototype tank could only be well predicted by the numerical model with the use of the k-ε turbulence model, where other options tested included the mixing length model and a large-eddy simulation (LES) model. However, it has been reported that the use of the k-ε model caused an underestimation of average cross-sectional velocities, possibly due to an overestimation of the turbulent shear stress terms (Wang and Falconer, 1998a). On the other hand, the two other turbulence models gave satisfactory predictions of the advective effects, although failing to represent turbulent mixing. In this context, Wang and Falconer (1998b) referred to the importance of using correct tools for simulating specific physical phenomena to avoid misleading conclusions,

recommending the development of sufficiently accurate models capable of predicting both the turbulent flow structure and the averaged flow properties.

In order to evaluate the effectiveness of higher-order difference schemes in representing the advective acceleration and its effect on solute transport processes, Wang (1995) tested the Quadratic Upstream Interpolation for Convective Kinematics (QUICK) algorithm and a third-order upwind scheme and compared the results with those obtained using a first-order upwind scheme. It was found overall that the advective effects were satisfactorily represented when the latter scheme was used, although the third-order scheme provided better discretisation of the advective terms. Discussions on these aspects were based on comparisons with RTD curves obtained experimentally by Teixeira (1993) for various cross-sections of the simulated CT.

Recommendations made by Wang (1995) included the development of 3-D numerical models, equipped with higher-order turbulence models, capable of performing accurately the hydrodynamic simulations, and widening the possibilities of application to more complex regions of CTs with pronounced 3-D flow.

Falconer and Ismail (1997) used a 2-DH numerical scheme similar to the model used by Falconer and Liu (1988). The Crank-Nicholson finite-difference scheme and the ADI method were deployed. The 2-DH advection-diffusion equation was discretised using the QUICK scheme in a semi-time-centred implicit version, with a substitution for the traditional central-difference scheme being based on linear interpolation. A zero-equation turbulence model, based on the assumption of bed-generated turbulence being

dominant was adopted for computational simplicity. Falconer and Ismail implemented the numerical model to simulate the prototype CT studied by Teixeira (1993). The numerical model results were in good agreement with the RTD curves for the region of 2-D flow of the CT. However, in compartments 1, 2 and 3 the results did not match the data that well, due to the inability of 2-DH models to represent vertical circulation patterns.

Three-dimensional computational fluid dynamics (CFD) techniques were reportedly applied in the modelling of field-scale CTs and reservoirs by Grayman et al. (1996), Hannoun and Boulos (1997) and Hannoun et al. (1998). A finite difference method and the standard k-ε model were used, while hydraulic efficiency assessments were essentially based on the short circuiting indicator θ_{10}. However, despite the inclusion of some empirical data in the studies, no comparisons with such data were carried out to verify the numerical model predictions, either for the hydrodynamic or the solute transport results.

Stamou (2002) deployed a commercial CFD model to investigate the effects of geometrical modifications on the hydraulic characteristics of a field-scale CT. A 3-D finite volume numerical approach, also based on the SIMPLE algorithm with the standard k-ε model was used. Although both the hydrodynamic and solute transport numerical predictions were shown, once again comparisons with empirical data were made only for the tracer curves. The level of agreement obtained between the numerical model and measured results was regarded as satisfactory in a comparison involving the respective RTD curves. This occurred in spite of the fact that the peak tracer

concentration level was underestimated in the numerical model predictions, and that the predicted mixing levels were generally underestimated by the numerical model (Stamou, 2002). After carrying out numerical model simulations with four distinct baffling setups for the tank, a comparative analysis of the numerically computed tracer results indicated the configuration with the highest hydraulic efficiency amongst the evaluated setups. Stamou's study exemplified the usefulness of modern CFD models as a design tool for the optimisation of existing CTs with complex 3-D flow patterns.

Peplinski and Ducoste (2002) made use of a statistical analysis to investigate the sensitivity of the results of a CFD model based on the SIMPLE finite volume method for uncertain input parameters. The authors investigated the influence of a number of modelling variants on the predicted results of RTD curves, including: i) type of turbulence model; ii) value of the turbulent Schmidt number; iii) wall roughness height; iv) inflow value of the turbulent kinetic energy; and v) inflow value of the turbulent length scale. It has been reported that the effluent RTD curve was mostly sensitive to the first two variants, regardless of the mixing levels in the simulated tank. On the other hand, uncertainties of the other variants assessed were found not to exert a significant impact on the predicted RTD results. The increase of σ_t reportedly induced a decrease in the short-circuiting and mixing levels in the simulations.

Teixeira et al. (2004) applied a 2-DH numerical model similar to the model of Falconer and Liu (1988) to simulate the hydrodynamic and solute transport processes of a model contact tank with 2-D flow. Very good agreement was reportedly achieved between measured RTD curves and their numerically predicted counterparts, after a sensitivity

analysis was carried out that involved the longitudinal dispersion coefficient, lateral turbulent diffusion coefficient, bed roughness and flow rate. The first two parameters were included in the 2-DH numerical model in order to compensate for the integration of the governing equations over the depth and, as well as the bed roughness, these parameters normally require calibration. The flow rate adjustment was made due to the experimental uncertainty associated with this parameter.

Further numerical modelling aspects are included in section 2.5. The following section draws on details of the physical experimentation techniques deployed in measurements of mean velocities and tracer transport in CT.

2.4. PHYSICAL EXPERIMENTATION METHODS

2.4.1 Acoustic Doppler velocimetry

Acoustic Doppler velocimetry is a relatively new technique for flow velocity measurement, with the first documented application dating back to 1994. Among its advantages in relation to Laser Doppler Anemometry (LDA) are its significant improvement in operational simplicity and versatility, at approximately a tenth of the cost (Lohrmann et al., 1994).

Generally an Acoustic Doppler Velocimeter (ADV) provides less temporal and spatial resolution than an LDA device, yet the two systems have been shown to have comparable accuracy (see Kraus et al., 1994; Lohrmann et al., 1995; Voulgaris and Trowbridge, 1998). ADV measurements of mean velocities were also verified in

18

comparisons with electromagnetic current meter results (Lane et al., 1998) and measurements of a hot film velocimeter (Finelli et al., 1999).

The ADV technique was found to be able to characterise turbulent velocity fluctuations at frequencies up to the maximum sampling rate and has reportedly measured calibrated velocities to as low as 0.4mm/s (Lohrmann et al., 1994).

Another important advantage of the ADV approach is its robustness and the fact that it does not require re-calibration, as long as the acoustic receivers are not bent or damaged. Calibration is performed by the manufacturer, who supplies the instrument with a calibration file, unique to each probe. Checks can be made on a regular basis using software provided by the manufacturer in order to confirm the good working order of the instrument (Nortek-AS, 1997a).

2.4.1.1   Principle of operation

The ADV principle of operation involves the emission of acoustic pulses via the central beam of the ADV probe at a known frequency, with these pulses propagating through the water and being reflected by suspended particulate matter. The echo is sampled by the receiver beams, so that the frequency shift caused by the movement of scatters – the Doppler shift – is measured. The flow velocity in each direction is then computed, proportionally to the frequency shift for the corresponding axis. A schematic representation of an ADV probe illustrating the emitted and reflected acoustic pulses is shown in Figure 2.1.

The location in the water where the reflected pulse is sampled is known as the sampling volume. This region in the flow corresponds roughly to a cylinder, with a diameter and height of 6mm and 9mm respectively, and lying at approximately 50mm from the probe tip (Nortek-AS, 1997a).

Figure 2.1 Representation of a down-looking 5cm ADV probe, the sampling volume and acoustic pulses (from Nortek-AS, 2004)

2.4.1.2   Operational parameters

Important parameters involved in the operation of an ADV include: the velocity range, sampling rate, signal-to-noise ratio (SNR) and the correlation coefficient (COR).

According to the manufacturer, the velocity range should be set as small as possible, while considering the maximum velocity expected in the assessed flow field and following Table 2.1. Setting an unnecessarily high velocity range usually results in excessive noise in the data (Nortek-AS, 1997a).

The sampling rate (SR) is the frequency at which data are recorded by the ADV. The instrument operates at an internal frequency of 10MHz and averages the raw acoustic

signals for a period defined as 1/SR. The standard range of sampling rate values for the Nortek-AS ADV is from 0.1Hz to 25Hz.

Table 2.1 Values of ADV velocity ranges and corresponding maximum flow velocities for the down-looking 5cm probe

ADV velocity range	Maximum horizontal velocity	Maximum vertical velocity
±3 cm/s	±30 cm/s	±10 cm/s
±10 cm/s	±60 cm/s	±15 cm/s
±30 cm/s	±120 cm/s	±30 cm/s
±100 cm/s	±300 cm/s	±75 cm/s
±250 cm/s	±360 cm/s	±90 cm/s

The SNR, given in dB, represents the strength of the received echo at each beam of the ADV probe. It is directly affected by the concentration of suspended scatters in the flow, hence a low SNR tends to be related to excessively noisy data. Therefore, the manufacturer recommends the use of seeding material when ADV assessments are carried out in clear water, in order to guarantee high SNR values. For a sampling rate of 25Hz, Nortek-AS (1997a) recommended SNR values consistently above 15dB. McLelland and Nicholas (2000) recommended a minimum of 20dB for this parameter, in an analysis based on the dimensionless spectral width of the received signal.

The seeding material used is commercially known as Sphericel-110P8, a silicate powder of neutrally buoyant hollow spheres of approximately 10µm in diameter. A seeding level between 10 and 50g/m^3 is suggested by Nortek-AS (1997a) to be maintained in water during measurements.

The correlation coefficient (COR) can be interpreted as a data quality indicator, being an outcome of the Doppler velocity calculations. A COR value of 100% indicates low-noise, reliable velocity measurements, while a COR of 0% indicates that no coherent signal was detected. Low COR generally indicates the occurrence of at least one of the following: i) that the probe is out of the water; ii) low SNR; iii) that the ADV or some component in the ADV system may be experiencing problems; and/or iv) that the assessment is being carried out in a difficult measurement regime. Martin et al. (2002) recommend a minimum COR of 70% for turbulence measurements, while COR values of around 40% provided good quality data in measurements of mean velocities.

SonTek (2004) explain that in high turbulence zones the value of COR may be affected by the short-term variability of the velocity data. It is stated that turbulence induces particles not to maintain their relative position between successive acoustic pulses, and thus, decorrelation of the signal occurs. According to Martin et al. (2002), this does not necessarily mean low quality data, but that the ADV's maximum sampling rate of 25Hz may be insufficient to resolve the turbulence in higher frequency flows.

2.4.1.3   Uncertainty and errors in ADV readings

An accuracy of ±1% is prescribed by the manufacturer for the ADV (Nortek-AS, 2004). This value includes the uncertainty involved in measurements of mean velocities, provided that the corresponding data series is averaged over a period long enough to allow the effects of noise to be cancelled out. As a general rule, the longer the time series then the less the results will be affected by noise.

Voulgaris and Trowbridge (1998) showed that the errors involved in ADV measurements can be of three types: i) sampling errors, due to electronically induced noise; ii) Doppler noise; and iii) errors due to velocity shear within the sampling volume.

A technique that allowed the determination of sampling errors of an ADV system was used by Nikora and Goring (1998) and McLelland and Nicholas (2000), who carried out measurements in still water with ADV probes that were later used in flow measurements. A similar method was used by Lyn and Rodi (1990) in order to define the lower limit of resolution of LDA measurements.

The Doppler noise and the velocity shear error are both flow-induced errors, tending to increase the variance of time velocity series, as shown by Nikora and Goring (1998). These authors explained that the Doppler noise is caused by phase uncertainty of the reflected signal, while the velocity shear error is due to mean velocity gradients occurring within the sampling volume. However, these error sources do not tend to affect the mean value calculated from a velocity time series, since their effect is averaged out due to the random nature of the errors involved (McLelland and Nicholas, 2000).

Although the ADV errors can be estimated analytically for a single sampling volume, as shown by Voulgaris and Trowbridge (1998), their direct computation becomes impracticable when a large region having several measuring locations and different flow conditions, is analysed. Therefore, in cases when second or higher order moments are to

be calculated from a measured velocity series, for instance to extract turbulence parameters, Lane et al. (1998) recommended the use of a low-pass filtering procedure that purges artificial fluctuations from the original signal. The literature reports, however, on the use of unfiltered ADV turbulence measurements (Song and Chiew, 2001). Such a filtering procedure admittedly modifies the original signal (Roy et al., 1997), but it allows a better visualisation of the lower frequency turbulent structure (Biron et al., 1995). Invariably, the choice of the filter has an effect on the computed turbulence intensity, but filtering does not tend to affect mean velocities.

2.4.2 Tracer techniques

Tracer techniques have successfully been incorporated as a tool for the hydraulic efficiency assessment of water and wastewater treatment tanks (Thirumurthi, 1969; Marske and Boyle, 1973; Thackston et al. 1987; Stamou and Adams, 1988). The acquisition of data from tracer studies can presently rely on real-time computerised monitoring, as well as automatic post-processing of results and the generation of normalised retention time distribution (RTD) curves and hydraulic efficiency indicators (HEI) (Teixeira et al., 2002).

Fluorescent dyes are probably the most common type of tracers used in CT investigations, especially rhodamine B and rhodamine WT. Fluorometers are normally used to measure and convert the fluorescence intensity of sample readings into tracer concentration. Generally, a fluorometer uses a photomultiplier to measure the amount of light emitted by the analysed sample at the emission wavelength for the fluorescent tracer used, after excitation by an internal light source (Turner Designs, 1998).

2.4.2.1 Factors affecting fluorescence readings

Deaner (1973) assessed the influence of chlorine on rhodamine B and WT for use in CTs, concluding that fluorescence readings can be quenched at relatively high chlorine residuals (> 4.0mg/l), which are not normally found in the domestic water supply system (WHO, 2004). The reason given for this decay in fluorescence is that such tracers are organic in nature and are therefore prone to being oxidised by chlorine.

Smart and Laidlaw (1977) analysed a number of fluorescent tracers and recommended that special care be taken with factors such as background fluorescence, temperature, pH, salinity and the presence of chlorine; all of which may affect the detection of fluorescence and induce misleading results to a tracer experiment. Rhodamine dyes were found to be especially sensitive to temperature variations, where the fluorescence intensity varied inversely with temperature. Where significant temperature variations occur during a tracer test, or relative to the fluorometer calibration conditions, it is recommended that the sample readings should be submitted to a correction curve for adjustment of the results.

The effect of pH on the fluorescence of rhodamine B was shown by Smart and Laidlaw (1977) to be negligible in the pH range of 5.0 – 9.0. It was also stated that salinity effects were important, only when these tracers were used in estuarine and marine environments, or in brackish groundwater.

An apparent or real background fluorescence can be detected due to natural fluorescence or suspended sediments in water. In order to eliminate the effects of the

former, the background level read at the start of an experiment should be deducted from all samples, so that only differences in fluorescence due to the injected tracer are effectively considered. For this reason, care should be taken in maintaining a constant background fluorescence throughout a tracer test.

Details of the tracer techniques deployed in this study, including the characteristics of the tracer and fluorometer used, experimentation methods and data acquisition and processing procedures are discussed in section 3.4.2.

2.5. ASPECTS OF NUMERICAL METHODS

2.5.1 Finite volume method

The finite volume method (FVM) can be regarded as a particular case of the method of weighted residuals, in which the weighting function assumes unity. It has also been referred to as "just a variant of the finite difference scheme" (Tannehill et al., 1997), not having even been mentioned by Abbott and Basco (1989) as a distinct numerical method. However, perhaps due to its most remarkable feature, i.e. being based on the macroscopic conservation laws of physics rather than on continuum mathematics concepts (Roache, 1998) it has received considerable attention in the past decade or so, making this method highly popular amongst computational fluid dynamiscists.

2.5.1.1 SIMPLER algorithm

The SIMPLE (Semi-Implicit Method for Pressure-Linked Equations) family of algorithms has a number of variants, such as the SIMPLER and SIMPLEC methods (Patankar and Spalding, 1972; Patankar, 1980; Patankar, 1981; van Doormaal and Raithby, 1984). A common feature of these methods is the way in which the flow equations are solved, i.e. by computing the velocity and pressure fields alternatively and iteratively, until convergence. An essentially similar method was developed by Issa (1985), which became known as the PISO (Pressure-Implicit with Splitting of Operators) method. These algorithms were compared by Jang et al. (1986), who concluded that the SIMPLER method tended to converge faster than its predecessor SIMPLE, and to be at least as fast as the other iterative methods evaluated. Jang et al. also reported favourably on the use of the SIMPLER method when a scalar variable is strongly coupled to the momentum equations, such as when the k-ε turbulence model is used.

The SIMPLER algorithm, as well as any other modelling approach based on the FVM, applies the conservation principle for a quantity ϕ (e. g. mass, momentum or solute concentration), for each non-overlapping control volume (CV) of a computational domain. The integrated differential equations then give discretised equations containing the value of ϕ for a number of "neighbour" grid points. Once the integral conservation of the dependent variable has been satisfied for each CV, it is then also verified over the whole computational domain for any number of grid points (Patankar, 1980). This implies that even relatively coarse grids exhibit an exact integral balance of ϕ, although the correctness of each individual computed value at an internal point still depends on the mesh fineness.

Adopting an iterative solution approach, as opposed to a direct method to solve the governing equations, has the disadvantage of potentially inducing low convergence ratios for computations with a relatively fine grid and for flows with a strong elliptic character, i.e. which have a relatively low Reynolds number (Kelkar and Patankar, 1989). Furthermore, the propagation of information from the boundaries tends to be slower for iterative methods than for direct methods. However, iterative methods have the key advantage of requiring considerably less computer storage and time. This is especially so for non-linear 3-D problems, similar to those of interest in this study.

With respect to the computational time required to achieve a converged solution using SIMPLE or SIMPLER, Braaten and Patankar (1989) inferred that this parameter "varies almost quadratically" with the number of CVs that constitute a given computational domain. This is due to the fact that the cost per iteration and the required number of iterations are each directly proportional to the number of CVs in the domain. Hence, if mesh refinement is applied to a given situation in which the number of grid points increases by a factor of 2, then the required computational time for the finer mesh simulation will be approximately 4 times that of the coarser mesh simulation, for a similar convergence level.

2.5.2 Turbulence modelling

As discussed in section 2.3.2, a previous numerical investigation of the hydrodynamic and solute transport processes in a CT concluded in favour of the use of the standard k-ε model to model the turbulence, rather than either a zero-equation model or a large eddy simulation (LES) model (Wang, 1995). Nonetheless, Revstedt et al. (1998) reported on

a successful application of LES modelling to simulate a baffled stirred reactor, used in a chemical engineering plant, while Balaras and Benocci (1994) used the technique to predict complex wall bounded flows. Numerous other successful applications of LES models to fluid flow problems can be found in the literature. However, Rodi et al. (1997) inferred that "a great deal of research is required before it will be known how widely the (LES) method can be used". For such reasons, in this review attention has been focused on aspects relating to the k-ε model, as discussed below.

The k-ε model is probably the most successfully applied and validated turbulence model for a wide range of hydraulic flow conditions, since the development of the standard version (Launder and Spalding, 1972; Launder and Spalding, 1974). One of the key strengths of the standard k-ε model reportedly lies in the use of an empirical wall function approach to establish the boundary condition for the hydrodynamic equations (Versteeg and Malalasekera, 1995). By using such an approach the need for several extra grid points is avoided, as would otherwise be required to obtain an adequate resolution of the viscous sub-layer, thus resulting in a considerable economy of computer resources in numerical simulations (Rodi, 1993).

However, due to the assumption of isotropic eddy viscosity the standard k-ε model is not able to represent stress-driven secondary motions, e.g. in square ducts (Wilcox, 1998). Non-linear versions of the k-ε model have thus been developed, such as the version due to Speziale (1987), which have proven to be able to account for such phenomena (Rokni et al., 1998).

Furthermore, the standard k-ε has been developed to simulate fully turbulent flows, i.e. where the viscous effects are deemed to be unimportant. In order to address flows with relatively low or intermediate levels of turbulence, as well as near wall flows, further variants of the k-ε model have been developed, in which damping functions have been incorporated into the original version of the model in order to mimic the direct effect of molecular viscosity on the shear stress (Patel et al., 1985). These versions have become known as low Reynolds number k-ε models.

The flow in contact tanks, and specifically in model and prototype units, often includes regions with relatively low velocities, as well as stagnant, recirculating flow regions (Teixeira, 1993). These flow fields can result in the occurrence of flow separation points and low turbulence regions, where the standard k-ε model normally fails (Rodi, 1993). It would therefore be appropriate to evaluate the applicability of low Reynolds number k-ε models in numerically simulating the hydrodynamic processes in CTs, as well as its effect on the corresponding numerical predictions of the solute transport processes. No published studies have been found in the literature where such an approach was used and validated with hydrodynamic and solute transport data.

2.5.3 Initial and boundary conditions

As pointed out by Roache (1998), a precise specification of the initial conditions for an incompressible flow problem is not of crucial importance, since during the numerical solution process the error of the initial guess is generally many orders of magnitude larger than the convergence or accuracy criteria. Thus, more often than not the initial

distributions of velocity, pressure and turbulence parameters are set to zero in the interior of the solution domain. Such an initial condition was recommended by Patankar (1980) for use with the SIMPLER algorithm.

The types of boundary conditions (BCs) generally applicable for 3-D numerical simulations of CTs can be classified as being: i) free surface; ii) inlet; iii) outlet; and iv) solid boundary. Aspects related to the choice and implementation of the free surface and outlet BC deserve special attention and have been approached in this review, as discussed below.

With regard to the surface BC, the rigid-lid treatment is recommended for situations with negligible variation of the water depth and for sub-critical flows (Sengupta, 1977; Lai et al., 2003). When using this type of surface BC the water depth is a constant parameter of the numerical simulations. Lai et al. (2003) reported of satisfactory results being obtained using this BC in simulations for an S-shaped open channel, in spite of a measured variation in the free surface elevation of up to 4% of the flow depth. Furthermore, under the condition of zero wind shear the free surface can also be represented as a free-slip boundary, by setting the normal gradients of appropriate variables to zero. The rigid-lid, free-slip treatment was successfully applied by Stamou (2002) as the surface BC for 3-D numerical simulations of a field-scale CT.

At an outlet section the zero-gradient or Neumann BC is generally used for the hydrodynamic and solute concentration variables. As pointed out by Adams and Rodi (1990), the use of this type of BC for outlet sections of treatment units has the

physically realistic effect that "disturbances at the outlet cannot propagate upstream into the tank". However, Demuren and Rodi (1983) explained that care should be taken regarding the location of the outflow boundary in situations with recirculating flows, for the appropriateness of this type of BC. The authors recommended that in such conditions the outflow boundary should be located no less than two reattachment lengths downstream of the reattachment point of the recirculation zone.

2.5.4 Line-by-line solution technique

The line-by-line technique has been extensively used to solve fluid flow problems and is similar in conception to the Alternating Direction Implicit (ADI) method (Roache, 1998). The method of application of the line-by-line method for 3-D flow problems has been explained by Versteeg and Malalasekera (1995).

One of the key advantages of the line-by-line and ADI methods is that a solution algorithm for tridiagonal systems of linear algebraic equations, namely the Tri-Diagonal Matrix Algorithm (TDMA), is relatively simple to implement and requires substantially less computational resources than any method which deals with 5 or 7 diagonal matrixes. Another advantage lies in the larger time steps that can be handled in solving parabolic problems in comparison with explicit schemes, providing a fast and efficient solution procedure (Tannehill et al., 1997).

Summary

In this Chapter a review has been undertaken of the main aspects relating to the physical experimentation and numerical modelling of flow and solute transport in Contact Tanks (CTs). Significant recent advancements were identified as being mainly: i) for the physical experimentation side, such as a study involving the direct assessment of the turbulent flow field by laser Doppler anemometry (LDA) in a prototype CT and with a complex 3-D flow; and ii) for the numerical modelling side, with the introduction of 3-D numerical schemes in CT simulations and provision as a tool for optimisation studies. However, the verification of the hydrodynamic numerical predictions has not been reported for situations of complex 3-D flows.

Details have been given regarding the use of a relatively new technique for flow velocity measurement, i.e. Acoustic Doppler Velocimetry (ADV), which has gained in popularity in recent years due to its advantages in relation to LDA. Aspects related to the use of fluorescent tracer techniques have also been considered herein.

Further numerical modelling aspects in this Chapter involved the use of the SIMPLER finite volume method; turbulence modelling; prescription of initial and boundary conditions; and details of a relatively fast and efficient line-by-line solution technique. With regard to the modelling of turbulence, a need for further research has been identified regarding the application and validation of low Reynolds number k-ε models to simulate the hydrodynamics of CTs, since this technique can potentially address the flow characteristics that reportedly occur in prototype scale, as well as field scale, contact tanks. Such an approach has not yet been reported in the literature.

Chapter 3

Experimentation Methods

3.1. INTRODUCTION

This chapter describes the materials and methods deployed during the physical experimentation of this research project. The hydraulic circuit is outlined in section 3.2, followed by a characterisation of the prototype tank, in section 3.3. The data acquisition and processing systems involved in the velocity measurements and tracer experiments are outlined in section 3.4.

3.2. HYDRAULIC CIRCUIT

The hydraulic circuit components were the main experimentation unit, henceforth referred to as the prototype tank (PT), two water supply tanks (WST1 and WST2), two centrifugal pumps (CP1 and CP2), an electromagnetic flow meter (FM) and four flow control valves (FCV1, FCV2, FCV3 and FCV4) and associated piping and connections. A diagram of the hydraulic circuit is given in Figure 3.1.
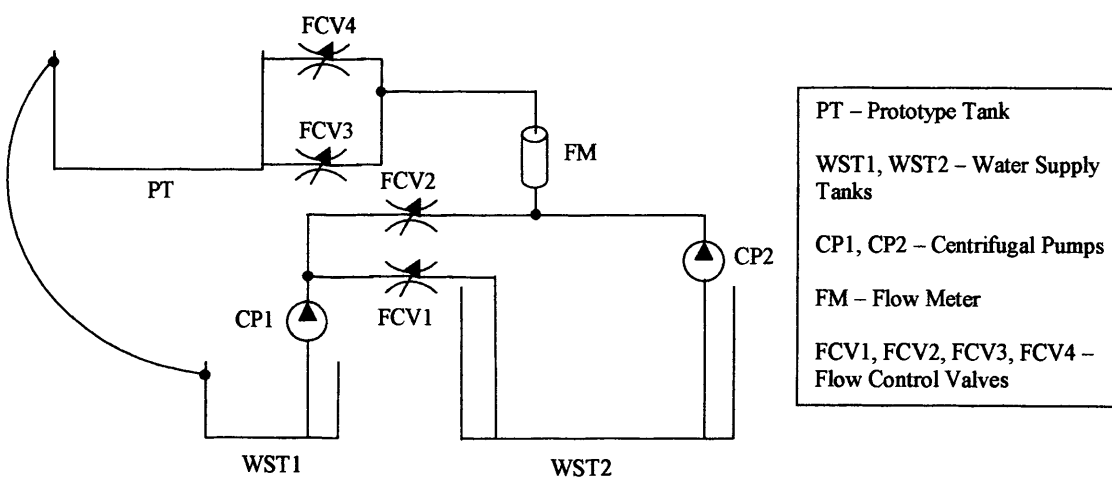
Figure 3.1 Graphical diagram of the hydraulic circuit, illustrating the Prototype Tank and associated auxiliary devices and components

Both pumps CP1 and CP2 were 0.5 hp devices, manufactured by Clarke International, model CPE15S. The flow meter was produced by Euromag, model MUT1100, with an internal diameter of 40 mm and calibrated by the manufacturer. An MC106 converter was connected to the flow meter in order to display readings. The pipeline and connections were made of plastic and had an internal diameter of 40 mm. A flexible plastic pipeline system of 140 mm in diameter, was used as a gravity return line for water from PT to WST1.

The water supply tank WST1 had a capacity of 4.7 m^3 and was built of steel. This tank provided a dedicated supply to the operation of PT under a closed circuit mode, being the sole supply tank used for the velocity data acquisition experiments. Due to its relatively low capacity, WST1 provided a quick return of the water into PT during the velocity measurements, which helped to minimise losses of material due to the settling of the seeding particles (see section 3.4.1).

The other reservoir, WST2, had a capacity of approximately 64 m^3 and it was the main supply tank in the Hydraulics Laboratory. The connection of this tank to the hydraulic circuit of PT was made in order to provide enough retention time for the recirculated dyed water not to interfere with the results of an ongoing tracer test in the PT. Thus, for tracer tests, FCV1 was kept partially open to give the desired discharge, while FCV2 remained closed and both pumps CP1 and CP2 were activated. For experiments where only velocities were measured, then the control valves FCV1 and FCV2 were inverted, CP2 was turned off and WST1 acted as the sole supply reservoir for the system.

3.3. PROTOTYPE TANK

The prototype tank (PT) that provided experimental data of velocity fields and tracer transport for this study was built in the Hyder Hydraulics Laboratory of the School of Engineering at Cardiff University. This unit had similar dimensions to a scaled chlorine contact tank (CCT) located at Embsay Water Treatment Works, England, designed and operated by Yorkshire Water. A photographic illustration of PT is shown in Figure 3.2. At its original design configuration, the serpentine tank was formed by 8 compartments, as indicated in the Figure. The tank's lateral walls are referred to as walls W1, W2, W3 and W4.

Figure 3.2 Photograph of the Prototype Tank, illustrating the setup with 8 compartments and indication of the direction of the main flow in compartments by arrows

Two geometrically similar models of the Embsay CCT have been previously investigated (Teixeira, 1993). The design of the unit for this study, however, aimed at providing a more flexible and useful laboratory model to be used in investigations of the

hydrodynamics and solute transport processes of water treatment tanks, and also providing data for verifying 3-D CFD (Computational Fluid Dynamics) models. The main structure of the PT was fabricated in steel and had part of the lateral walls W1 and W3 made of glass for flow visualisation purposes (see Figure 3.3). It had two types of inlet devices, namely an open channel and a pipe device, which corresponded to the most commonly found inlets in field-scale CCTs. Its baffles could be arranged with relative ease, so as to allow investigations of a range of flow patterns as well as optimisation studies for different geometrical configurations. The bed of the PT was covered with a 12mm layer of plywood, in order to allow structures such as baffles to be attached to the bottom of the unit and re-located as appropriate. Figure 3.3 shows a plan view of the original setup (OS) of PT.
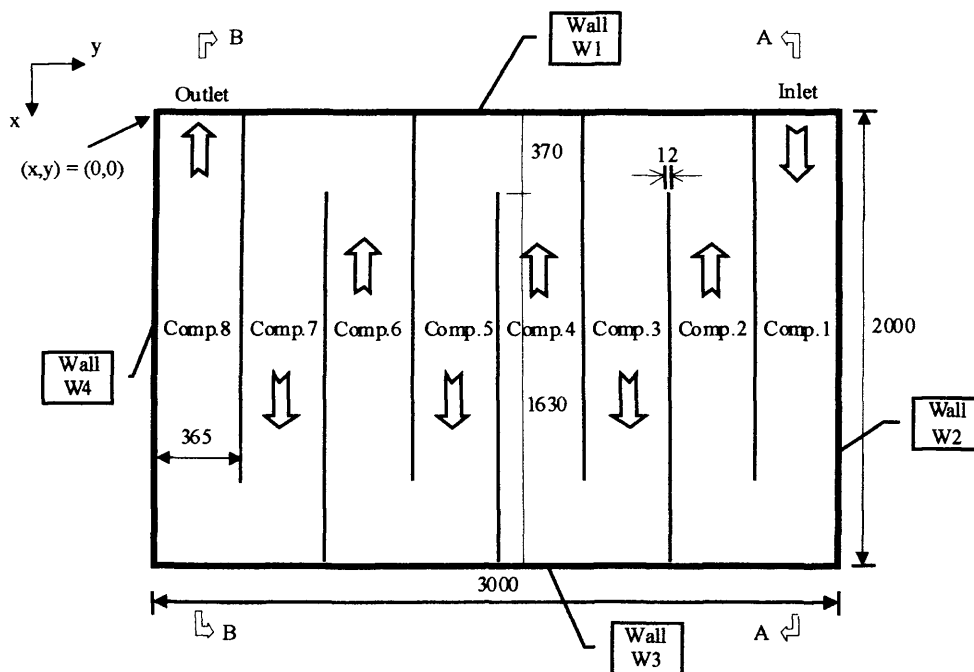
Figure 3.3 Plan view of the original setup of the Prototype Tank, illustrating 8 compartments, the lateral walls, as well as the coordinate system used and arrows indicating the direction of the main flow (dimensions in mm)

3.3.1 Inlet devices

Section A-A, as indicated in Figure 3.3, is illustrated in Figure 3.4. This cross-section view includes a representation of the inlet devices, consisting of an open channel at the top-right corner and a pipe at the bottom-right corner of the diagram. These were situated at wall W1, in the region corresponding to Compartment 1 of the unit's original setup.

The pipe inlet was installed next to the bed of the PT and its centre was vertically aligned with the centre of the channel inlet, being at Y=2820mm. These two inlet devices could be used alternately by switching the control valves FCV3 and FCV4 in the appropriate manner. Figure 3.5a shows a front view of the inlet devices at wall W1, in Compartment 1 of setup OS.
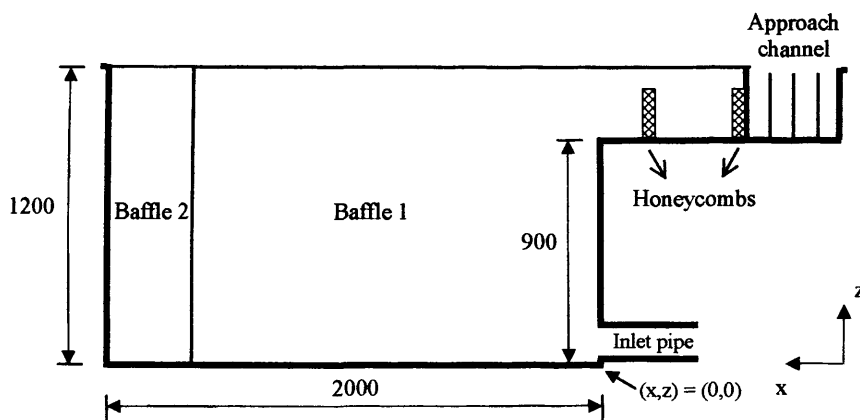
Figure 3.4 Section A-A of the Prototype Tank, as indicated in Figure 3.3, illustrating the location of the inlet devices (dimensions in mm)

Connected to the channel inlet was an approach channel which bared some resemblance to the configuration used by Teixeira (1993) for the Embsay CCT. Three guiding vanes

located in the 90° bend and two honeycomb devices acted as flow-homogeniser structures for the inflow, which are represented in more detail in Figure 3.6.

The pipe inlet device had an internal diameter of approximately 152 mm (6") and was made of plastic. This device was adapted with a tracer injection device that involved a control valve with a connector for a syringe, a diffuser and three injection needles, which were placed around the pipe, as shown in Figure 3.5b.
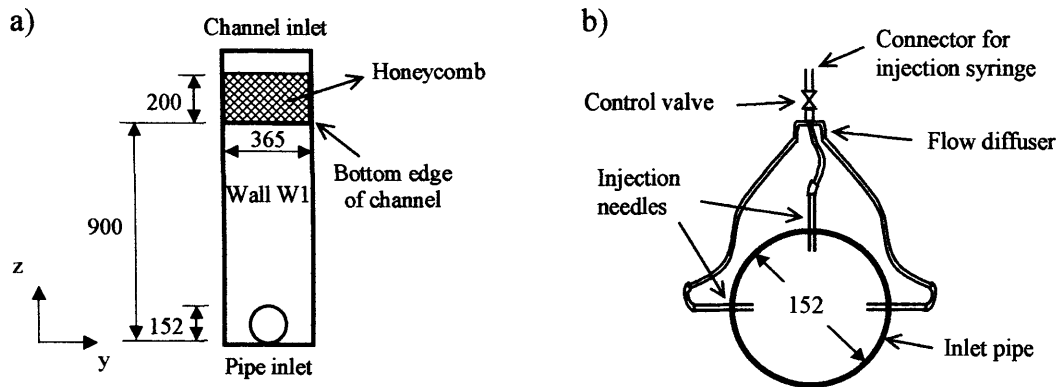
Figure 3.5 Front view of inlet sections of the Prototype Tank, illustrating: a) the channel and pipe inlet devices at wall W1; and b) the tracer injection device connected to the inlet pipe (dimensions in mm)
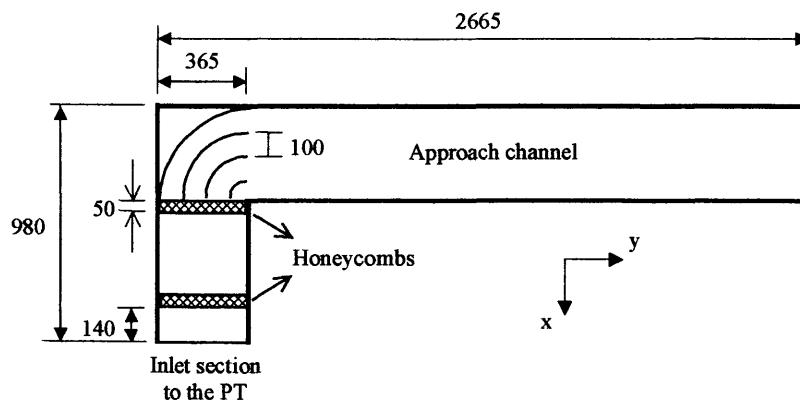
Figure 3.6 Superior view of the approach channel to the Prototype Tank, indicating the location of the honeycombs and guiding vanes (dimensions in mm)

3.3.2 Outlet section

The outlet section of the PT consisted of a sharp-crested rectangular weir made of plywood, which was located at wall W1 (as indicated in Figure 3.3). The weir crest was 12mm thick and was at an elevation of 980 mm above the tank bed. The width of the outlet section corresponded to the width of Compartment 8 of the original setup of PT.

After exiting the tank, the water discharged over the weir was collected in a rectangular steel box and returned to WST1 by gravity. Figure 3.7 illustrates a lateral view of Section B-B of the PT, as indicated in Figure 3.3, where the location of the outlet weir is indicated at the top-left corner.
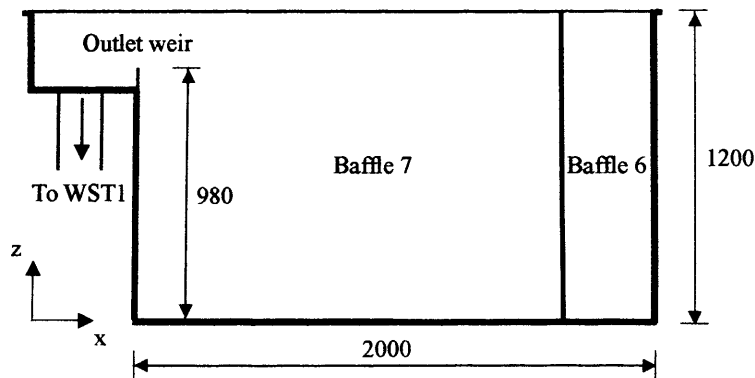
Figure 3.7 Section B-B of the Prototype Tank, as indicated in Figure 3.3, illustrating the outlet weir at the end of Compartment 8 (dimensions in mm)

3.3.3 Baffling arrangements

The 7 baffles used to construct the original setup (OS) of PT were 12mm thick, 1200mm high and 1660mm long plywood sheets. These baffles were mounted on the

plywood bed of the tank and were longitudinally oriented in relation to the inflow, in such a location as to give 8 compartments of similar width, as shown in Figure 3.3.

In addition to setup OS, four other baffling arrangements have been experimentally assessed in this study. Modified setups of the tank were obtained by removing and/or repositioning baffles in the interior of PT, in order to reproduce flow patterns with varying levels of short-circuiting and mixing.

Setup MS1 was obtained by removing baffles 6 and 7 (i.e. the baffles that separate compartments 6 and 7 and compartments 7 and 8 respectively) from the baffling arrangement of setup OS. A schematic representation of setup MS1 is shown in Figure 3.8a. Further removal of baffles 4 and 5 gave rise to setup MS2, as shown in Figure 3.8b. Figure 3.8c illustrates setup MS3, which corresponded to an unbaffled configuration of PT. A cross-baffling arrangement (Teixeira, 1995) was reproduced in setup MS4, where 5 compartments were transversally oriented in relation to the main inflow direction. A schematic representation of setup MS4 is shown in Figure 3.8d.
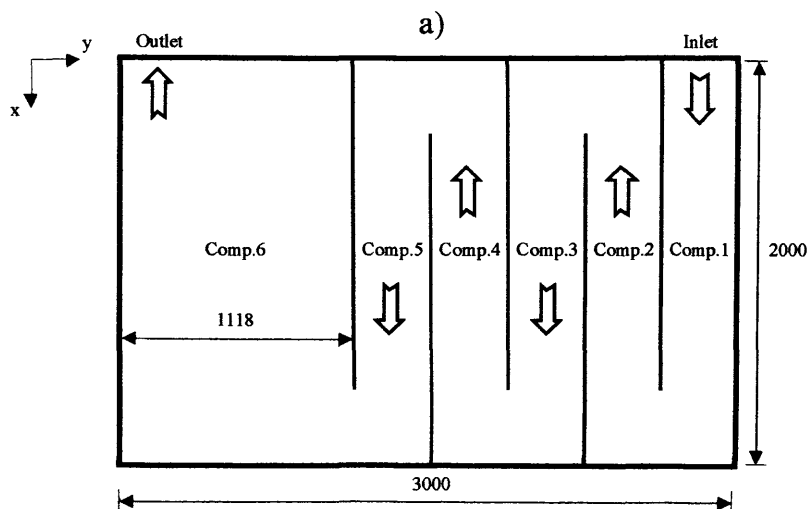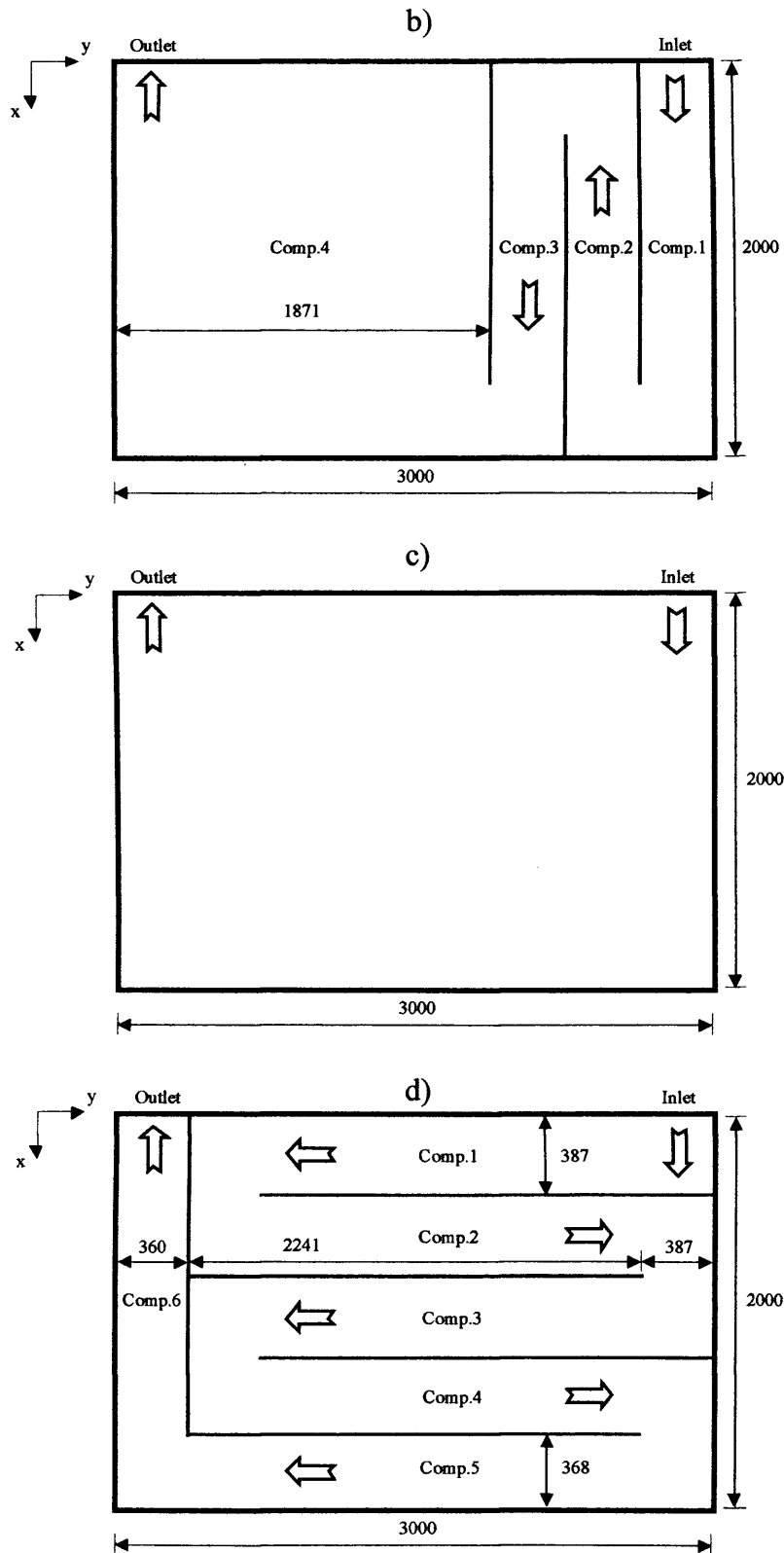
Figure 3.8 Plan view of the modified setups of the Prototype Tank, illustrating: a) setup MS1; b) setup MS2; c) setup MS3; and d) setup MS4. The arrows indicate the direction of the main flow in each design setup (dimensions in mm)

43

3.4. DATA ACQUISITION AND PROCESSING SYSTEMS

Data sets obtained in this research were twofold: mean velocity fields were measured using an Acoustic Doppler Velocimeter (ADV) and solute concentration curves were obtained with a digital fluorometer. Details of the data acquisition and processing systems and materials are given in this section.

3.4.1 Mean velocity measurements by ADV

3.4.1.1 Characteristics of the data acquisition system

The flow velocity measurements of this study were conducted using a down-looking ADV probe manufactured by Nortek-AS. The probe's serial number was N0093 and it has been used in a number of research projects carried out in the University's Hydroenvironmental Research Centre. During the velocity measurements, the ADV probe was controlled by a computer, using the data acquisition software supplied by the manufacturer (Nortek-AS, 1997b). As a result, data files were recorded that contained the velocity time series measured by the ADV.

A software check of the ADV probe used was performed on a routine basis, in order to test the ADV system for errors. During these tests, which were carried out according to recommendations of the manufacturer (Nortek-AS, 1997a), the instrument was found to be in good working order.

The ADV operation required the definition of a number of parameters associated to the velocity data acquisition, as part of the ADV software configuration. The water temperature and salinity were set to 20°C and 0ppt respectively. Under such conditions, the speed of sound in water was calculated by the ADV software as being 1482m/s. The velocity range parameter was set to 10cm/s, while the sampling rate adopted was 25Hz, which corresponded to the instrument's maximum sampling rate. The length of the time velocity series acquired in each sampling point was 3min, which respectively resulted in 4,500 instantaneous velocity values being recorded.

In order to improve data quality, the value of the signal-to-noise ratio (SNR) of the ADV measurements had to be maintained above 15dB (see section 2.4.1). This required the frequent addition of further seeding material to the system, and a low water level was kept in the water supply tank WST1 (see Figure 3.1) to reduce the residence time of the water in WST1 and, thus, minimise the settling losses. The SNR values were monitored on the ADV software screen during measurements.

The coordinate system orientation for the velocity measurements followed that defined for the PT (see Figures 3.3 and 3.4). The ADV probe was attached to a movable rack, which allowed manual displacement in all directions over the PT. The displacement of the ADV probe was guided by millimetre scales affixed to the supporting rack.

3.4.1.2 Data processing

The conventional data output from the ADV velocity measurements was a binary file with an extension *.adv, created by the data acquisition software (Nortek-AS, 1997b).

Data columns in one such file included the time, velocities, correlation parameter (COR) and SNR value for each sample.

The *.adv files were processed by the software WinADV, version 2.009 (Wahl, 2000). An illustration of the software's main screen is shown in Figure 3.9. Samples with low COR and/or low SNR were removed from the velocity series, where the restrictions applied were average SNR ≥ 15 dB and average COR > 70%. Using the processing options of the software, the data series were also submitted to a spike detection algorithm developed by Goring and Nikora (2002). After submitted to the filtering process the data were used to calculate the mean velocity fields, which were then plotted using the Tecplot software.
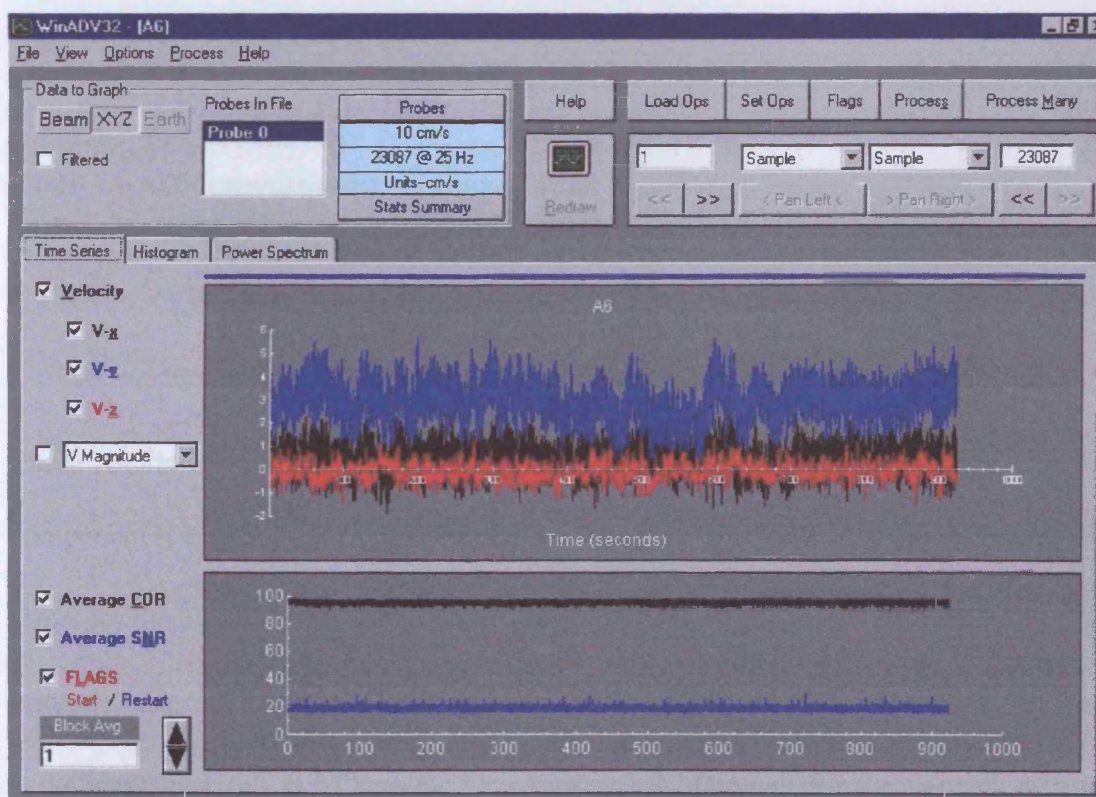
Figure 3.9 WinADV software main screen

3.4.1.3 Uncertainty and error estimation

An accuracy of ±1% was prescribed by Nortek-AS (2004) for the ADV, which was regarded in this study as the uncertainty range (σ_{ADV}) for the mean velocity measurements. An estimation of the ADV sampling errors was made by carrying out a still water test, following McLelland and Nicholas (2000). For this test, the ADV probe was placed in a large container with 70 litres of seeded water and the system was left undisturbed for approximately 30min. Data acquisition was then carried out for 2min, at the sampling rate of 25Hz. During this test the SNR values were in the range of 15 to 18dB, while the values of the correlation parameter were higher than 95%. The measured data series was used to estimate the errors for the mean velocity components ($|\sigma_U|$, $|\sigma_V|$ and $|\sigma_W|$) and for the respective standard deviation values ($|\sigma_u|$, $|\sigma_v|$ and $|\sigma_w|$). The results obtained are shown in Table 3.1.

Table 3.1 ADV sampling errors estimated from the still water test

$|\sigma_U|$ (cm/s)	$|\sigma_V|$ (cm/s)	$|\sigma_W|$ (cm/s)	$|\sigma_u|$ (cm/s)	$|\sigma_v|$ (cm/s)	$|\sigma_w|$ (cm/s)
0.01	0.01	0.07	0.46	0.47	0.08

These results showed that the sampling error associated to the mean vertical velocity component (i.e. $|\sigma_W|$ = 0.07cm/s) was higher, by almost an order of magnitude, than the errors for the mean horizontal velocity components (i.e. $|\sigma_U|$ = $|\sigma_V|$ = 0.01cm/s), but the opposite occurred for the respective standard deviation results (i.e. $|\sigma_u|$ = 0.46cm/s, $|\sigma_v|$ = 0.47cm/s and $|\sigma_w|$ = 0.08cm/s). The error values obtained for the vertical velocity

component (i.e. $|\sigma_W|$ and $|\sigma_w|$) were of the same order of magnitude. On the other hand, for the horizontal velocity components the error values for the corresponding mean results (i.e. $|\sigma_U|$ and $|\sigma_V|$) were considerably lower than the respective standard deviation results (i.e. $|\sigma_u|$ and $|\sigma_v|$). This indicated that a discrepancy occurred between the sampling errors for the horizontal (x and y) and vertical (z) directions. This fact has been regarded as a consequence of the geometrical characteristics of the down-looking ADV probe (Voulgaris and Trowbridge, 1998).

The significance of the sampling errors determined for the mean velocity components was evaluated in relation to the prescribed uncertainty of the ADV measurements. An analysis was carried out for two flow conditions, i.e. fast and slow flows, which represented the range of flow velocities expected to occur in the PT. The results obtained are shown in Table 3.2.

Table 3.2 Significance of the estimated ADV sampling errors for the mean velocities relatively to the prescribed uncertainty range of the instrument ($\sigma_{ADV} = \pm 1\%$)

Flow condition	Fast: mean velocity $\approx 10cm/s$ $\sigma_{ADV} \approx 0.1cm/s$	Slow: mean velocity $\approx 1cm/s$ $\sigma_{ADV} \approx 0.01cm/s$
Sampling errors	$|\sigma_{U,V,W} / \sigma_{ADV}|$	
$|\sigma_U| = 0.01cm/s$	0.1	1.0
$|\sigma_V| = 0.01cm/s$	0.1	1.0
$|\sigma_W| = 0.07cm/s$	0.7	7.0

Table 3.2 shows that the order of the sampling errors associated to U and V for the fast and slow flow conditions was inferior (i.e. $|\sigma_{U,V,W} / \sigma_{ADV}| \ll 1.0$) and similar (i.e.

$\left|\sigma_{U,V,W} / \sigma_{ADV}\right| \approx 1.0$) to the ADV uncertainty respectively. On the other hand, for W the order of the sampling errors for the fast and slow flow conditions was similar and superior (i.e. $\left|\sigma_{U,V,W} / \sigma_{ADV}\right| >> 1.0$) to the magnitude of the ADV uncertainty respectively.

In short, the analysis carried out based on Table 3.2 indicated that, for the horizontal velocity components and/or under the fast flow condition considered, the accuracy of the ADV measurements was within the range of ±1% prescribed by the manufacturer. On the other hand, under the slow flow condition the sampling error associated to the determination of the mean vertical velocity component was potentially the key factor that impaired the accuracy of the corresponding ADV measurement. A sampling error of 0.07cm/s was associated to the estimation of W, which would represented almost 10% of the corresponding mean velocity measured under the slow flow condition.

3.4.2 Tracer experiments

Tracer experiments were performed in this study with the main aim of providing information on the solute transport characteristics of the flow in the experimentation tank. The fluorescent tracer rhodamine B and a digital fluorometer Turner AU-10 (Turner Designs, 1998) were used in the tracer tests. Rhodamine B, otherwise known as Tetraethylrhodamine, is a relatively common fluorescent dye used for water tracing (see section 2.4.2), its main advantages being the relatively low cost compared to other dye tracers and a very high detectability (Smart and Laidlaw, 1977).

The tracer tests carried out in this study were of the "black box" type, consisting of an injection of the tracer solution at the inlet section, followed by sampling at the outlet to monitor the outflow tracer concentrations with time.

The water used in the tracer experiments was virtually free of suspended material and chlorine residual, since it was taken from the mains distribution system and kept in the supply tank WST2 (see Figure 3.1) for relatively long retention times. The water used in the tracer experiments was not mixed with the seeded water used in the velocity measurements, in order to mitigate potential tracer losses due to absorption (see section 2.4.2 and Smart and Laidlaw, 1977).

3.4.2.1 *Preparation of tracer solutions*

The dye rhodamine B was available as a powder. A precision scale was used to weigh a specified mass of this tracer, which was then diluted into distilled water to give a solution with the desired concentration. This procedure was carried out using the equipment and facilities of the Soil Mechanics Laboratory, observing conventional laboratory and safety practices. The tracer solution was then stored in an amber glass bottle and kept at room temperature in the Hydraulics Laboratory. Each base solution prepared had a volume of 500ml, where the tracer concentration was 5.0g/l.

Other solutions were prepared to be used in the calibration of the fluorometer. The tracer concentration of these samples was of the order of $10^{-2} - 10^{-1}$mg/l, or between 10 and 100ppb. Due to these relatively low concentration values, a dilution procedure was used in the preparation of these samples, which is shown in Figure 3.10.
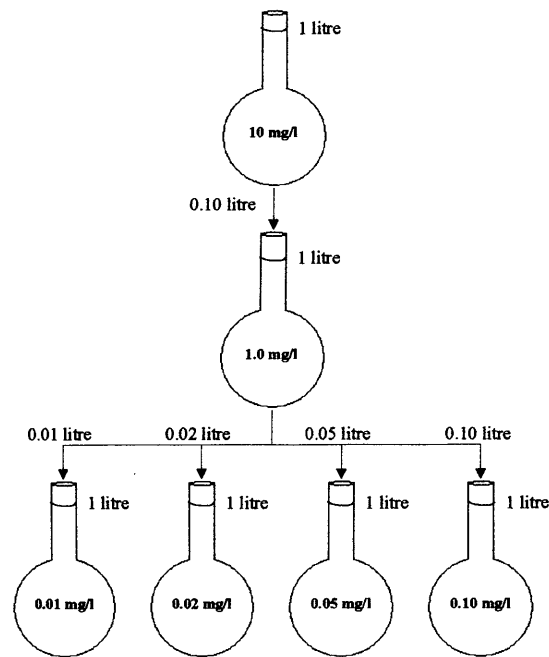
Figure 3.10 Dilution scheme for tracer solutions used in the fluorometer calibration

3.4.2.2 Calibration of the fluorometer

The calibration procedure recommended by the manufacturer was used to calibrate the fluorometer (Turner Designs, 1998). It involved setting the zero and standard levels of concentration with the instrument under calibration mode, and by using solutions containing respectively 0ppb (pure distilled water) and100ppb of Rhodamine B.

Solutions with concentrations of 0, 10, 20, 50 and 100ppb were then analysed and a calibration curve was plotted, as shown in Figure 3.11. The equation obtained was based on a linear regression curve that best fitted the data. Re-calibration was frequently performed, in order to obtain an updated correction equation for the fluorescence readings. This was usually undertaken before every new round of experimentation.
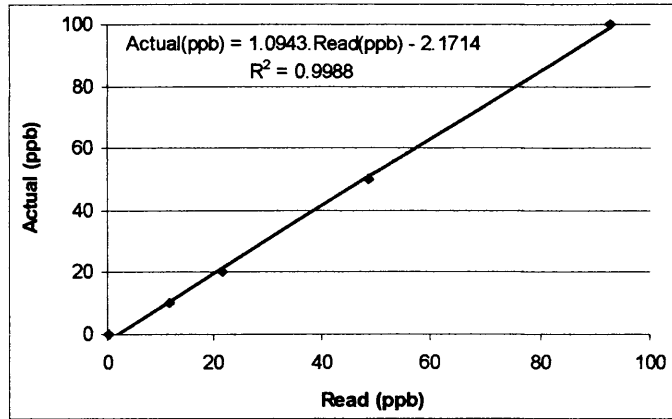
Actual (ppb)	Read (ppb)
0.00	0.20
10.00	11.50
20.00	21.50
50.00	48.73
100.00	92.48

Figure 3.11 Calibration curve used to correct tracer concentration readings

3.4.2.3 Injection of the tracer

From the base solution with a concentration of 5.0g/l, 50ml were taken with a syringe for the use in each tracer test. This provided a mass of tracer (M) of 250mg per experiment. When divided by the wet volume (V_w) of PT, of 6,000 litres, then this gave a mean concentration in the tank $(C_0 = M/V_w)$ of approximately 0.042mg/l, or 42ppb. This parameter was important for the estimation of the level of concentration expected to occur in the experiments, besides later being used in the non-dimensionalisation of the tracer data.

Before the start of each test, the hydraulic system was operated at the experimentation flow rate for about 2 hours, in order to allow the flow in PT to achieve a steady state. Such a period of time was longer than four times the unit's hydraulic retention time $(HRT = V_w/Q)$, which corresponded to $HRT = 27$min. During this period, the fluorometer readings were checked for variations in the background fluorescence and experiments were only commenced once the background level exhibited a constant behaviour.

52

The inlet tracer injection was made manually and as uniformly as possible, without provoking significant disturbances to the inflow. Thirumurthi (1969) and Marske and Boyle (1973) considered that an instantaneous tracer injection was achieved when it was performed in less than $1/50^{th}$ of HRT. In this study such a period of time would correspond to nearly 30s. However, the injection of the tracer solution was normally performed in 10s in this study, which corresponded to approximately $1/150^{th}$ of HRT.

3.4.2.4 Monitoring of concentrations

Water samples were continuously pumped from the outflow from a location above the centre of the outlet weir. The sampled water was directed through the fluorometer to be analysed, before being discarded. The time of travel between the outlet section and the fluorometer was measured and confirmed to be 5s. This time phase was later discounted from the actual sample reading times. The results from three valid tracer test replicas were used to calculate the mean tracer passage curve for each design setup of the PT.

3.4.2.5 Data processing

The output from each tracer test was reproduced in the form of a log file created by the fluorometer in ASCII format. This file contained the data of the measured concentrations with time, which were later processed using a Fortran routine. The data processing firstly involved discounting the travel time of the samples and the value of the background concentration from the corresponding recorded values. After taking account of these aspects, the data were then non-dimensionalised and normalised by using conventional tracer data processing methods (Levenspiel, 1999).

For each test the tracer mass recovery index (REC) was calculated and the experiment was considered valid for $0.95 < \text{REC} < 1.15$ (Stamou and Adams, 1988). Values of REC situated outside this range may indicate occurrence of high tracer loss (e.g. due to absorption or reaction with other compounds) during the test and/or may be caused by improper calibration or malfunction of the fluorometer.

The final outcomes of the tracer tests were the retention time distribution (RTD) and accumulated tracer mass (F) curves, as well as the hydraulic efficiency indicators (HEI) associated to each configuration of the PT. The RTD curves were plotted as $E(\theta)$ as a function of θ, where $E(\theta)$ was the normalised tracer concentration and θ was the normalised time. The HEI parameters were indicators of the level of short circuiting or mixing in the flow system. From the wide range of parameters available in the literature for this purpose four indicators (two of each type) were selected for use in this study, which have been defined as in Table 3.4. As discussed in section 2.2.2, these indicators were shown by Teixeira and Siqueira (2005) to better represent the phenomena to which they were related, i.e. short circuiting or mixing.

Table 3.4 Definition of the short circuit and mixing indicators used to analyse tracer experiments results

Index*	Definition
θ_i	normalised time for the initial detection of tracer at the monitoring section
θ_{10}	normalised time for the passage of 10% of the injected tracer mass
Mo	ratio between θ_{90} and θ_{10} (where θ_{90} is defined similarly to θ_{10})
σ^2	ratio between the variance of the RTD curve and the normalised time for its centre of mass

* θ_i and θ_{10} for evaluating the short circuiting levels; and Mo and σ^2 for the mixing levels

Qualitative and semi-quantitative analyses of the flow patterns were carried out in Chapter 6 relatively to the idealised flow patterns of flow reactors, namely, the complete mixing (CM) and plug flow with dispersion (PFwD). The RTD curves of these flow patterns were obtained using Equations (3.1) and (3.2) respectively, given as (Levenspiel, 1999): –

$$E(\theta) = e^{-\theta} \tag{3.1}$$

$$E(\theta) = \frac{1}{4\sqrt{\pi d}} \frac{1 + \frac{1}{\theta}}{\sqrt{\theta}} e^{\left[-\left(\frac{1-\theta}{\sqrt{4d\theta}} \right)^2 \right]} \tag{3.2}$$

where $\pi = 3.1416$ and d is the dispersion number, given by: –

$$d = \frac{D_L}{U_0 L} \tag{3.3}$$

where D_L is the longitudinal dispersion coefficient, U_0 is the average (bulk) flow velocity and L is the length of flow. The value of the dispersion coefficient was estimated using the formulation of Elder (1959), given as $D_L = 5.93 H U_f$, where H is the depth of flow and U_f is the friction velocity, calculated with Equation (4.8). Specification of values for H, U_0 and L was based on the flow characteristics of setup OS, so that H = 1.01m, U_0 = 0.01m/s and L = 16.12m. As a result of this calculation procedure, the value obtained for the dispersion coefficient was $D_L = 0.0023 m^2/s$, while the dispersion number was determined as d = 0.014 for the PFwD flow pattern.

Summary

The materials and methods involved in the laboratory experiments carried out in this study were discussed in this Chapter. The hydraulic circuit was explained in section 3.2, while the main features of the Prototype Tank were outlined in section 6.3. Schematic illustrations were shown of the assessed design setups of the experimentation unit, namely, the original setup (OS) and four modified setups (MS1, MS2, MS3, MS4). The inlet devices used were of the pipe and open channel types, while a sharp-crested rectangular weir was used as the outlet device of the tank. In section 6.4 the data acquisition and processing systems were explained. Aspects of the ADV operation were described, followed by the determination of uncertainty and sampling errors involved in mean velocity measurements. The tracer techniques used were outlined and the outcomes of the tracer tests of interest to this study were identified as being the retention time distribution (RTD) curves and the associated hydraulic efficiency indicators (HEI). Two short-circuiting indicators, i.e. θ_i and θ_{10}, and two mixing indicators, i.e. Mo and σ^2 were used in this study. The procedure used to obtain the RTD curves of the complete mixing and the plug flow with dispersion flow patterns was explained. The physical experimentation results obtained are discussed in Chapter 6.

Chapter 4

Governing Equations

4.1. INTRODUCTION

This chapter presents the mathematical framework for the modelling of flow and solute transport processes of the numerical model described in Chapter 5.

The 3-D Navier-Stokes equations are presented, expressed in Eulerian, rectangular coordinates. Assumptions applicable to the flow conditions of typical contact tanks are discussed. Turbulence modelling is then approached and the equations of the k-ε model used are presented, followed by the advection-diffusion equation for modelling the transport of conservative solutes. Cartesian-tensor notation is used and the equations are presented in a primitive-variable form. Initial and boundary conditions are also presented in the corresponding sections.

4.2. HYDRODYNAMIC MODELLING

The so-called balance equations of physics represent the fundamental conservation principles of mass, momentum and energy, as applicable to an arbitrary continuous medium. Assuming certain constitutive relationships for Newtonian fluids, and considering other thermodynamic conditions, leads to the formulation of the continuity, momentum and energy conservation equations. These form a closed set of equations that describes exactly the distribution of mean-flow quantities within a *continuum* in local thermodynamic equilibrium and form the common basis of most Computational Fluid Dynamics (CFD) models. Derivation of these equations from the basic principles can be found in Batchelor (1967).

4.2.1 Navier-Stokes equations

In their general form, the Navier-Stokes (NS) equations include all known internal and external effects on the motion of a fluid, some of which are sometimes not important to a particular problem. Thus, it is convenient to apply certain simplifying assumptions and obtain a subset of equations. For instance, the water is generally treated as an incompressible fluid and the influence of Earth's rotation can be disregarded, depending upon the scale of the problem being considered. Temperature changes may also be unimportant within the time scale and boundary conditions of a problem, which allows the continuity and momentum equations to be uncoupled from the energy equation by assuming a constant viscosity and treating pressure as an ordinary variable (i.e., disregarding its thermodynamic nature). These are assumptions often made to model the flow in contact tanks, as shown in previous related modelling work undertaken by Wang (1995).

As heat transfer and other thermal processes are not within the context of this research, the energy equation will not be included herein. The simplified unsteady continuity and momentum equations are therefore given as (Schlichting, 1979): –

$$\frac{\partial U_i}{\partial x_i} = 0 \tag{4.1}$$

$$\frac{\partial U_i}{\partial t} + U_j \frac{\partial U_i}{\partial x_j} = -\frac{1}{\rho}\frac{\partial P}{\partial x_i} + v_l \frac{\partial^2 U_i}{\partial x_i^2} \tag{4.2}$$

where U_i refers to the instantaneous velocity in the i direction, with i assuming values of 1, 2 and 3 for the 3-D case, corresponding to the longitudinal (x), lateral (y) and vertical (z) directions respectively; P is the static pressure; and the fluid properties are ρ as density and ν_1 as the kinematic molecular viscosity, where $\nu_1 = \mu/\rho$ and μ is the dynamic viscosity.

The divergence of the velocity is set to zero, as in Equation (4.1), as governed by the assumption of incompressibility, since it forces the volume of an arbitrary region to be constant, assuming that ρ is also invariable. This later assumption concerning ρ is often valid when a monophasic flow is studied.

In Equation (4.2), the first term on the left-hand side is the transient of the velocity. Often, in modelling flow in contact tanks and other water and wastewater treatment units it is of interest to obtain a steady state solution of the flow field and then apply it to predict the distribution of a solute (Falconer and Ismail, 1997), or compare the hydrodynamic results for different design configurations in optimisation studies (Stamou, 2002). In such circumstances, the transient term can be dropped from the momentum equations and the resulting set solved for as an elliptic, vis-a-vis a parabolic problem.

The second term on the left-hand side of Equation (4.2) represents the advective contribution to the transport of momentum and is responsible for the non-linearity of the NS equations. On the right-hand side of Equation 4.2, the terms include: the pressure gradient in the corresponding ' i ' direction and the diffusive or viscous term.

Two aspects are worth mentioning at this stage. The first relates to the manner in which pressure is regarded in this mathematical model; in that it is kept in the form of a hydrodynamic pressure distribution, as opposed to assuming a hydrostatic pressure distribution. Such an assumption, when adopted, reduces the original 3-D problem to a 2-D-horizontal structured, repeating the process for various layers and estimating the vertical velocity component as a function of the others. This mathematical basis is common to models referred to as "3-D layer-integrated", and has proven to be effective when representing shallow water flows, such as those occurring in most estuarine and coastal regions. Typical examples are the models of Kim and Lee (1994) and Lin and Falconer (1997).

However, when modelling complex 3-D flow fields that may occur in non-optimally designed contact tanks, such as the unit investigated by Teixeira (1993), the hydrostatic pressure distribution assumption could fail to provide an accurate representation of the flow field. This is because, in such cases, strong vertical accelerations may occur in certain regions of the flow field, configuring a hydrodynamic pressure distribution. With this concern in mind, the governing equations in this study have been kept in fully 3-D form, i.e., not assuming a hydrostatic pressure distribution.

The second aspect to be pointed out is the issue of modelling turbulent flows. As commented earlier, the NS equations govern the motion of a fluid within a *continuum*, but it is well known that general analytical solutions for these equations are non-existent to date. In turn, using a numerical approach requires the differential equations to be discretised onto some form of algebraic counterparts, which means that the original

problem is solved for not in a continuous domain, but in certain locations of a computational grid. The modified equations no longer describe exactly the fluid motion and a so-called "closure" model is required to account for the effects of turbulence. Direct numerical simulations of the NS equations are a way to avoid this issue, but their application is rather limited to only a few flow conditions and they still require excessive expensive computational resources, from the engineering viewpoint (see, for instance, de Bruin, 2001).

It is in this context that turbulence modelling contributes towards providing a cost-effective solution for flows of practical engineering interest. It essentially consists of simulating the effects of turbulence on the mean flow quantities, such as velocity and a chemical species concentration, based on a theoretical-empirical approach, as discussed below.

4.2.2 Turbulent flow equations

Two main approaches are found in the literature to model turbulence. One, based on a statistical-temporal representation of the flow quantities, in which the instantaneous value of a variable is split into its mean and fluctuating (turbulent) components. This process is known as Reynolds averaging and is exemplified in Equation (4.3) for velocities, where the velocity is written in terms of a time mean and a fluctuating component to give: −

$$U_i = \overline{U_i} + u_i \qquad\qquad (4.3)$$

where $\bar{U}_i$ represents the time mean component of the actual velocity U_i averaged over a long period compared to the time scale of the turbulent motion and u_i is the corresponding instantaneous fluctuation.

Application of Equation (4.3) to the Navier-Stokes equations leads to the so-called Reynolds averaged NS equations (RANS), giving (Rodi, 1993): –

$$\frac{\partial U_i}{\partial t} + U_j \frac{\partial U_i}{\partial x_j} = -\frac{1}{\rho}\frac{\partial P}{\partial x_i} + \frac{\partial}{\partial x_j}\left(v_i \frac{\partial U_i}{\partial x_j} - \overline{u_i u_j} \right)$$ (4.4)

It should be noted that the mean-value overbar in Equation (4.3) has been omitted in Equation (4.4) for convenience of presentation. In comparing Equations (4.4) and (4.2), the difference (beside U_i standing for the mean velocity and not the instantaneous velocity) is seen to be in the viscous part, with the inclusion of a new term $-\overline{u_i u_j}$.

When multiplied by ρ, this term is known as the Reynolds or turbulent stress. It is known as the Boussinesq concept and is usually expressed as a function of the mean-velocity gradients and the turbulent viscosity, in an analogous manner to the viscous stresses occurring in laminar flows, as (Rodi, 1993): –

$$-\overline{u_i u_j} = v_i \left(\frac{\partial U_i}{\partial x_j} + \frac{\partial U_j}{\partial x_i} \right) - \frac{2}{3}k\delta_{ij}$$ (4.5)

where ν_t is the eddy viscosity, k is the turbulent kinetic energy and δ_{ij} is the Kronecker delta. Thus, Equation (4.4) can be re-written as: –

$$\frac{\partial U_i}{\partial t} + U_j \frac{\partial U_i}{\partial x_j} = -\frac{1}{\rho}\frac{\partial P}{\partial x_i} + \frac{\partial}{\partial x_j}\left[(\nu_t + \nu_t)\frac{\partial U_i}{\partial x_j} \right]$$ (4.6)

where the kinematic and the eddy viscosities are added together to represent the effective viscosity term in the RANS equations. Obtaining the distribution of ν_t within the flow field is the desired outcome of turbulence modelling, based on the Reynolds approach in this study.

4.2.2.1 Depth-averaged eddy viscosity

The use of a depth-averaged eddy viscosity consists of a relatively simple representation of turbulence, which is useful when the flow field can be deemed as two-dimensional in nature, i.e. where only the horizontal transport is important (Rodi, 1993). The calculation of ν_t can then be performed using (Fischer, 1973; Falconer, 1991): –

$$\nu_t = 0.15 U_f H$$ (4.7)

where H is the depth of flow and the friction velocity U_f is computed as: –

$$U_f = \frac{U_0\sqrt{g}}{c}$$ (4.8)

where U_0 is the bulk flow velocity, taken as the flow rate divided by the wetted area of the flow, $g = 9.8\text{m/s}^2$ is the acceleration of gravity and c is the Chezy coefficient, calculated as (French, 1985): –

$$c = \frac{H^{\frac{1}{6}}}{n} \tag{4.9}$$

where n is the Manning's resistance coefficient. The value of n adopted in this study was n = 0.012, which was associated by Chow (1959) to the types of solid surfaces found in the experimentation tank described in Chapter 3.

It can be noticed that, where the water depth and bulk velocity are constant quantities of a problem, then the corresponding value of the depth-averaged eddy viscosity can be calculated only once, at the start of the solution procedure. Then, for the remainder of the numerical simulation this quantity can be treated as a constant parameter.

4.2.2.2 Low Reynolds number k-ε turbulence model

As seen in section 2.5.2, the k-ε model belongs to the category of two-equation turbulence models, in deploying two further transport equations to describe the turbulence quantities.

In this study, a low Reynolds number version of the k-ε model was used to model the turbulence. The model adopted was developed by Lam and Bremhorst (1981), and it is

henceforth referred to as the LB model. Amongst the advantages of the LB model in comparison with other low Reynolds number k-ε models, e.g. the version of Launder and Sharma (1974), is the fact that the LB model includes an equation for the dissipation rate itself, rather than for a modified dissipation rate parameter, which is more attractive from the physical point of view (Patel et al., 1985).

In the LB model, the distributions of the turbulent kinetic energy, k, and its dissipation rate, ε, are computed and then related to the eddy viscosity, by using: −

$$v_t = c_\mu f_\mu \frac{k^2}{\varepsilon}$$ (4.10)

where f_μ is a damping function used to mimic the direct effect of molecular viscosity on the shear stress (Patel et al., 1985), which is given by Equation (4.14); and C_μ is an empirical parameter. In this study two approaches were used to model the parameter C_μ, namely: i) as a constant quantity, for which the value of C_μ is given in Table 4.1; and ii) as a variable quantity, where C_μ was a function of the ratio between the local turbulence production and the dissipation rate (see section 5.3.2).

The turbulence quantities k and ε were respectively computed using the following transport equations: −

$$\frac{\partial k}{\partial t} + U_i \frac{\partial k}{\partial x_i} = \frac{\partial}{\partial x_i}\left[\left(v_l + \frac{v_t}{\sigma_k}\right)\frac{\partial k}{\partial x_i}\right] + G - \varepsilon$$ (4.11)

$$\frac{\partial \varepsilon}{\partial t} + U_i \frac{\partial \varepsilon}{\partial x_i} = \frac{\partial}{\partial x_i}\left[\left(v_i + \frac{v_i}{\sigma_\varepsilon}\right)\frac{\partial \varepsilon}{\partial x_i}\right] + c_{1\varepsilon} f_1 \frac{\varepsilon}{k} G - c_{2\varepsilon} f_2 \frac{\varepsilon^2}{k} \qquad (4.12)$$

where the two terms on the left-hand side respectively represent the transient and advective contributions to the transport of the corresponding turbulent quantity. On the right-hand side of the equations, the first term represents the diffusion and the remaining terms represent the production and destruction of the quantity respectively.

Four empirical constants $c_{1\varepsilon}$, $c_{2\varepsilon}$, σ_k and σ_ε are included in Equations (4.11) and (4.12) and their typical values are shown in Table 4.1. The parameter G is calculated as: –

$$G = v_i \left(\frac{\partial U_i}{\partial x_j} + \frac{\partial U_j}{\partial x_i}\right)\frac{\partial U_i}{\partial x_j} \qquad (4.13)$$

Table 4.1 Recommended values of constants in the k-ε model (from Rodi, 1993)

k-ε model constant	c_μ	$c_{1\varepsilon}$	$c_{2\varepsilon}$	σ_k	σ_ε
Value	0.09	1.44	1.92	1.00	1.30

Further damping functions, i.e. parameters f_1 and f_2, are included in Equation (4.12) as part of the LB model. As well as the parameter f_μ that appears in Equation (4.10), these parameters are modelled as being a function of the turbulence Reynolds number. The values of f_μ, f_1 and f_2 were calculated using: –

$$f_\mu = \left(1 - e^{-0.0165R_y}\right)^2 \left(1 + \frac{20.5}{R_T}\right) \qquad (4.14)$$

$$f_1 = 1 + \left(\frac{0.05}{f_\mu}\right)^3 \qquad (4.15)$$

$$f_2 = 1 - e^{-R_T^2} \qquad (4.16)$$

where R_y and R_T are the turbulence Reynolds numbers, which are calculated using: –

$$R_y = \frac{y\sqrt{k}}{\nu_l} \qquad (4.17)$$

$$R_T = \frac{k^2}{\varepsilon \nu_l} \qquad (4.18)$$

where y is the normal distance to the nearest solid boundary. The value assumed by the damping functions tends to unity in the region away from solid boundaries, for fully turbulent flows (Patel et al., 1985).

4.2.3   Initial and boundary conditions

The hydrodynamic equations were modelled using zero initial conditions, i.e. the value of all variables was set to zero at the start of the simulations, i.e. for t = 0 (Roache, 1998; Patankar, 1980).

The boundary conditions (BC) prescribed in this study for the RANS and k-ε model equations followed definitions of Roache (1998) and were divided into four types, namely: – inlet, solid boundary, outlet and the free surface boundary.

At inlet sections the Neumann BC was specified for the pressure, so that the normal gradient of this variable was zero. The Dirichlet BC was applied for the mean velocity components, so that the value of the mean velocity component in the direction of the main inflow was set equal to the inlet bulk velocity (U_{in}), which was calculated as $U_{in} = Q/A_{in}$, where Q was the flow rate and A_{in} was the inlet cross-section area. The value of the other velocity components was set to zero at the inlet.

The Dirichlet BC was also prescribed for the turbulence quantities. A turbulence intensity of 1% was assumed for the inflow, so that the inlet values of k and ε, i.e. k_{in} and ε_{in}, were calculated using: –

$$k_{in} = 1.5\left(0.01 U_{in}\right)^2 \qquad (4.19)$$

$$\varepsilon_{in} = \frac{c_\mu k_{in}^{1.5}}{0.01 R_{Hin}} \qquad (4.20)$$

where R_{Hin} was the inlet hydraulic radius. The eddy viscosity value for the inflow was calculated using Equation (4.7) and the values of k_{in} and ε_{in}, with $f_\mu = 1$.

At outlet sections the Neumann BC was prescribed for all variables, so that the respective gradient normal to the boundary was set to zero.

At solid boundaries (i.e. the walls and bed) the no-slip, no-flux BC was applied, so that the mean velocities were set to zero (i.e. U = V = W = 0). The Neumann BC was prescribed for the pressure and for ε. The value of k was set to zero at solid boundaries.

The free surface was modelled as a rigid lid, free-surface boundary, so that the value of the mean vertical velocity was set to zero at the surface, i.e. $W|_{z=H} = 0$, while the Neumann BC was applied for the other mean velocity components, as well as for the pressure and k. Therefore, at the free surface these variables were calculated using: –

$$\frac{\partial U}{\partial z}\bigg|_{z=H} = \frac{\partial V}{\partial z}\bigg|_{z=H} = \frac{\partial P}{\partial z}\bigg|_{z=H} = \frac{\partial k}{\partial z}\bigg|_{z=H} = 0 \tag{4.21}$$

where H is the water depth. The value of ε at the free surface was calculated as (Celik and Rodi, 1984): –

$$\varepsilon|_{z=H} = \frac{\left(k|_{z=H}\right)^{1.5}}{0.18H} \tag{4.22}$$

The choice of using Equation (4.22) as the surface BC for ε was made after consideration of the results of Cotton et al. (2003), where this BC was shown to provide a more accurate representation of the eddy viscosity profile along the depth in open-

channel flows, in comparison with other types of BC including the zero-gradient option.

A summary of the types of boundary conditions prescribed for the hydrodynamic equations is shown in Table 4.2.

Table 4.2 Summary of the types of boundary conditions prescribed for the hydrodynamic equations

Type of boundary	Inlet	Outlet	Wall	Surface
Variable	Type of boundary condition			
P	Neumann	Neumann	Neumann	Neumann
U	Dirichlet	Neumann	Dirichlet	Neumann
V	Dirichlet	Neumann	Dirichlet	Neumann
W	Dirichlet	Neumann	Dirichlet	Dirichlet
k	Dirichlet	Neumann	Dirichlet	Neumann
ε	Dirichlet	Neumann	Dirichlet	Dirichlet

4.3. SOLUTE TRANSPORT MODELLING

The modelling of solute transport processes was carried out using the advective-diffusion equation (ADE), as discussed below.

4.3.1 Advection-diffusion equation

The ADE is essentially a conservation equation written for a chemical species, and it is derived similarly to the RANS equations, to give: –

$$\frac{\partial C}{\partial t} + U_i \frac{\partial C}{\partial x_i} = \frac{\partial}{\partial x_i}\left(\lambda \frac{\partial C}{\partial x_i} - \overline{u_i c}\right) \qquad (4.23)$$

where C is the time-mean solute concentration; c the turbulent fluctuation of C; λ the molecular diffusivity of C; and the term $-\overline{u_i c}$, when multiplied by ρ, represents the turbulent mass flux. In analogy to the turbulent transport of momentum, this term is generally assumed to be related to the gradient of the transported quantity (Rodi, 1993), as follows: –

$$-\overline{u_i c} = \Gamma \frac{\partial C}{\partial x_i} \qquad (4.24)$$

where Γ is the turbulent mass diffusivity and is related to the turbulence intensity, rather than being a fluid property. Similarly to Equation (4.6), the ADE can be re-written as: –

$$\frac{\partial C}{\partial t} + U_i \frac{\partial C}{\partial x_i} = \frac{\partial}{\partial x_i}\left[(\lambda + \Gamma)\frac{\partial C}{\partial x_i}\right] \qquad (4.25)$$

where the molecular and turbulent mass diffusivities (i.e. λ and Γ) are added together to represent the effective diffusivity term.

4.3.2 Turbulent Schmidt number

The value of Γ that enters Equation (4.25) is calculated as the ratio between the eddy viscosity v_t and the turbulent Schmidt number σ_t, as follows: –

$$\Gamma = \frac{v_t}{\sigma_t}$$ (4.26)

According to Rodi (1993), it is not unrealistic to adopt a constant value for σ_t, since this parameter has been found to show little variation across a flow, and also from flow to flow (unlike v_t). The value of σ_t was approximated to unity in the numerical simulations of a contact tank by Wang (1995), yielding $\Gamma = v_t$. However, some discrepancies can arise when different values of σ_t are employed (Peplinski and Ducoste, 2002; Shiono et al., 2003). Shiono and Teixeira (2000) suggested that particular attention should be paid as to the value of σ_t when modelling the solute transport processes in a contact tank with complex flow conditions. Therefore, in this study different values of σ_t were tested in the solute transport simulations of contact tanks and an analysis of the sensitivity of the results obtained was carried out, as discussed in Chapter 8.

4.3.3 Initial and boundary conditions

The initial condition prescribed for Equation (4.25) followed the studies of Falconer and Ismail (1997) and Stamou (2002). This included the use of a square step function for the values of C at the inlet section, with zero concentration being set elsewhere for t = 0. The square step function mimicked a quasi-instantaneous release of the tracer at the inlet of a simulation domain (see Chapter 3). Therefore, a uniform solute concentration was set at the inflow (i.e. C_{in}) for a pre-determined period of time (i.e. T_i), and then set to zero for the rest of the simulation time, as illustrated in Figure 4.1.
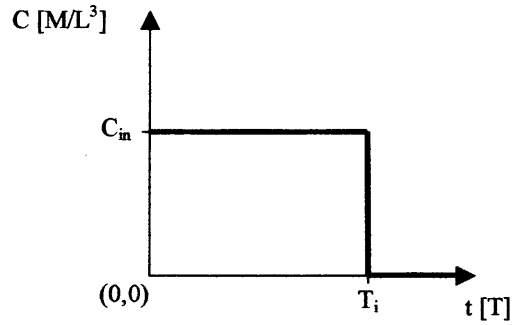
Figure 4.1 Schematic representation of the square step function, illustrating the initial condition used for the mean inlet concentration in the advection-diffusion equation

The boundary conditions (BC) applied for the ADE were classified accordingly to the type of boundary, which were given as: – inlet, solid boundary, free surface and outlet boundary.

At inlet sections, the value of the solute concentration was specified as being zero for time $t > T_i$, which characterised the application of a Dirichlet BC for this type of boundary.

At the free surface and outlet sections the Neumann BC was applied, so that the normal gradient of C at the corresponding boundary was set to zero. Solid boundaries were treated as no-flux surfaces, where the Dirichlet BC was used to specify the zero concentration value at the respective boundary.

4.4. A GENERAL FORMULATION FOR THE TRANSPORT EQUATIONS

The governing equations used to model the transport of flow quantities, such as momentum, k, ε and solute were given by Equations (4.6), (4.11), (4.12) and (4.25)

respectively. As previously discussed in this Chapter, these equations include a number of terms that account for the transient effects on the transport of the corresponding flow quantity, as well as the effects of advection, diffusion and any source terms that may exist in the flow field.

The similarity among the conservation equations allowed a general formulation to be written, which was useful in the derivation of the numerical scheme presented in Chapter 5. Therefore, the general transport equation used was (Patankar, 1980): –

$$\underbrace{\frac{\partial \phi}{\partial t}}_{transient\ term} + \underbrace{U_i \frac{\partial \phi}{\partial x_i}}_{advective\ term} = \underbrace{\frac{\partial}{\partial x_i}\left(D\frac{\partial \phi}{\partial x_i}\right)}_{diffusion\ term} + \underbrace{S}_{source\ term} \tag{4.27}$$

where i = 1, 2, 3 for the x, y and z directions respectively; U_i is the flow mean velocity in the corresponding direction; t is the time; and the parameters ϕ, D and S are specified accordingly to Table 4.3.

Table 4.3 Specification of parameters for the general transport equation, Equation (4.27)

Conservation equation	ϕ: dependent variable	D: diffusion coefficient	S: source term
Momentum	U_i	$v_l + v_t$	$-\frac{1}{\rho}\frac{\partial P}{\partial x_i}$
Turbulent kinetic energy	k	$v_l + \frac{v_t}{\sigma_k}$	$G - \varepsilon$
Dissipation rate	ε	$v_l + \frac{v_t}{\sigma_\varepsilon}$	$c_{1\varepsilon}f_1\frac{\varepsilon}{k}G - c_{2\varepsilon}f_2\frac{\varepsilon^2}{k}$
Advection-diffusion	C	$\lambda + \frac{v_t}{\sigma_t}$	$= 0$

where U_i is the flow mean velocity component in the i direction; C is the time-mean concentration of solute; ρ and ν are the specific mass and kinematic viscosity of the fluid respectively; ν_t is the eddy viscosity; σ_k, σ_ε, $c_{1\varepsilon}$ and $c_{2\varepsilon}$ are constants of the k-ε model; σ_t is the turbulent Schmidt number; P is the pressure; and G is the turbulence generation term, defined as in Equation (4.13). Further details about the derivation and terms of the general transport equation can be found in Patankar (1980) and Rodi (1993).

Summary

In this Chapter the conservation differential equations that govern the transport of mean turbulent flow quantities were discussed. These included the continuity equation, the momentum equations, the turbulent kinetic energy (k) equation and the equation for k's dissipation rate (ε), as well as the advection-diffusion equation for the conservative transport of a chemical species. The governing equations were written using the Cartesian-tensor notation and in a primitive-variable form. Assumptions were made as for the modelling of water as a Newtonian incompressible fluid, while the Earth's rotation was disregarded. A fully three-dimensional approach was adopted, which allows for a hydrodynamic pressure distribution to occur in the flow field. A statistical-temporal strategy was used to model the turbulence effects, while two options to calculate the eddy viscosity were outlined, namely, i) a depth-integrated eddy viscosity formulation; and ii) a low Reynolds number version of the k-ε model. The initial and boundary conditions were prescribed for the governing equations and a general formulation of the transport equation was presented. The discretisation of the governing equations and further details of the numerical method used in this study are discussed in Chapter 5.

Chapter 5

Numerical Modelling

5.1. INTRODUCTION

Details are given herein of the Computational Fluid Dynamics (CFD) model developed and used in the numerical simulations of this study. In section 5.2 the discretisation of the governing equations outlined in Chapter 4 is demonstrated, using the finite volume method on a three-dimensional (3-D) computational grid. Details of the CFD model are given in section 5.3, which include flow charts that illustrate various components of the model. Aspects of the turbulence and solute transport modelling and the line-by-line technique used to solve the systems of discretised equations are also discussed.

5.2. DISCRETISATION OF THE GOVERNING EQUATIONS

The numerical scheme used in the CFD model developed in this study was based on the SIMPLER algorithm of Patankar (1980) and Patankar (1981). As seen in section 2.5.1, in this algorithm the finite volume method (FVM) is used to discretise the governing differential equations into algebraic counterparts, which can then be solved numerically with an appropriate set of boundary conditions. Numerical schemes based on algorithms of the SIMPLE family have been applied successfully to predict complex hydraulic and environmental flow problems (Wu et al., 2000; Olsen et al., 2000; Faure et al., 2004).

A general representation of the discretisation control volumes (CV) in the 3-D computational grid is shown in Figure 5.1a. A projection of this grid on the x-y plan is shown in Figure 5.1b. The central point is represented as point P. Its neighbouring points include the north (N) and south (S) points in the y direction, the east (E) and west

(W) points in the x direction and the top (T) and bottom (B) points in the z direction, in the Cartesian coordinate system.
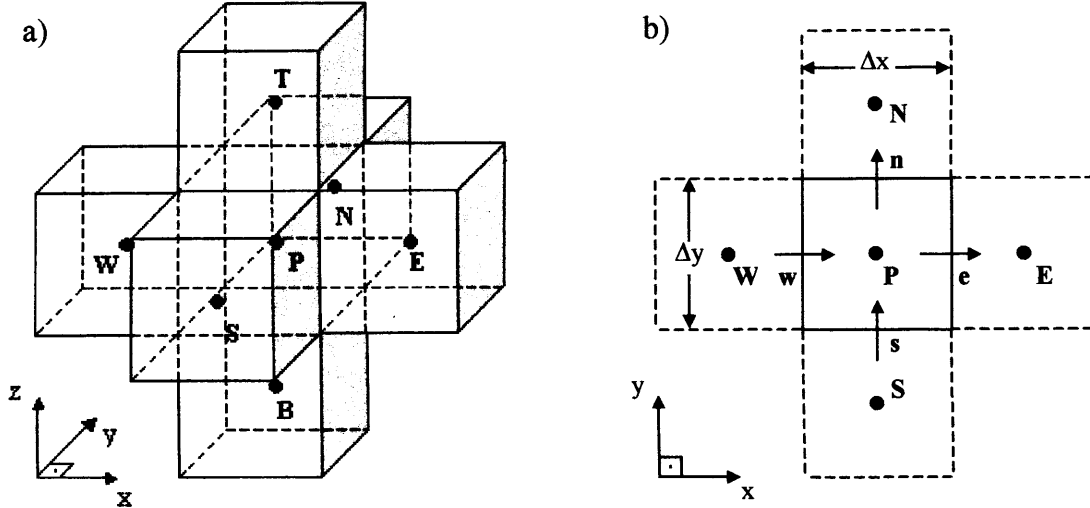
Figure 5.1 General representation of the finite volume discretisation mesh, illustrating:
a) the 3-D computational grid; and b) the corresponding x-y plan projection

5.2.1 General transport equation

The general transport equation, given in Chapter 4 as Equation (4.27) was discretised using the FVM and was written as: –

$$a_P \phi_P = a_E \phi_E + a_W \phi_W + a_N \phi_N + a_S \phi_S + a_T \phi_T + a_B \phi_B + b \tag{5.1}$$

where ϕ stands for the dependent variable; the subscripts P, E, W, N, S, T and B represent the grid points; and a and b are coefficients which include the transient, diffusive, advective and source-term contributions to the transport of ϕ, given as: –

80

$$a_E = D_e A(|P_e|) + \|-F_e, 0\| \qquad (5.2)$$

$$a_W = D_w A(|P_w|) + \|F_w, 0\| \qquad (5.3)$$

$$a_N = D_n A(|P_n|) + \|-F_n, 0\| \qquad (5.4)$$

$$a_S = D_s A(|P_s|) + \|F_s, 0\| \qquad (5.5)$$

$$a_T = D_t A(|P_t|) + \|-F_t, 0\| \qquad (5.6)$$

$$a_B = D_b A(|P_b|) + \|F_b, 0\| \qquad (5.7)$$

$$a_P = a_E + a_W + a_N + a_S + a_T + a_B + a_P^0 - S_P \Delta x \Delta y \Delta z \qquad (5.8)$$

$$b = S_c \Delta x \Delta y \Delta z + a_P^0 \phi_P^0 \qquad (5.9)$$

where the symbol $\|\ \|$ stands for the largest of the two internal quantities; the small-cased indexes refer to the CV faces, as illustrated in Figure 5.1b; Δx, Δy and Δz are the grid spacings; ϕ_P^0 is the previous time step/iteration value of ϕ at the central point; and a_P^0 is a coefficient given by: $-$

$$a_P^0 = \frac{\rho \Delta x \Delta y \Delta z}{\Delta t}$$

(5.10)

where Δt is the time step. The term $a_P^0 \phi_P^0$ is the equivalent of the CV's internal energy.

The source term (S) is expressed as: –

$$S = S_C + S_P \phi_P$$

(5.11)

where Sc and Sp are coefficients of the source term, obtained by using an appropriate

linearisation procedure (Patankar, 1980), as discussed in section 5.4.

The parameters F and D in Equations (5.2) – (5.7) represent flow rates and conductance

across the CV faces, or respectively the advection and diffusion effects in the transport

of ϕ, and are given (for instance, for the CV east face) as: –

$$F_e = \rho u_e \Delta y \Delta z$$

(5.12)

$$D_e = \frac{\Gamma_e \Delta y \Delta z}{(\delta x)_e}$$

(5.13)

where u_e is the velocity component in the x direction, which is computed at face e; Γ_e is

the diffusion coefficient; $\Delta y \Delta z$ is the area of face e; and $(\delta x)_e$ is the distance between

the two grid points involved, i.e. P and E. Similar formulations are deployed for the

other flow rates and conductances, with appropriate changes being made in terms of the corresponding grid locations.

In this study the Power-Law formulation given by Patankar is used as the advection-diffusion scheme in Equations (5.2) to (5.7), so that $A(|P|)$ is given by: –

$$A(|P|) = \left\| 0, (1 - 0.1|P|)^5 \right\|$$
(5.14)

where the Peclet number P is calculated as P = F/D at the corresponding CV face.

The Power-Law scheme has proven to match closely the behaviour of the exponential (exact) scheme, but at a lower computational expense (Patankar, 1980). The Power-Law scheme produces the same effect as that of the hybrid scheme when $|P| > 10$ (i. e. when advection is at least 10 times greater than diffusion), where diffusion is set to zero at high Peclet numbers (thus mimicking a pure upwind formulation). It also reduces to the central difference scheme when Peclet = 0 (Kelkar and Patankar, 1989).

5.2.2 Coupling the continuity and momentum equations

When dealing with the momentum equations, ϕ equates to a mean velocity component which corresponds to the x, y or z direction (see Chapter 4). Since the pressure gradient is regarded as the main source of momentum in these equations (Patankar, 1980), it is often convenient to write the pressure gradient outside the source-term, such that the discretised form of the x-momentum equation on a staggered mesh is: –

$$u_e = \frac{\sum a_{nb} u_{nb} + b}{a_e} + d_e(P_P - P_E)$$

(5.15)

where u_e is the central velocity; the subscript nb stands for the 'neighbour' grid locations (see Figure 5.1); P_P and P_E are the pressures at the points P and E respectively; and d_e is given by: –

$$d_e = \frac{A_e}{a_e}$$

(5.16)

where A_e is the area of the CV face normal to u_e, i.e., $A_e = \Delta y \Delta z$. For the y and z momentum equations, similar formulations are used for v_n and w_t, where the corresponding velocity components are calculated for the north and top faces of the CV respectively. The pressure gradients are $d_n(P_P - P_N)$ and $d_t(P_P - P_T)$; and the interface areas are $A_n = \Delta x \Delta z$ and $A_t = \Delta x \Delta y$.

The diffusion coefficient Γ in the momentum equations is taken as the effective viscosity at the CV face, which is obtained by adding the kinematic viscosity (v_l) to the eddy viscosity (v_t). This procedure avoids having a source-term included in the momentum equations, which is what would occur if the Reynolds stresses were to be directly used to represent turbulence. Thus, since the pressure-gradient term is explicitly represented in equations such as Equation (5.15), the source-term components S_P and S_c in Equations (5.8) and (5.9) can be set to zero, which generally contributes to the stability of the method.

The sequence of operations involved in solving the mean velocity and pressure fields using the SIMPLER algorithm is described below.

The first step of the algorithm applied to the momentum equations is the computation of a pseudo-velocity (i. e. $\hat{u}_e$ in the x direction) by simply dropping the pressure term in Equation (5.15), such that: –

$$\hat{u}_e = \frac{\sum a_{nb} u_{nb} + b}{a_e}$$

(5.17)

The pseudo-velocities are computed explicitly from the neighbouring velocities, which, during the iterative solution process, correspond to the velocity values obtained at the end of the previous iteration or time step. Similar formulations to Equation (5.17) can be derived for $\hat{v}_n$ and $\hat{w}_t$ using the y and z velocity components. After the $\hat{u}_e$, $\hat{v}_n$ and $\hat{w}_t$ velocity fields have been calculated they are used to determine the starred-pressure P* field using: –

$$a_P P_P^* = a_N P_N^* + a_S P_S^* + a_E P_E^* + a_W P_W^* + a_T P_T^* + a_B P_B^* + b$$

(5.18)

where, for incompressible, monophase flows, b is given by: –

$$b = \rho\left[\left(\hat{u}_w - \hat{u}_e\right)\Delta y \Delta z + \left(\hat{v}_s - \hat{v}_n\right)\Delta x \Delta z + \left(\hat{w}_b - \hat{w}_t\right)\Delta x \Delta y\right]$$

(5.19)

which is obtained after substituting the continuity equation into the momentum equation. The pressure coefficients are computed (for instance, for point E) as: –

$$a_E = \rho d_e \Delta y \Delta z \qquad (5.20)$$

with similar formulations being used for the other neighbouring points. The central point coefficient is given by: –

$$a_P = a_E + a_W + a_N + a_S + a_T + a_B \qquad (5.21)$$

After the P* field is determined, then the momentum equation, i.e. Equation (5.15) is used to calculate the starred-velocity field u_e^*, and similarly for v_n^* and w_t^*. A further (corrected) pressure field P' must then be calculated by again using Equation (5.18). However, the starred velocities are included in Equation (5.19) instead of pseudo-velocities. Finally, the pressure-correction and starred-velocity fields are used to determine the actual velocities based on the following formulations: –

$$u_e = u_e^* + d_e \left(P_P^{'} - P_E^{'} \right) \qquad (5.22)$$

$$v_n = v_n^* + d_n \left(P_P^{'} - P_N^{'} \right) \qquad (5.23)$$

$$w_t = w_t^* + d_t \left(P_P^{'} - P_T^{'} \right) \qquad (5.24)$$

A flow chart for the sequence of operations described above is shown in Figure 5.2. The solution process is repeated until a converged solution has been reached. This is determined by a convergence parameter, which signals the end of the iterative loop, as outlined in section 5.2.
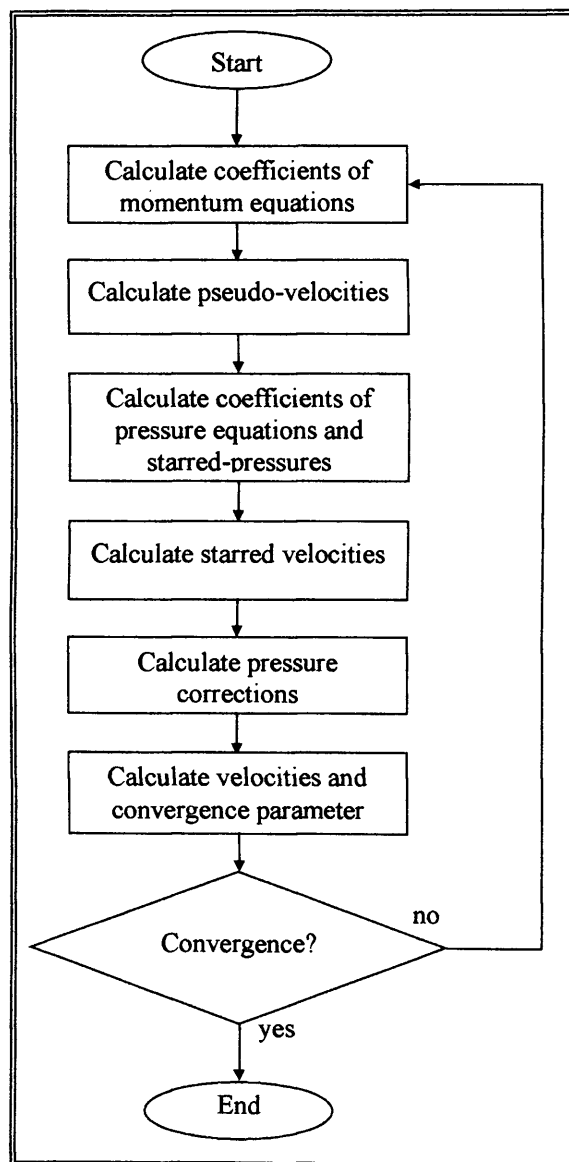
Figure 5.2 Flow chart illustrating the sequence of operations of the solution algorithm for the momentum equations in the numerical model

5.3. NUMERICAL MODEL DETAILS

The CFD model has been developed using Fortran 90 and comprises three main parts: the pre-processor, the main solver and the post-processor.

5.3.1 Pre-processor module

In the pre-processor module the problem characteristics are specified, so that a computational grid that represents the fluid domain and the corresponding types of boundaries can be created.

A mesh generator programme capable of creating regular, orthogonal, non-uniform grids was developed and included in this module. This programme receives as inputs the geometrical features of the domain to be simulated, such as length, width, depth, as well as the location and dimensions of the inlet and outlet sections, number and size of baffles. The mesh features are specified as including the finest and coarsest spacings to be used in each direction and the corresponding gradient to be applied to conform the non-uniform mesh. The use of a relatively smooth mesh spacing variation is recommended, since it generally contributes towards controlling the local truncation errors of the numerical simulation (Beier et al., 1983).

Using the input data the mesh generator programme calculates the mesh spacings, giving as outputs the number of cells and the array of grid spacings in each direction, and a map of indexes identifying all types of cells within the grid, adapted from Falconer et al. (1999). These can be: wet, dry, 'air', inlet or outlet. Dry cells represent

solid boundaries, which include walls, bed and baffles. Air cells are located above the surface. Together with inlet and outlet cells, these allow the main solver to identify which boundary conditions to apply around the wetted domain. A flow chart showing the sequence of operations performed by the mesh generator programme is given in Figure 5.3. An example of a non-uniform mesh calculated by the mesh generator programme for a 2-D corner bend is shown in Figure 5.4.

```
                    ( Start )
                       │
                       ▼
            ┌──────────────────────┐
            │ Read geometrical     │
            │ features of problem  │
            └──────────────────────┘
                       │
                       ▼
            ┌──────────────────────┐         ┌──────────────────────┐
            │ Read desired features│◄────────│                      │
            │ for computational mesh│        │                      │
            └──────────────────────┘         │                      │
                       │                      │                      │
                       ▼                      │                      │
            ┌──────────────────────┐   ┌──────────────────────┐
            │ Calculate grid spacings│  │ Send warning to screen:│
            └──────────────────────┘   │ Adjust grid features  │
                       │                └──────────────────────┘
                       ▼                          ▲
                  ╱ Able to fit ╲   no            │
                 ╱ the domain with  ╲─────────────┘
                 ╲ desired grid      ╱
                  ╲ features?       ╱
                       │ yes
                       ▼
            ┌──────────────────────┐
            │ Generate domain map  │
            │ with cells indexes   │
            └──────────────────────┘
                       │
                       ▼
            ┌──────────────────────┐
            │ Calculate distances from│
            │ cells to nearest wall │
            └──────────────────────┘
                       │
                       ▼
            ┌──────────────────────┐
            │ Write to output files │
            └──────────────────────┘
                       │
                       ▼
                    ( End )
```
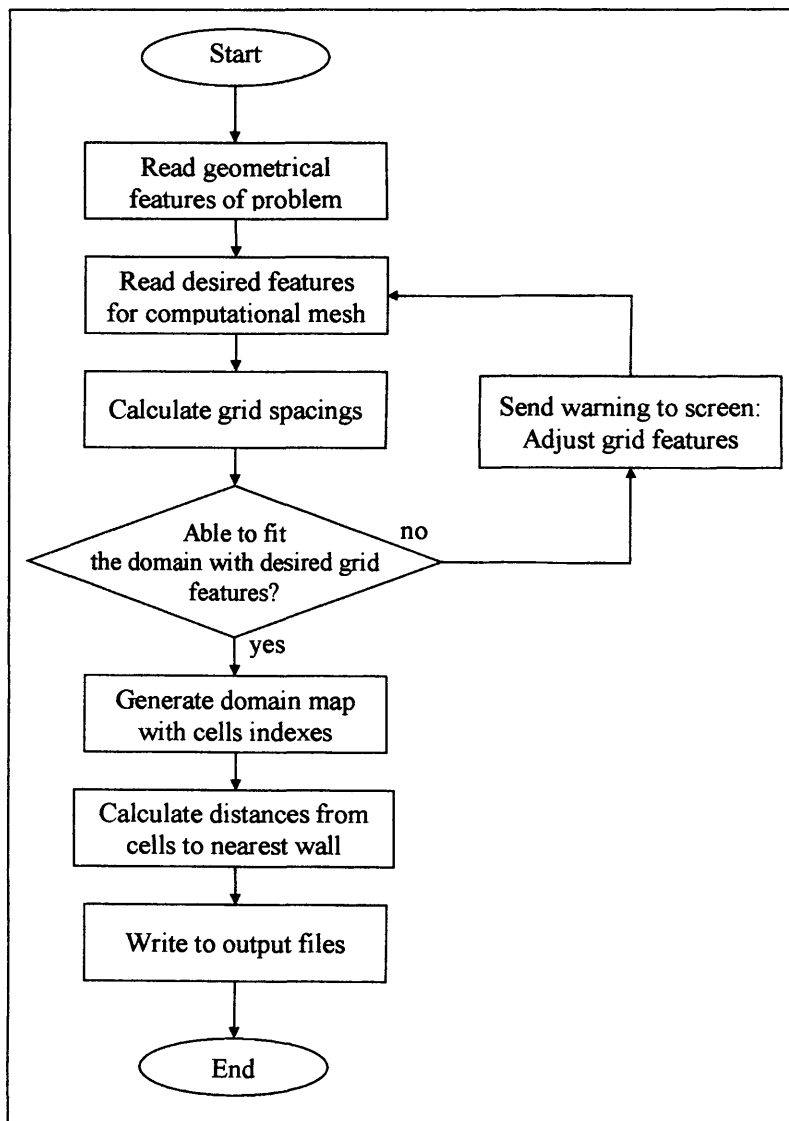
Figure 5.3 Flow chart illustrating the sequence of operations performed by the mesh generator programme
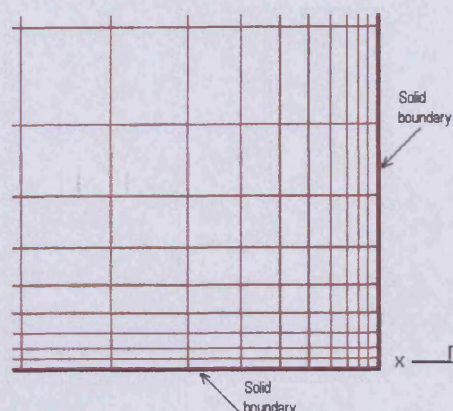
Figure 5.4 Example of a non-uniform mesh calculated for a 2-D corner bend

5.3.2 Main solver

The main solver includes the hydrodynamic module (HM), which is used to solve the turbulent flow field, and a solute transport module (STM), which calculates parameters related to the hydraulic efficiency of the simulated unit. A flow chart for the main solver is shown in Figure 5.5.

The primary task of the HM is to generate the velocity field and the distribution of the eddy viscosity in the tank, by obtaining a steady-state solution for a given flow rate, and within the computational domain provided by the pre-processor. Input parameters for the HM include: the acceleration of gravity, fluid density and kinematic viscosity, the flow rate, the type of turbulence representation to be used, i.e. the k-ε turbulence model or the depth-averaged eddy viscosity (see section 4.2.2). The HM can support either a 'cold start', where all variables in the flow field are initially set to zero, or a 'warm start' in which case the calculations develop from a previously computed flow field. Further details about the main solver features are given below.
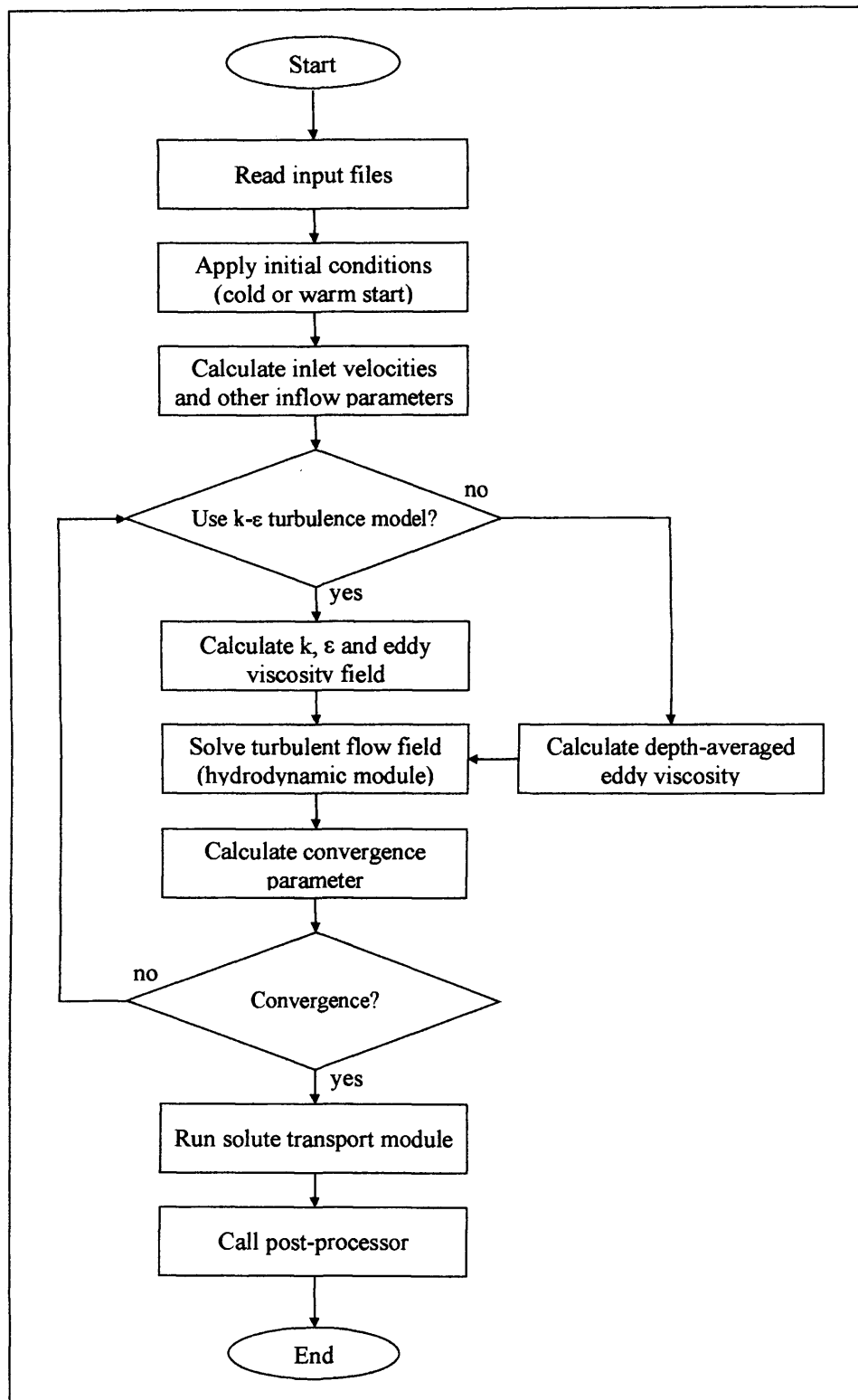
Figure 5.5 Flow chart illustrating the sequence of operations of the main solver

The distribution and magnitude of the mean velocities at outlet sections are calculated using the zero-gradient boundary condition at this location, as seen in section 4.2.3. It is then necessary to compute the flow rate at the outlet, in order to evaluate whether the mass conservation principle is satisfied at the end of the iterative solution process.

For calculating the outflow (q_{out}), a group of internal CV located just upstream of the outlet section are considered. The normal velocity components at each CV face are multiplied by the corresponding cross-section area and then added together to give the net flow rate at the outlet, as exemplified in Figure 5.6.
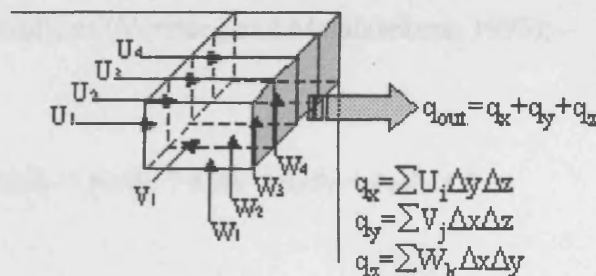
Figure 5.6 Schematic representation of the velocity components and control volume faces involved in the computation of the outflow by the numerical model

The ratio of the outflow to the inflow values, i.e. the ratio between the flow rates calculated at the outlet section and specified at the inlet section of the computational domain is used as the convergence parameter for the hydrodynamic module described above. The solution process for the steady state mean velocity field is stopped when the ratio of the outflow to the inflow becomes asymptotic at 1.

5.3.2.2 Line-by-line solution technique

For the computation of the flow field quantities, the respective discretised equation expressed in a 3-D domain involves 7 unknowns, since it relates the central point value of the variable to the values of the corresponding 6 neighbours. The resulting system of equations is then solved by the numerical model using a semi-implicit approach, known as the line-by-line method. This method involves splitting the original 3-D problem into a series of 1-D problems, thus reducing the number of unknowns at each sweep from 7 to 3. This is achieved by treating implicitly the points located in one direction at a time, while taking all other neighbouring values explicitly, similarly to the Alternating Direction Implicit (ADI) method. Thus, the general discretised transport equation, Equation (5.1), is re-written in the forms corresponding to the sweeps in the x, y and z directions respectively, as (Versteeg and Malalasekera, 1995): –

$$-a_E \phi_E + a_P \phi_P - a_W \phi_W = a_N \phi_N + a_S \phi_S + a_T \phi_T + a_B \phi_B + b \qquad (5.25)$$

$$-a_N \phi_N + a_P \phi_P - a_S \phi_S = a_E \phi_E + a_W \phi_W + a_T \phi_T + a_B \phi_B + b \qquad (5.26)$$

$$-a_T \phi_T + a_P \phi_P - a_B \phi_B = a_N \phi_N + a_S \phi_S + a_E \phi_E + a_W \phi_W + b \qquad (5.27)$$

which can be solved in a sequential manner throughout the computational domain, by applying the appropriate set of boundary conditions and using the Tri-Diagonal Matrix Algorithm (TDMA) (Tannehill et al., 1997). In this method the systems of equations are firstly represented in the upper tridiagonal matrix form, by applying Gaussian

elimination. This is followed by back-substitution, which then gives the solution for the system of equations of the corresponding line. The numerical loop is advanced to the next line of cells and the process is repeated until the external boundary is reached. The implicit direction is then swept and the other corresponding directions are treated explicitly, until the x, y and z sweeps have been performed. Further details of the TDMA method and the numerical routine used to solve the tridiagonal systems of equations in this study are given by Tannehill et al. (1997).

It is worth of mention that, whenever a Neumann boundary condition is involved in a line-by-line sweep, then it is necessary to equate the corresponding boundary value of the variable to the value calculated for the internal neighbouring grid cell, after the back substitution process is performed. This is a necessary update of the domain, in preparation for the subsequent sweep of the solution algorithm.

5.3.2.3   Computation of the interface viscosity

In solving the discretised momentum equations, i.e. Equations (5.22) – (5.24), the associated coefficients involve viscosity values that are taken at CV faces in the staggered computational grid, as shown in Equation (5.13). When a uniform viscosity field is involved in solving the hydrodynamic flow field, e.g. when the turbulence is represented by a depth-averaged eddy viscosity approach, then the interface values of this parameter can simply be equated to the value originally calculated for CV centres (see section 4.2.2).

However, when the k-ε turbulence model is used, a non-uniform eddy viscosity distribution is normally obtained from the calculated k and ε fields, where the viscosity values computed for the CV centres need to be interpolated in order to give the corresponding interface values. Therefore, the procedure proposed by Patankar (1980) was used in this study for such a purpose. Using this method, the viscosity value at the east face of a CV can be calculated as: –

$$v_e = \left(\frac{1-f_e}{v_P} + \frac{f_e}{v_E} \right)^{-1}$$

(5.28)

where f_e is the interpolation factor, given by: –

$$f_e = \frac{(\delta x)_{e+}}{(\delta x)_e}$$

(5.29)

where $(\delta x)_{e+}$ and $(\delta x)_e$ are the grid distances involved in the interpolation procedure, as shown in Figure 5.7.
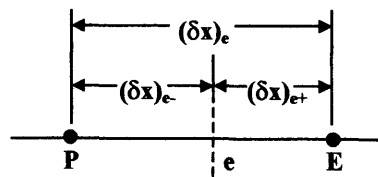
Figure 5.7 Schematic representation of the grid distances associated with the calculation of the interface viscosity

As pointed out by Patankar (1980), when the interface is placed midway between points P and E, i.e. when the values of $(\delta x)_{e+}$ and $(\delta x)_e$ coincide, then equation (5.28) reduces to the harmonic mean between v_P and v_E, and not to the arithmetic mean that would result from assuming a linear variation of v between points P and E.

5.3.2.4 Source term linearisation

Following recommendations of Patankar (1980), the source terms of the k and ε equations were linearised using a procedure described in this section. This was regarded as a necessary step to guarantee the stability of the numerical method.

The source-terms of the k and ε equations, i.e. S^k and S^ε respectively, were given in Table 4.3 as being: –

$$S^k = G - \varepsilon \tag{5.30}$$

$$S^\varepsilon = c_{1\varepsilon} f_1 \frac{\varepsilon}{k} G - c_{2\varepsilon} f_2 \frac{\varepsilon^2}{k} \tag{5.31}$$

where G is the turbulence generation term, defined as in Equation (4.13); $c_{1\varepsilon}$ and $c_{2\varepsilon}$ are constants of the k-ε model, as shown in Table 4.1.

In the linearisation procedure used, Equation (4.10) was firstly rearranged as: –

$$\varepsilon = c_\mu f_\mu \frac{k^2}{v_t}$$

(5.32)

which was substituted for ε into Equations (5.30) and (5.31), to give: –

$$S_k = G - c_\mu f_\mu \frac{k}{v_t} k$$

(5.33)

$$S_\varepsilon = c_{1\varepsilon} f_1 c_\mu f_\mu \frac{k}{v_t} G - c_{2\varepsilon} f_2 c_\mu f_\mu \frac{k}{v_t} \varepsilon$$

(5.34)

Thus, the source term coefficients to be included in Equations (5.8) and (5.9) as part of the discretised transport equation for k are: –

$$S_C^k = G$$

(5.35)

and

$$S_P^k = -c_\mu f_\mu \frac{k}{v_t}$$

(5.36)

Likewise, the source term coefficients for the discretised transport equation for ε read:–

$$S_C^\varepsilon = c_{1\varepsilon} f_1 c_\mu f_\mu \frac{k}{v_t} G$$

(5.37)

and

$$S_P^\varepsilon = -c_{2\varepsilon} f_2 c_\mu f_\mu \frac{k}{v_t}$$

(5.38)

5.3.2.5 Computation of variable C_μ

The use of C_μ as a constant quantity of the k-ε turbulence model (where C_μ = 0.09) is

generally recommended to simulate high Reynolds number flows, where the production

and dissipation of the turbulent kinetic energy are in approximate balance (Rodi, 1993).

However, where the viscous effects play an important role locally in the flow, such as in

the viscous sublayer near walls, Rodi proposed that C_μ should be modelled as a function

of the ratio between the turbulence production and dissipation quantities [i.e. C_μ =

$f(\overline{P/\varepsilon})$], as illustrated in Figure 5.8a.
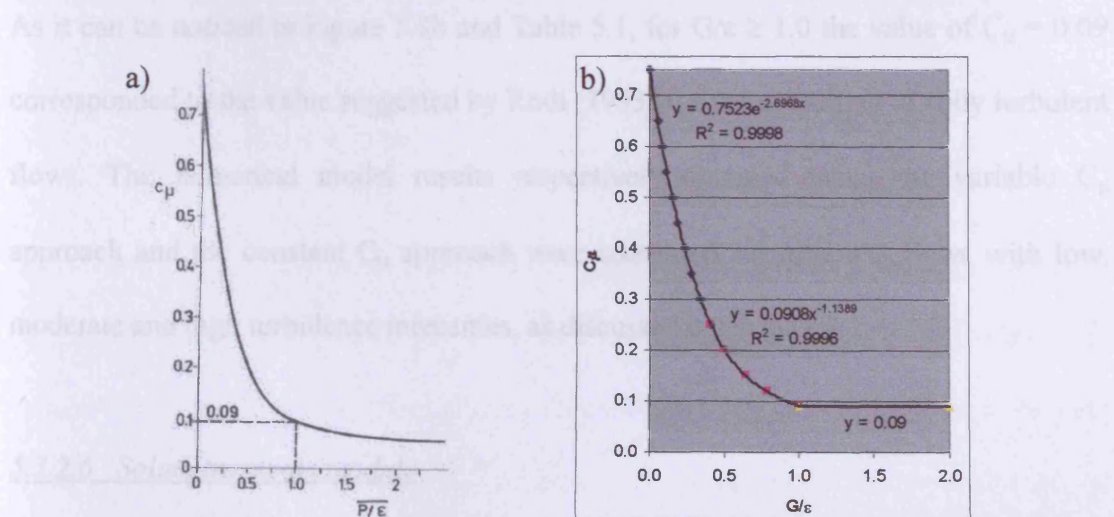
Figure 5.8 Variation of C_μ as a function of the ratio between turbulence production and dissipation, as in: a) empirical correlation function (from Rodi, 1993); and b) approximation using least squares regression functions

In this study the numerical simulations carried out using C_μ as a variable quantity in the

low Reynolds number k-ε model were performed using the regression functions of

Figure 5.8b, which provided the best fit for the empirical curve of Figure 5.8a. The term

$\overline{P/\varepsilon}$ from the empirical curve was substituted by G/ε, where the overbar was dropped

for convenience and the turbulence production term was represented by G [see Equation

(4.13)]. The least square regression functions obtained for the function $C_\mu = f(G/\varepsilon)$ and

the corresponding coefficients of determination are shown in Table 5.1.

Table 5.1 Least square regression functions for the function $C_\mu = f(G/\varepsilon)$

Interval of G/ε	Regression function	Coefficient of determination
G/ε ≤ 0.41	$C_\mu = 0.7523e^{-2.6968(G/\varepsilon)}$	$R^2 = 0.9998$
0.41 < G/ε < 1.0	$C_\mu = 0.0908(G/\varepsilon)^{-1.1389}$	$R^2 = 0.9996$
G/ε ≥ 1.0	$C_\mu = 0.09$	---

As it can be noticed in Figure 5.8b and Table 5.1, for G/ε ≥ 1.0 the value of $C_\mu = 0.09$

corresponded to the value suggested by Rodi (1993) for the modelling of fully turbulent

flows. The numerical model results respectively obtained using the variable C_μ

approach and the constant C_μ approach were compared for turbulent flows with low,

moderate and high turbulence intensities, as discussed in Chapter 7.

5.3.2.6   Solute transport module

Once the mean velocity and eddy viscosity fields have been computed using the

hydrodynamic module, these results can then be used to obtain temporal and spatial

distributions of a solute within the fluid domain. This was done in this study so as to simulate the tracer experiments described in Chapter 3.

Input parameters for the STM include the total simulation time, the time step, the wetted volume, the mass of solute and the duration of the simulated solute injection. The initial and boundary conditions for the STM were given in Chapter 4.

The modelling of solute transport is carried out based on equations (5.1) – (5.14), with the parameter ϕ assuming the time-mean solute concentration, C. When a conservative substance is considered, the source-term quantities S_c and S_p are both set to zero.

At the end of each time step of the solution procedure the average outlet concentration is calculated and used to determine the mass of tracer that has exited the unit during that iteration cycle. It is also used to produce data for the retention time distribution curve and associated hydraulic efficiency indexes, which were described in Chapter 3.

5.3.3 Post-processor module

Once the solutions have been completed through the main solver, the post-processor module generates output files in the appropriate format to be analysed using data visualisation and processing programmes. This includes the mean velocity and the eddy viscosity fields, the time-mean solute transport results and animation scenarios of the transient 3-D solute dispersion in the modelled flow field. An example of animation scenarios generated with data from transient solute transport results for a generic contact tank with 4 compartments is shown in Figure 5.9.
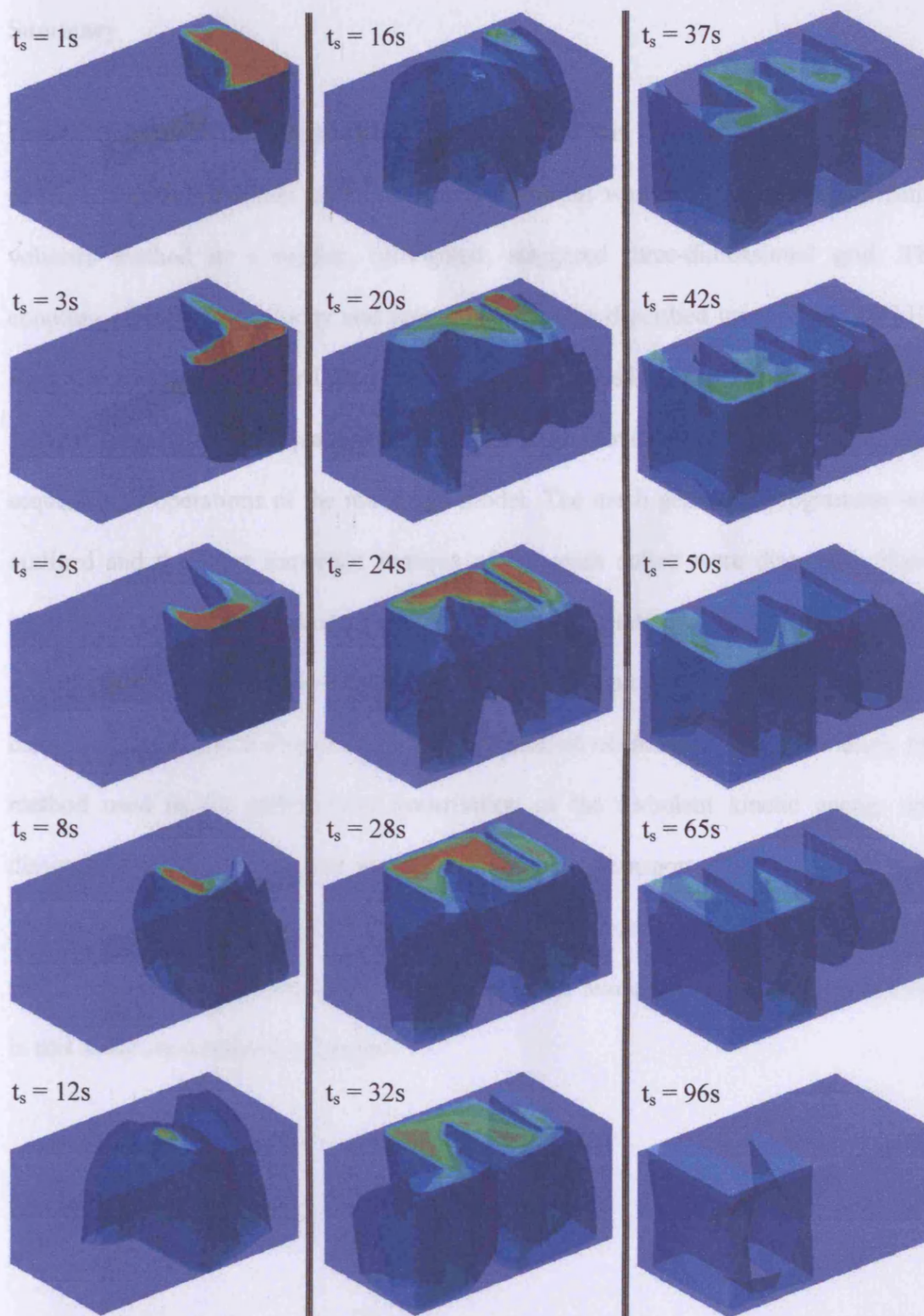
Figure 5.9 Animation scenarios at various simulation times (t_s) created using results of the solute transport module for a generic contact tank with 4 compartments

Summary

Details of the numerical model that was developed in this study were discussed in this Chapter. The discretisation of the governing equations was performed using the finite volumes method in a regular, orthogonal, staggered three-dimensional grid. The coupling of the mean velocity and pressure fields was described using the SIMPLER algorithm, with the Power-Law formulation being used as the advection-diffusion scheme for the transport equations. Flow charts were provided that illustrated the main sequences of operations of the numerical model. The mesh generator programme was outlined and the most important features of the main solver were discussed. These included: the calculation procedure used to obtain the solution convergence parameter; an explanation of the line-by-line solution technique deployed to solve the systems of discretised equations; a discussion on the computation of interface viscosity values; the method used in the source term linearisation of the turbulent kinetic energy and dissipation rate equations; and aspects of the solute transport modelling. The post-processor module of the programme creates output files to be analysed using data visualisation and processing softwares. Results of the numerical simulations carried out in this study are discussed in Chapter 7.

Chapter 6

Physical Experimentation Results

6.1. INTRODUCTION

Results from the physical experimentation work are discussed herein. Velocity measurements were undertaken using an Acoustic Doppler Velocimeter (ADV) and tracer experiments were carried out using a digital fluorometer for a number of design configurations of the Prototype Tank (PT), with the main aims being: i) to provide data for the verification and validation of numerical models, such as the model described in Chapter 5; and ii) to obtain a better understanding of the hydrodynamic and mixing processes in chlorine contact tanks. The results of the mean velocity fields measured using the ADV are discussed in Section 6.2, with a characterisation of the solute transport processes and an analysis of the hydraulic efficiency of the assessed setups of the PT being given in Section 6.3.

6.2. CHARACTERISATION OF MEAN VELOCITY FIELDS

The results presented in this section were obtained using the three-dimensional ADV, giving velocity fields for the PT. The design setups of the PT assessed using the ADV included the following configurations: – OS-C, OS-P, MS3, MS4-C and MS4-P, with the design specifications and schematic representations of these setups being given in Chapter 3. A summary of the main design characteristics of these configurations is given in Table 6.1, where the orientation of compartments is indicated relatively to the main direction of the inflow.

In Section 6.2.1 the flow field is characterised in terms of mean velocity distributions acquired in four assessment groups for setups OS-C and OS-P. The results for setups

MS4-C and MS4-P are discussed in Section 6.2.2, with the mean velocity fields measured in setup MS3 being shown in Section 6.2.3.

Table 6.1 Summary of main design specifications of assessed setups of the Prototype Tank

Setup	Inlet type	Number of compartments	Orientation of compartments
OS-C	Channel	8	Longitudinal
OS-P	Pipe	8	Longitudinal
MS1	Pipe	6	Longitudinal
MS2	Pipe	4	Longitudinal
MS3	Pipe	1	---
MS4-C	Channel	6	Transversal /
MS4-P	Pipe	6	Longitudinal

6.2.1 Original Setup of Prototype Tank

The results for four sets of ADV assessments undertaken in this setup are discussed below. Comparisons have been made with the results obtained by Teixeira (1993), who carried out an extended analysis of the flow field assessed by use of a Laser Doppler Anemometer (LDA) in a contact tank with similar design characteristics to the setup OS-C.

6.2.1.1 Assessment OS-A1

Assessment OS-A1 was carried out in a vertical plane located at the mid-width centre of compartment 1 of setup OS-C. A cross-section devised for the velocity measurements in this region was formed by 312 grid points, where the grid spacing varied from 25mm to

150mm. Results are shown in Figure 6.1, where the longitudinal and vertical length scales, i.e. X and Z respectively, were normalised by the water depth (H), where H = 1010mm. Resultant velocities were calculated from the corresponding longitudinal and vertical components. The inlet section is indicated by an inflow arrow in Figure 6.1a, with the relative location of the walls W1 and W3, the compartment bed and free surface also being shown in this Figure.

Figure 6.1a shows a vector plot of the normalised mean resultant velocities obtained for Assessment OS-A1, while iso-velocity contour plots of the corresponding longitudinal and vertical velocity components are shown in Figures 6.1b and 6.1c. It can be seen from Figure 6.1a that a significant vertically reversed flow zone was the dominating feature of the flow field in Compartment 1 of setup OS-C. The upper layers of the water column, i.e. where $z/H > 0.9$, were occupied by a jet flow structure, originating from the inlet section and where the maximum magnitude of the streamwise velocities corresponded to 900% of the bulk velocity (i.e. $U_0 = 1.0$cm/s). The flow was deflected by wall W3 and by the compartment bed to form the recirculating flow structure. The flow reversed velocities near the bed of Compartment 1 had a maximum magnitude of 350% of U_0, as shown in Figure 6.1b. The maximum magnitude of the vertical velocity component was 500% of U_0 near wall W3, and as shown in Figure 6.1c.

A second, relatively small vertical recirculation zone occurred in this cross-section, located at the corner bend formed by wall W1 and the compartment bed. This corner eddy rotated in the opposite direction relatively to the main vertical recirculation of Compartment 1, as shown in Figure 6.2a.
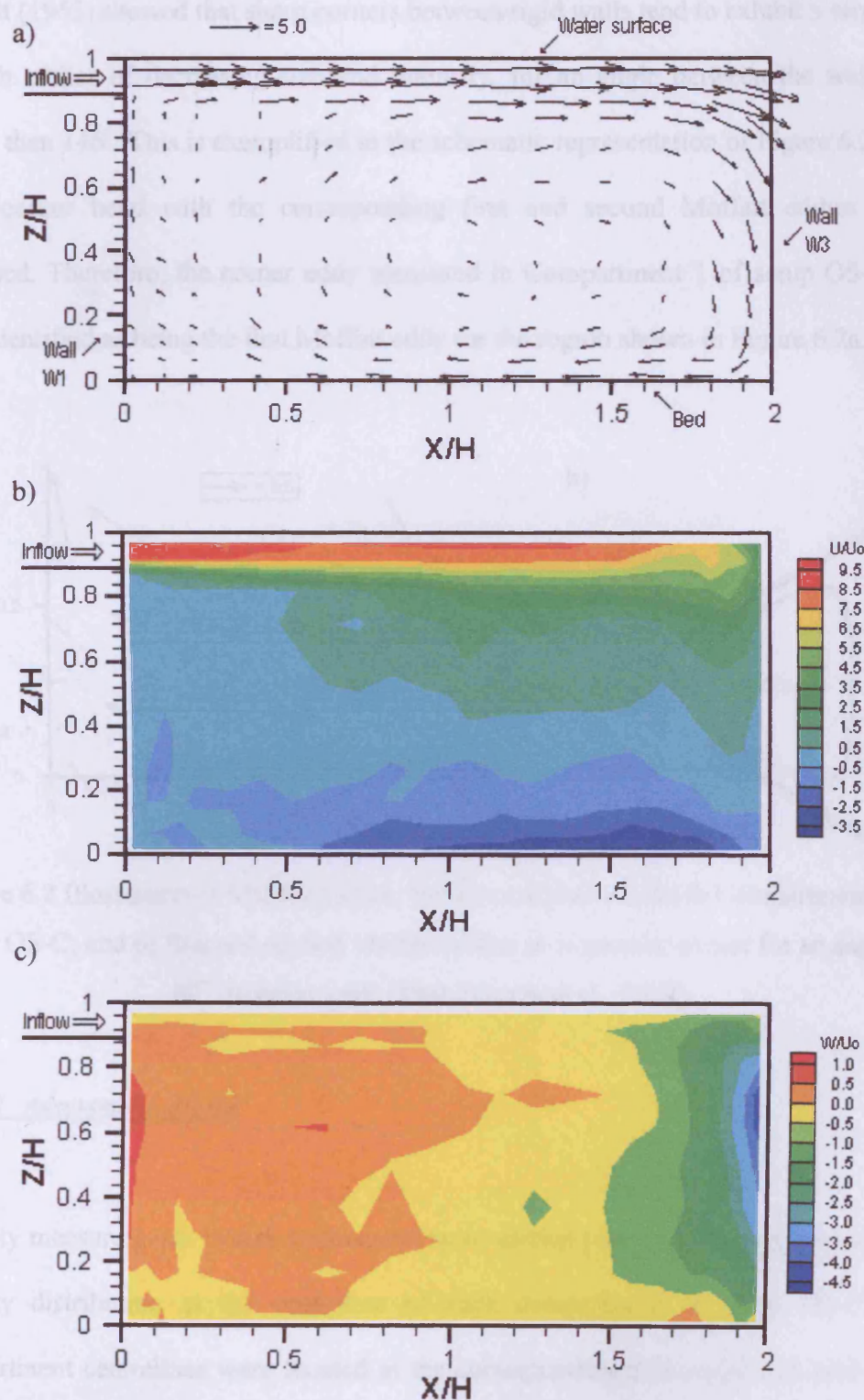
Figure 6.1 Normalised mean velocities measured in Assessment OS-A1 for: a) Vector plot of the resultant velocity field; b) U/U_0 iso-velocity contours; and c) W/U_0 iso-velocity contours

Moffatt (1963) showed that sharp corners between rigid walls tend to exhibit a sequence of such eddies of decreasing size and intensity, for an angle between the walls not higher than 146°. This is exemplified in the schematic representation of Figure 6.2b, for a 60°-corner bend with the corresponding first and second Moffatt eddies being indicated. Therefore, the corner eddy measured in Compartment 1 of setup OS-C has been identified as being the first Moffatt eddy for the region shown in Figure 6.2a.
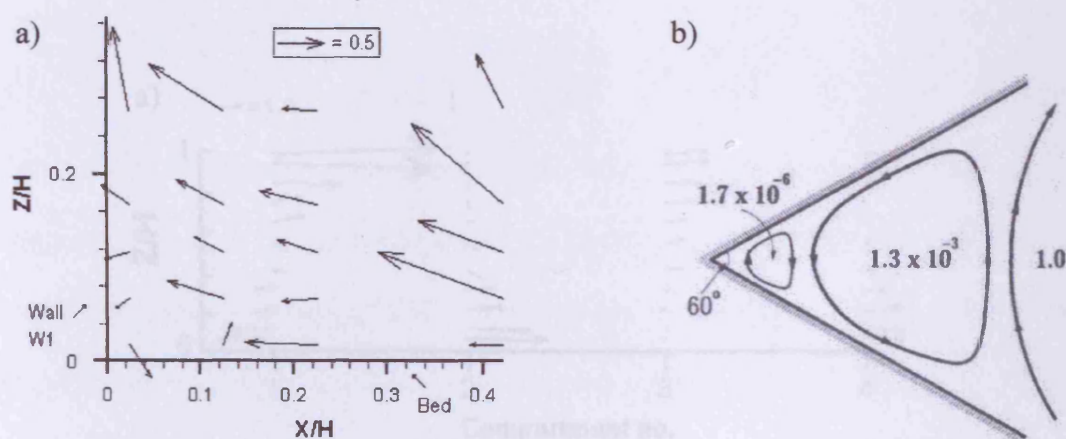
Figure 6.2 Illustration of Moffatt eddies, for: a) measured results in Compartment 1 of setup OS-C; and b) first and second Moffatt eddies in a concave corner for an angle of 60° between walls (from Biswas et al., 2004)

6.2.1.2   Assessment OS-A2

Velocity measurements in this Assessment were carried out to characterise the vertical velocity distribution at the centreline of each compartment of setup OS-C. The compartment centrelines were located at the corresponding mid-length and mid-width positions. A total of 11 sampling points were located along each centreline, where the grid spacing values varied between 50mm and 125mm, and the first grid point was situated 25mm away from the tank bed.

The results for this Assessment are shown in Figure 6.3, where the horizontal axis indicates the compartment number, and the vertical axis represents the normalised depth. The resultant velocities shown in this vector plot were calculated from the U and W components and were normalised by U_0. Streamwise velocity vectors indicated in the Figure point towards the following corresponding compartment. Figure 6.3a shows the mean velocity profiles of centrelines in Compartments 1 to 4, while the corresponding results for Compartments 5 to 8 appear in Figure 6.3b.
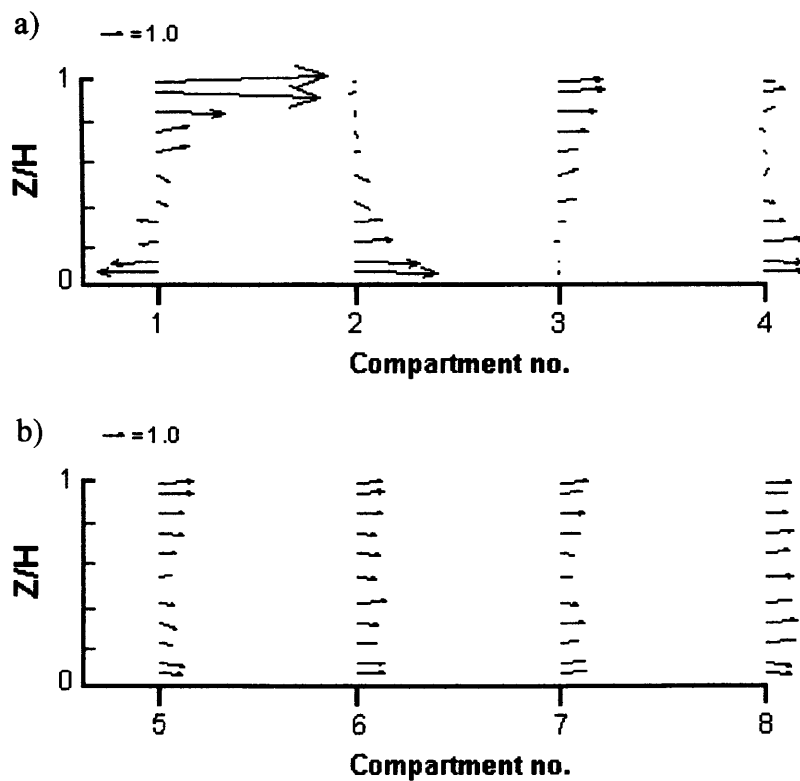
Figure 6.3 Vertical profiles of mean normalised velocities measured along compartment centrelines of setup OS-C for: a) Compartments 1 to 4; and b) Compartments 5 to 8

The results in Figure 6.3a indicate that vertically reversed flow velocities occurred in Compartments 1 to 4. Along the corresponding centrelines, the region of occurrence of the maximum streamwise velocity was found to alternate between the upper and the

lower layers of the water column. Hence, in odd-numbered compartments (i.e. 1 and 3) the respective maximum velocity occurred near the surface, within the region of z/H > 0.9, while in even-numbered compartments (i.e. 2 and 4), the respective maximum velocity occurred near the compartment bed, i.e. within the region z/H < 0.1. This effect was a consequence of the inflow jet and the flow deflection caused by tank walls (Teixeira, 1993). The maximum magnitude of the mean streamwise flow velocities along the centrelines of Compartments 1 to 4 corresponded to 860%, 400%, 220% and 190% of U_0 respectively.

It can be seen in Figure 6.3b that streamwise flow occurred along the centrelines of compartments 5 to 8. In the centreline of Compartment 5, the maximum streamwise velocity occurred in the region z/H > 0.9 and was of the order of 170% of U_0. For Compartments 6 to 8, no trend could be detected for the region of occurrence of the maximum streamwise velocity.

An analysis of the flow uniformity along the vertical direction was carried out using the mean velocity distributions from Assessment OS-A2. A deviation coefficient ($\overline{\sigma_c}$) was calculated for each compartment, as being the mean relative difference between the measured values of the resultant velocity and the bulk velocity (U_0), such as: –

$$\overline{\sigma_c} = \frac{\sum_{k=1}^{11} \left| \frac{U_{C,k} - U_0}{U_0} \right|}{11} \tag{6.1}$$

where the index C was the compartment number from 1 to 8; the number of layers along each centreline profile was 11; k was a layer index; and $U_{C,k}$ was the magnitude of the corresponding mean streamwise velocity. The results obtained for Compartments 1 to 8 are shown in Table 6.2 and Figure 6.4.

Table 6.2 Values of the deviation coefficient calculated in the vertical uniformity analysis of the centreline mean velocity profiles in Compartments 1 to 8 of setup OS-C

k	|U-Uo|/Uo							
	Comp.1	Comp.2	Comp.3	Comp.4	Comp.5	Comp.6	Comp.7	Comp.8
11	7.6	1.1	1.1	0.5	0.7	0.1	0.3	0.1
10	7.2	1.4	1.2	0.0	0.7	0.2	0.0	0.1
9	2.4	1.1	0.8	0.6	0.2	0.2	0.1	0.0
8	0.6	1.0	0.4	1.3	0.2	0.2	0.1	0.2
7	0.6	0.9	0.1	0.9	0.2	0.1	0.4	0.1
6	0.4	0.3	0.1	0.9	0.3	0.2	0.5	0.2
5	0.5	0.3	0.2	0.6	0.3	0.4	0.2	0.2
4	2.0	0.3	0.7	0.1	0.2	0.0	0.1	0.5
3	1.9	0.8	1.2	0.9	0.4	0.2	0.2	0.4
2	3.3	2.2	1.0	0.9	0.2	0.2	0.1	0.1
1	3.9	3.0	1.0	0.9	0.1	0.3	0.2	0.2
Average	2.8	1.1	0.7	0.7	0.3	0.2	0.2	0.2
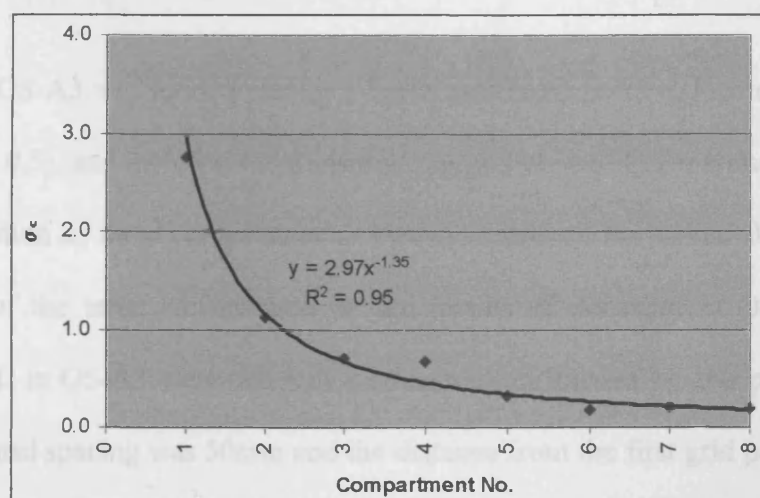
Figure 6.4 Variation of the deviation coefficient values shown in Table 6.2

$$y = 2.97x^{-1.35}$$
$$R^2 = 0.95$$

The bottom row of Table 6.2 shows the values of $\overline{\sigma_c}$ calculated using Equation (6.1) for Compartments 1 to 8. As it can be noticed in these results, a trend of decrease of the value of the deviation coefficient occurred from Compartment 1 to 6. The decay of $\overline{\sigma_c}$ along compartments followed a power trend, as shown in Figure 6.4. This was followed by the parameter becoming asymptotic at 0.2 for Compartments 6, 7 and 8, indicating that the corresponding mean velocity distributions tended to be vertically uniform. This fact suggested that the mean velocity field had a 2-D horizontal character from Compartment 6 until the centreline of Compartment 8 of setup OS-C.

This indication was in disagreement with the observations of Teixeira (1993) for a similar contact tank, where the start of 2-D flow reportedly occurred in Compartment 5 of that tank. Such a discrepancy was probably a consequence of the different relative dimensions between the two prototype units.

6.2.1.3   Assessment OS-A3

Assessment OS-A3 was carried out for a horizontal cross-section, located at mid-depth (i.e. at z/H = 0.5), and included the transition region between Compartments 7 and 8, as well as a portion of these compartments. Two-dimensional horizontal flow occurred in this region of the tank, as indicated by the results of Assessment OS-A2. Velocity measurements in OS-A3 were taken in a cross-section formed by 260 points, in which the internal grid spacing was 50mm and the distance from the first grid point near a wall or baffle to the corresponding boundary was 25mm.

The results for Assessment OS-A3 are shown in Figure 6.5. The horizontal length scales in this Figure were normalised by the compartment width (L), where L = 365mm. The location of walls W3 and W4, as well as Baffles 6 and 7 and Compartments 7 and 8 are indicated in Figure 6.5a, which shows a vector plot of the mean resultant velocity field. The resultant velocities were calculated from the corresponding longitudinal and lateral velocity components (i.e. U and V, respectively), and were then normalised relative to U_0. Iso-velocity contour plots of these velocity components are shown in Figures 6.5b and 6.5c respectively.

In Figure 6.5a it can be seen that a predominantly streamwise flow occurred in Compartment 7 for x/L < 0.0, with a non-uniform velocity distribution across this compartment.

The location of the transition region between Compartments 7 and 8 is indicated in Figure 6.5 as the region of x/L > 0.0. Downstream of the transition region a horizontal recirculation zone occurred in the vicinity of Baffle 7, as shown in Figure 6.5a. This zone was formed as a consequence of flow separation at the baffle lee (Teixeira, 1993). The width and length of the recirculation zone were estimated as approximately 0.5L and 1.6L respectively, where L was the compartment width. Figure 6.5b indicates that the maximum magnitude of the reversing flow velocity in this region was of the order of 80% of U_0, whereas in the main advective flow path along wall W4 the maximum velocity magnitude measured corresponded to 220% of U_0.
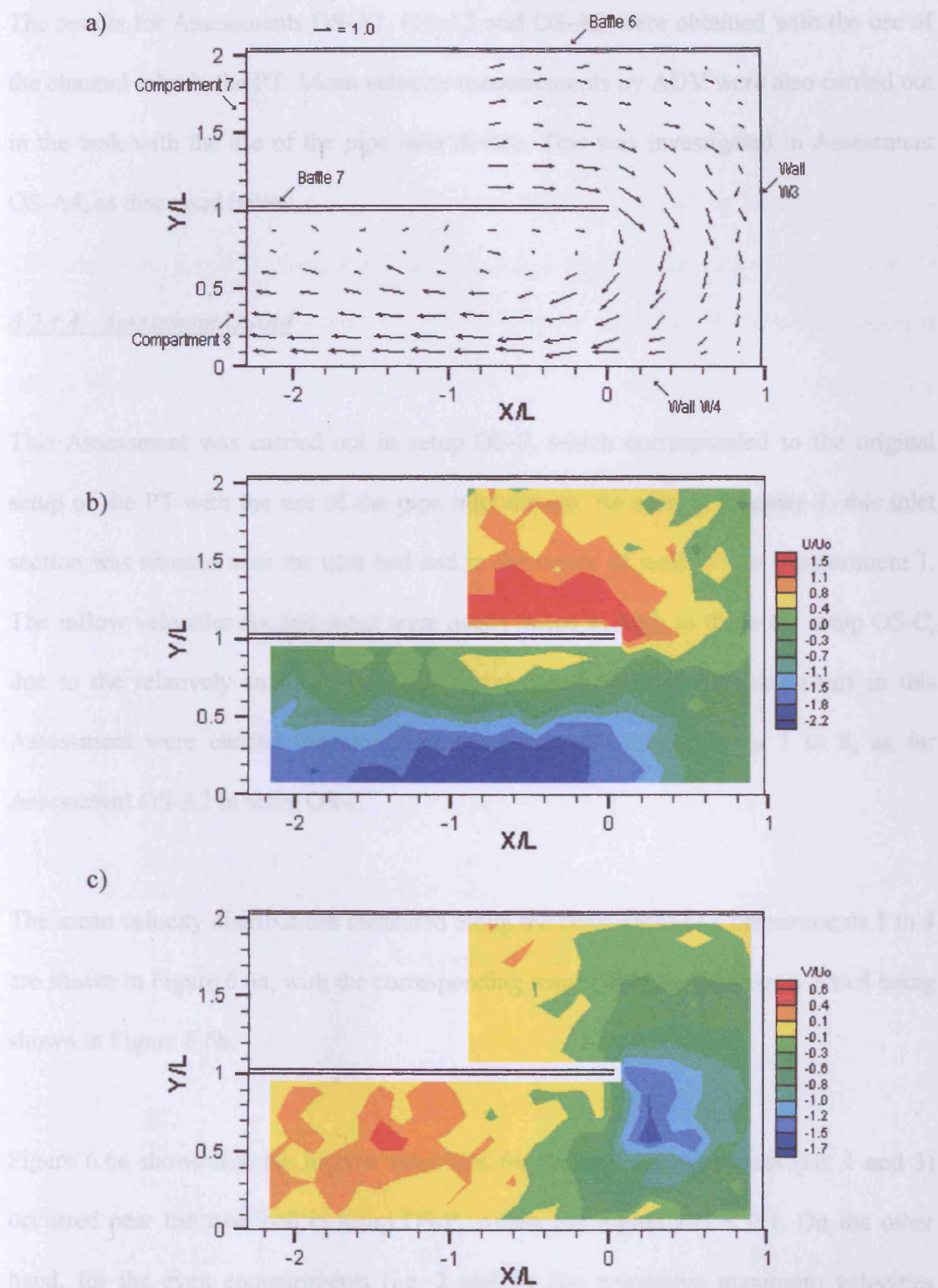
Figure 6.5 Measured results in Assessment OS-A3, illustrating: a) Vector plot of the mean velocity field; b) U/U_0 iso-velocity contours; and c) V/U_0 iso-velocity contours

The results for Assessments OS-A1, OS-A2 and OS-A3 were obtained with the use of the channel inlet in the PT. Mean velocity measurements by ADV were also carried out in the tank with the use of the pipe inlet device. This was investigated in Assessment OS-A4, as discussed below.

6.2.1.4   Assessment OS-A4

This Assessment was carried out in setup OS-P, which corresponded to the original setup of the PT with the use of the pipe inlet device. As seen in Chapter 3, this inlet section was situated near the tank bed and in the centre of wall W1 in compartment 1. The inflow velocities for this setup were nearly twice as high as those for setup OS-C, due to the relatively smaller inlet cross-section area. Velocity measurements in this Assessment were carried out along the centreline of Compartments 1 to 8, as for Assessment OS-A2 in setup OS-C.

The mean velocity distributions measured along the centrelines of Compartments 1 to 4 are shown in Figure 6.6a, with the corresponding results for Compartments 5 to 8 being shown in Figure 6.6b.

Figure 6.6a shows that the highest velocities for the odd compartments (i.e. 1 and 3) occurred near the tank bed in setup OS-P, within the region $z/H < 0.1$. On the other hand, for the even compartments (i.e. 2 and 4), the respective maximum velocities occurred in the upper layers of the centreline, i.e. where $z/H > 0.9$. The corresponding

maximum velocity magnitudes in relation to U_0 were of the order of 1540%, 580%, 290% and 230% in Compartments 1 to 4 respectively.

In Figure 6.6b it can be seen that velocities that occurred along the centrelines of Compartments 5 to 8 in setup OS-P were in the streamwise direction. The maximum velocity measured in Compartment 5 was of the order of 180% of U_0, which occurred within the region $z/H < 0.1$. In the centreline of Compartment 6, this velocity corresponded to 160% of U_0 within the region $z/H > 0.9$. For Compartments 7 and 8 no trend could be detected for the region of occurrence of the maximum streamwise velocity.

a) $\rightarrow = 1.0$

b) $\rightarrow = 1.0$

Figure 6.6 Vertical profiles of mean normalised velocities measured along compartment centrelines of setup OS-P for: a) Compartments 1 to 4; and b) Compartments 5 to 8

6.2.2 Modified Setup No. 4 of Prototype Tank

The results included in this Section were obtained from velocity measurements using the ADV as performed in setups MS4-C and MS4-P. As seen in Chapter 3 and Table 6.1, a transversal baffling arrangement was used in the first 5 compartments of these setups of PT, which were formed by 6 compartments and where the channel and pipe inlet devices were respectively used.

Assessments of mean velocity profiles in setups MS4-C and MS4-P were undertaken along vertical lines in Compartments 1 to 6, in a similar manner to Assessment OS-A2. A total of eight vertical profiles were measured in each setup, where two profiles were taken in Compartment 1, two in Compartment 2 and one in each remaining compartment. These profiles were situated at mid-width of the corresponding compartment. The spacing between the measurement points within the profiles was 100mm, where the first grid point was situated 30mm away from the tank bed.

The results for setups MS4-C and MS4-P are respectively shown in Figures 6.7 and 6.8. Figures 6.7a and 6.8a show the vertical profiles measured in Compartments 1 and 2, where sections A and B refer to the start and end region of the corresponding compartment. The mean velocity profiles measured in Compartments 3 to 6 are given in Figures 6.7b and 6.8b.

Figures 6.7a and 6.8a indicate that the mean velocity field in Compartment 1 of setups MS4-C and MS4-P had a strongly three-dimensional character. The maximum

magnitudes of the vertical velocity component (W), verified in profiles 1A of these setups, corresponded to 90% and 130% of U_0 respectively. In profiles 1B the corresponding maximum magnitude verified for W was of the order of 40% and 50% of U_0. The maximum magnitude verified for W in profiles 2A of these setups was of the order of 50% of U_0. This parameter corresponded to 10% of U_0 in profile 2B for either setup.

Figures 6.7b and 6.8b indicate that a predominantly 2-D mean flow occurred from Compartment 3 onwards in setups MS4-C and MS4-P, where recorded W values were lower than 10% of U_0.

With regard to the mean streamwise velocity component, the maximum magnitude verified for this parameter in both setups corresponded to 250% of U_0, which occurred in the respective Compartment 1. For setup MS4-C and profile 2A, this parameter corresponded to 150% of U_0, while for profile 2B this parameter was of the order of 130% of U_0. These velocities occurred at z/H = 0.72 in both profiles of Compartment 2. From Compartment 3 to Compartment 6 the maximum streamwise velocity was of the order of 130% of U_0, except for the point situated at z/H = 0.03 in Compartment 6, where the magnitude of this parameter was 150% of U_0. For setup MS4-P, the maximum velocity magnitude verified in Compartments 2 to 6 corresponded to 130% of U_0, except for the point situated at z/H = 0.92 in Compartment 3, where the magnitude of the streamwise velocity was 150% of U_0.
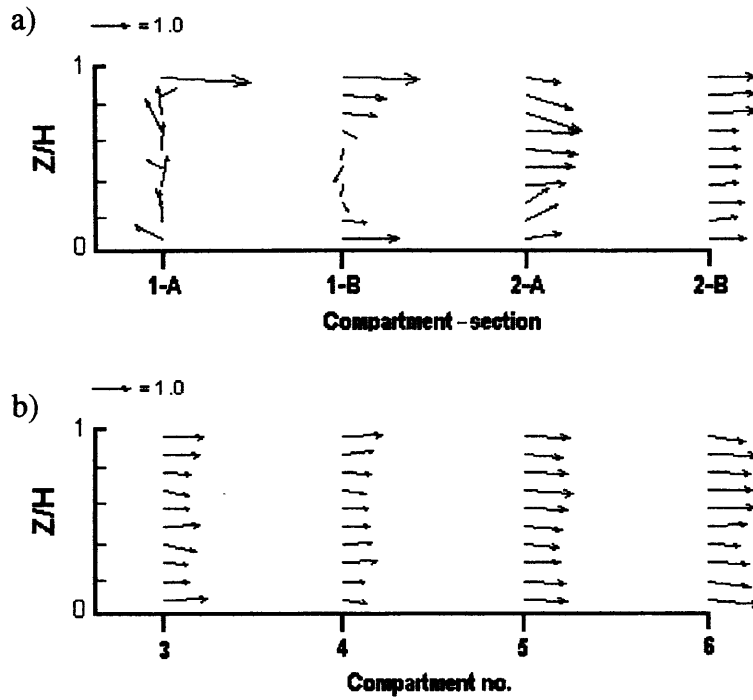
Figure 6.7 Vertical profiles of mean normalised velocities measured along compartment centrelines of setup MS4-C for: a) Compartments 1 and 2; and b) Compartments 3 to 6
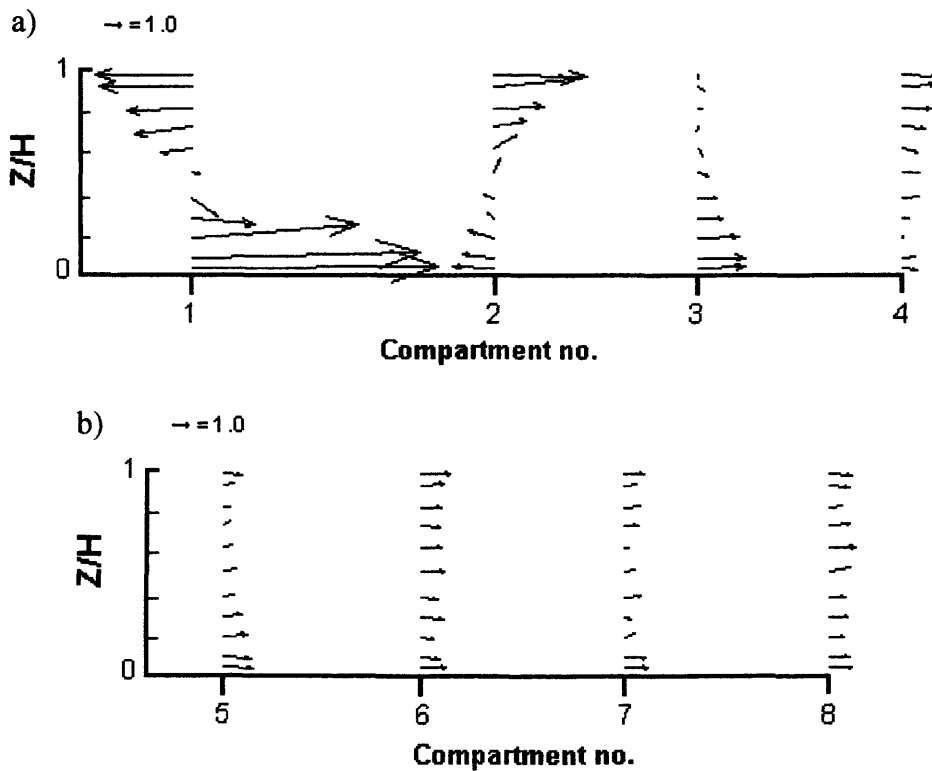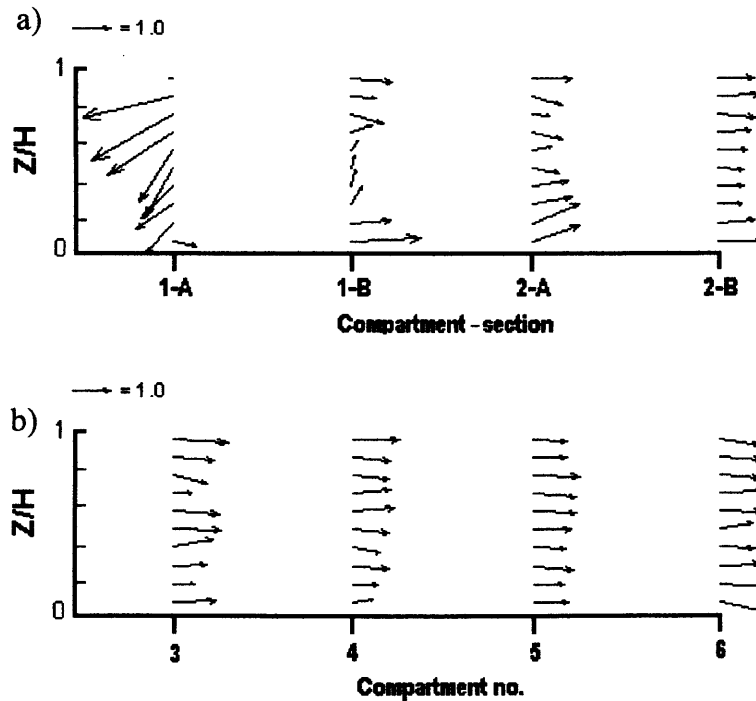

Figure 6.8 Vertical profiles of mean normalised velocities measured along compartment centrelines of setup MS4-P for: a) Compartments 1 and 2; and b) Compartments 3 to 6

6.2.3 Modified Setup No. 3 of Prototype Tank

The results presented herein were obtained from the ADV velocity measurements carried out in setup MS3 of PT. This design setup corresponded to the unbaffled configuration of the tank, where use was made of the pipe inlet device. The grid spacing between the measurement points was 100mm, while the distance from the first grid point to the nearest solid boundary was 50mm. These ADV measurements were undertaken for a period of 15min at each point.

Data acquisition were carried out at three cross-sections of the flow in setup MS3, which were located as follows:

- Cross-section 1: the vertical (X-Z) plane situated along the vertical centreline of the inlet section (i.e. for Y = 2820mm);

- Cross-section 2: the horizontal (X-Y) plane situated near the tank bed (i.e. for Z = 30mm);

- Cross-section 3: the vertical (X-Z) plane situated along the horizontal mid-width line of the tank (i.e. for Y = 1500mm).

The results of the normalised mean velocities, measured at the cross-sections defined above, are shown in Figures 6.9, 6.10 and 6.11 respectively. The horizontal and vertical length scales in these Figures were normalised by including the water depth (H) in the tank, while velocities were normalised by including the bulk velocity (U_0).

120
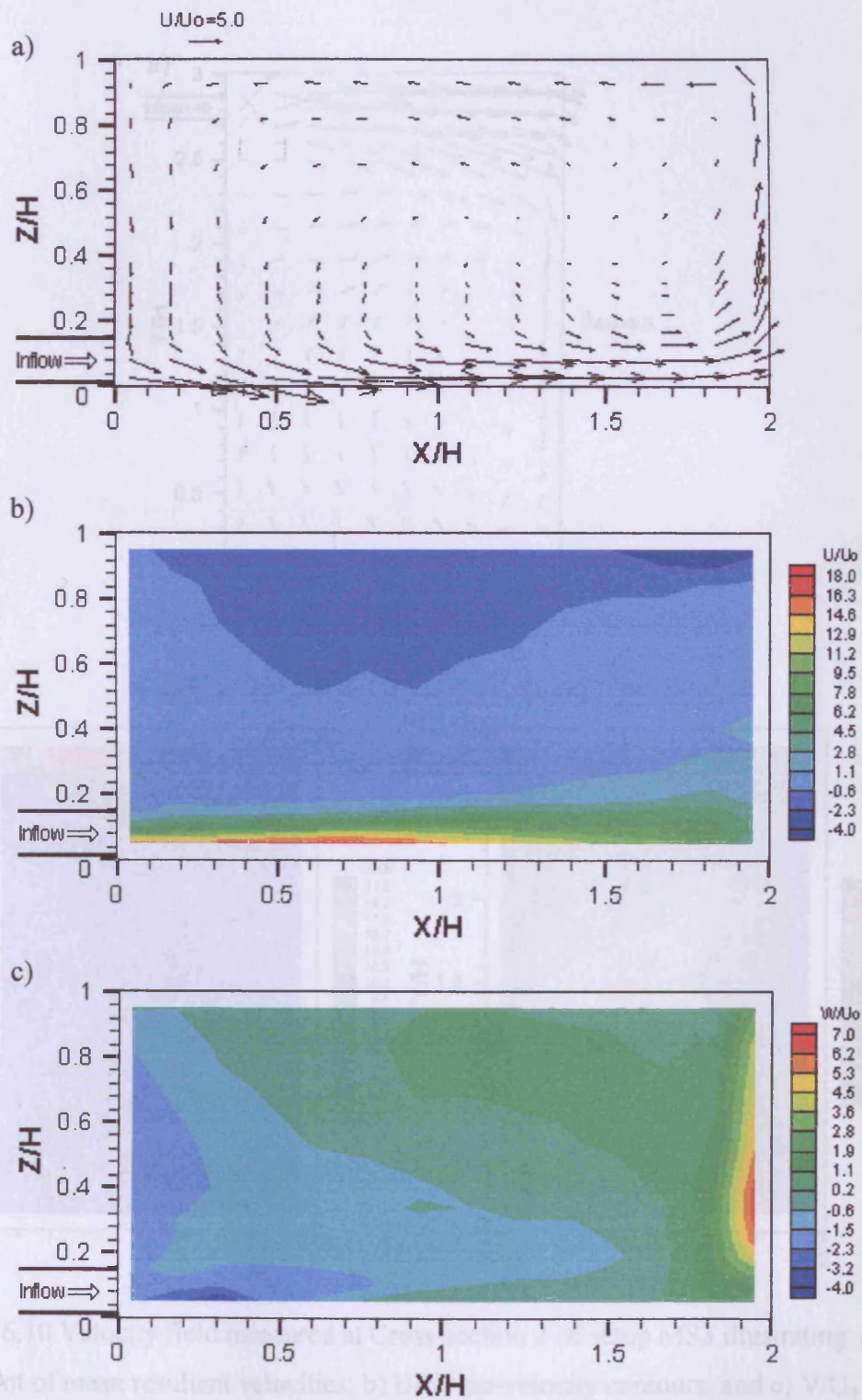
Figure 6.9 Velocity field measured at Cross-section 1 of setup MS3 illustrating: a)
Vector plot of mean resultant velocities; b) U/U_0 iso-velocity contours; and c) W/U_0 iso-
velocity contours
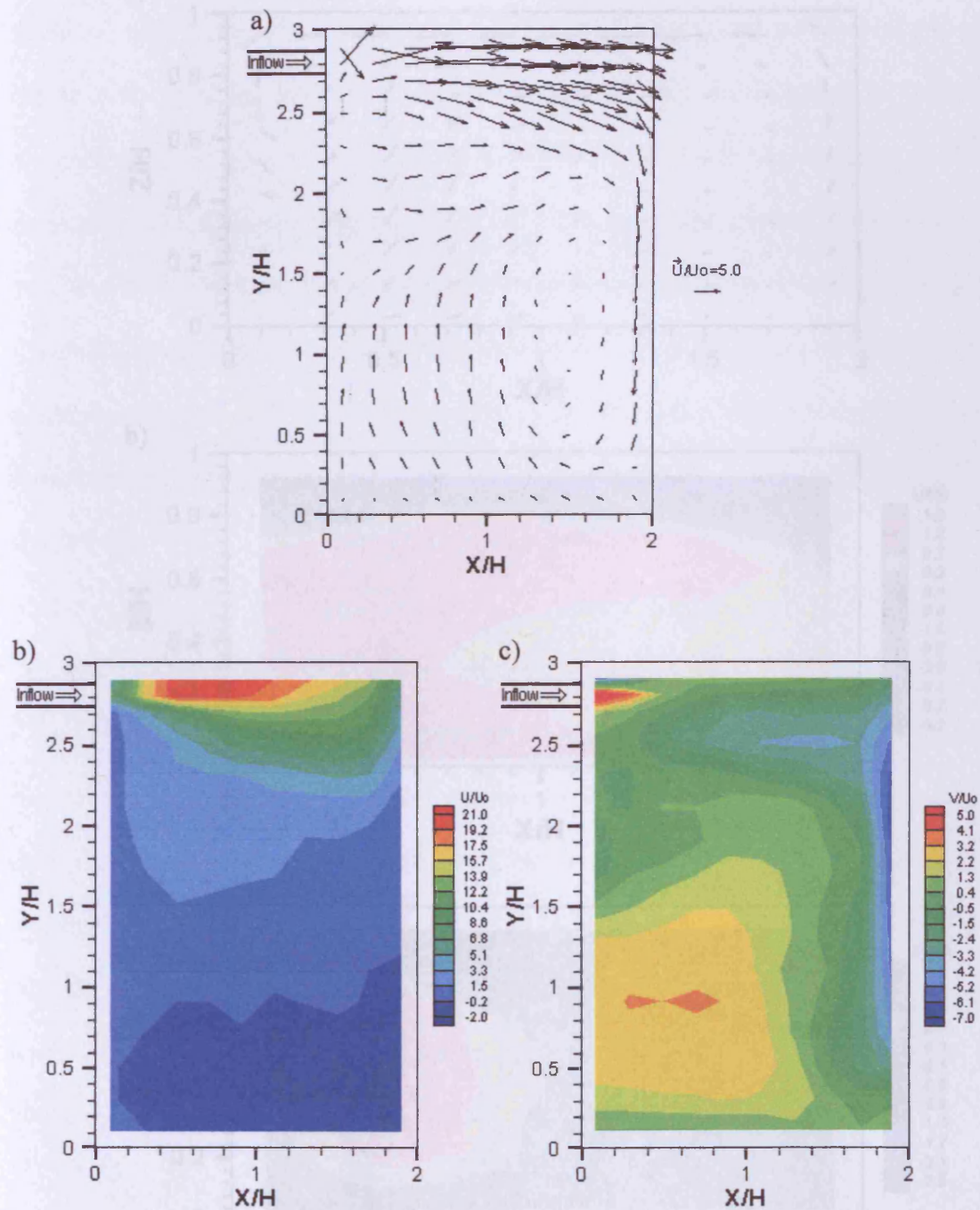
Figure 6.10 Velocity field measured at Cross-section 2 of setup MS3 illustrating: a) Vector plot of mean resultant velocities; b) U/U_0 iso-velocity contours; and c) V/U_0 iso-velocity contours
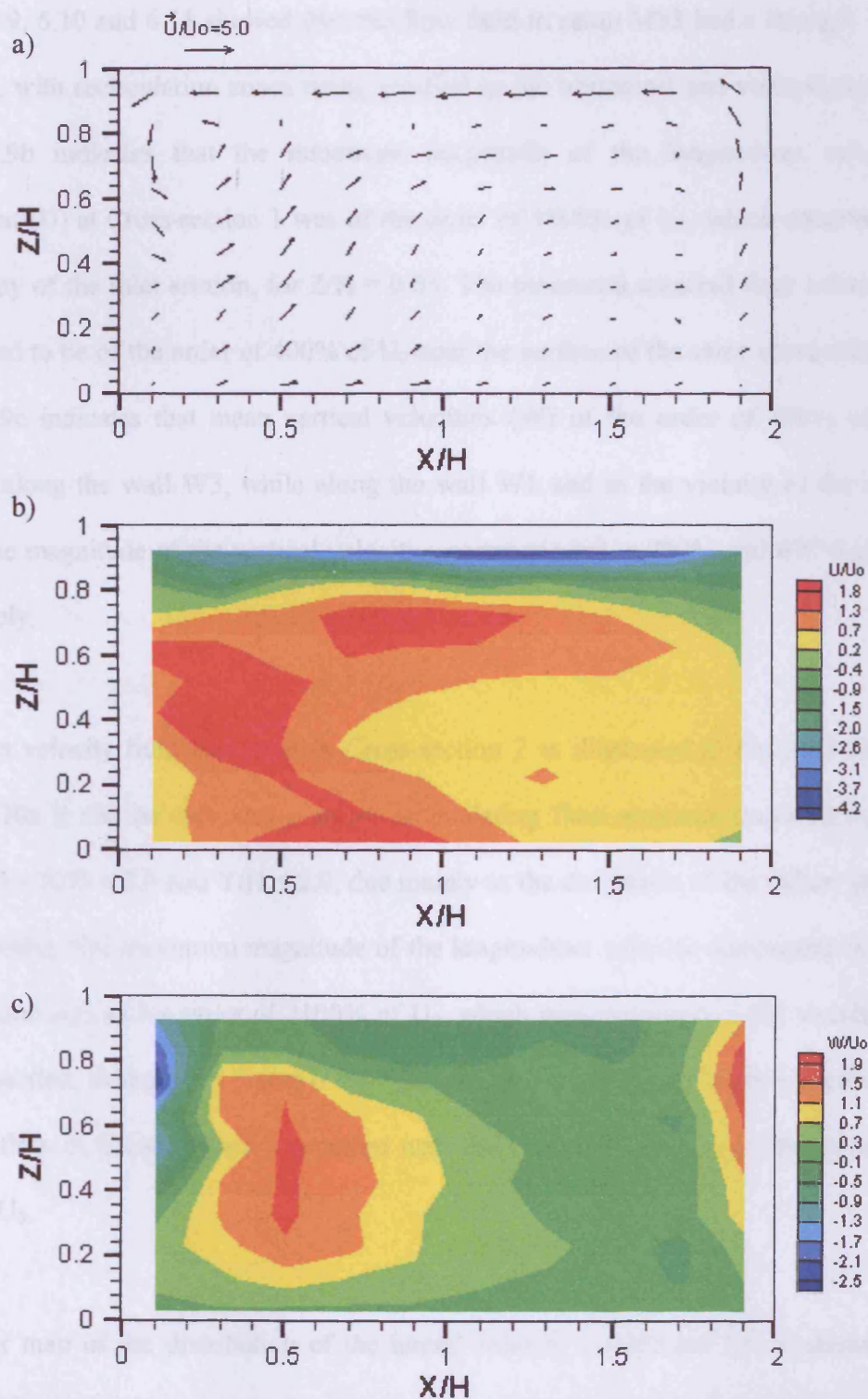
Figure 6.11 Velocity field measured at Cross-section 3 of setup MS3 illustrating: a) Vector plot of mean resultant velocities; b) U/U$_0$ iso-velocity contours; and c) W/U$_0$ iso-velocity contours

Figures 6.9, 6.10 and 6.11 showed that the flow field in setup MS3 had a strongly 3-D character, with recirculation zones being verified in the horizontal and vertical planes. Figure 6.9b indicates that the maximum magnitude of the longitudinal velocity component (U) at Cross-section 1 was of the order of 1800% of U_0, which occurred in the vicinity of the inlet section, for $Z/H = 0.05$. The measured reversed flow velocities were found to be of the order of 400% of U_0 near the surface of the same cross-section. Figure 6.9c indicates that mean vertical velocities (W) of the order of 700% of U_0 occurred along the wall W3, while along the wall W1 and in the vicinity of the inlet section the magnitude of the vertical velocities corresponded to 200% and 400% of U_0 respectively.

The mean velocity field measured in Cross-section 2 is illustrated in Figure 6.10. In Figure 6.10a it can be seen that a major recirculating flow structure occurred in the region $1.0 < X/H < 2.0$ and $Y/H < 2.0$, due mainly to the deflection of the inflow jet by the tank walls. The maximum magnitude of the longitudinal velocity component in this cross-section was of the order of 2100% of U_0, which was measured in the vicinity of the inlet section, as shown in Figure 6.10b. The maximum magnitude of the horizontally reversed flow in Cross-section 2 occurred near the wall W4 and was of the order of 200% of U_0.

A contour map of the distribution of the lateral velocity component (V) is shown in Figure 6.10c. In this Figure it can be seen that the maximum magnitude of this velocity component occurred near the wall W3 and was of the order of 700% of U_0. Such relatively high lateral velocities occurred in this region as a consequence of the

deflection of the inflow jet by the above mentioned wall. Lateral velocities of the order of 320% of U_0 occurred in the region X/H < 1.0 and Y/H = 1.0, and of the order of 500% of U_0 in the vicinity of the inlet section to the tank.

The results for Cross-section 3 are shown in Figure 6.11. In Figure 6.11a it can be seen that a vertical recirculation zone was found to occur in the region X/H < 0.5 and Z/H >0.6. The highest velocity values measured around this zone were of the order of 310% of U_0 for U and of 250% of U_0 for W, as indicated in Figures 6.11b and 6.11c respectively. The measured flow field along the surface layer of this cross-section (i.e. for Z/H = 0.93) presented the maximum magnitude of 420% of U_0 for U. Near the wall W3 the maximum vertical velocity measured was of the order of 190% of U_0.

Due to the flow field in setup MS3 being occupied mainly by recirculating flow structures, it was expected that considerably high levels of mixing would occur in this setup. This was analysed in the following section, where the results obtained using tracer techniques for various configurations of the PT are discussed.

6.3. CHARACTERISATION OF SHORT-CIRCUITING AND MIXING LEVELS

The design setups of PT that were assessed for their solute transport characteristics were setups OS-C, OS-P, MS1, MS2, MS3, MS4-C and MS4-P, as defined in Table 6.1 and described in Chapter 3. The main outcomes of the tracer tests performed in this work were Residence Time Distribution (RTD) curves, accumulated tracer mass (F) curves and Hydraulic Efficiency Indicators (HEI) of the flow. These results were analysed

through qualitative and semi-quantitative methods to characterise the levels of short-circuiting and mixing associated to the design configurations cited above.

The value of the experimentation flow rate (Q) was Q = 3.7l/s, for which the theoretical hydraulic residence time (T) in PT was 27min. The value of T was calculated as T = V_{PT}/Q, where V_{PT} was the average wetted volume amongst the design setups of PT. Data acquisition during the tracer tests were undertaken for periods that varied between 2.5T and 4.0T, depending on the mixing levels of the respective tank setup. The time interval between two consecutive tracer concentration readings was 3s. The procedures adopted in normalising the tracer data, as well as in obtaining mean RTD curves, F curves and HEI parameters were explained in Chapter 3.

6.3.1 Mean RTD and F curves

Mean RTD and F curves for the various design setups of PT are shown in Figure 6.12. In Figures 6.12a and 6.12b the respective vertical axis represents the normalised concentration of tracer (E) and the accumulated tracer mass (F), while the horizontal axis gives the normalised time (t/T). The RTD and F curves corresponding to Complete Mixing (CM) and Plug Flow with Dispersion (PFwD) flow patterns are also shown in Figure 6.12. These curves were calculated by using analytical expressions given in Chapter 3. In the following analyses the PFwD results represented the condition for the theoretical maximum Hydraulic Efficiency of PT, taking into consideration that the ideal flow pattern for the disinfection process in chlorine contact tanks is Plug Flow.
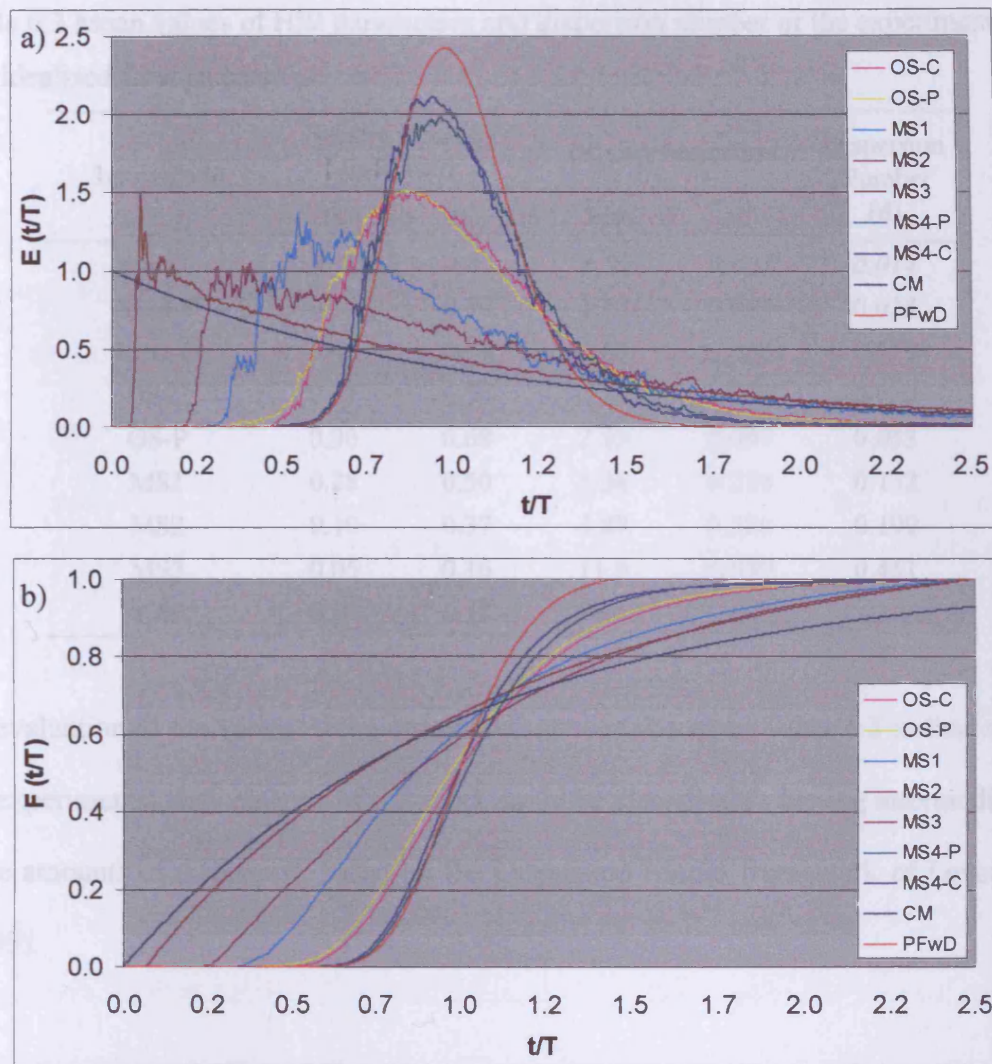
Figure 6.12 Experimental tracer curves and representation of the idealised flow patterns Complete Mixing and Plug Flow with Dispersion for: a) RTD curves; and b) F curves

6.3.2 Hydraulic Efficiency Indicators

The results for the short-circuiting indicators θ_i and θ_{10} and mixing indicators Mo and σ^2, corresponding to the mean tracer curves, are shown in Table 6.3, as well as the value of the dispersion number (d) for each setup. The limits for the range of variation of the HEI parameters and d were represented by the corresponding PFwD and CM results. The short-circuiting and mixing parameters used were defined in Table 3.3.

Table 6.3 Mean values of HEI parameters and dispersion number of the experimental and idealised flow patterns

Setup Code	Short-Circuiting Indicators		Mixing Indicators		Dispersion Number (d)
	θ_i	θ_{10}	Mo	σ^2	
PFwD	*0.50*	*0.81*	*1.52*	*0.027*	*0.014*
MS4-P	0.50	0.79	1.71	0.052	0.028
MS4-C	0.48	0.78	1.69	0.055	0.029
OS-C	0.47	0.70	2.12	0.095	0.050
OS-P	0.30	0.68	2.13	0.097	0.053
MS1	0.28	0.50	3.38	0.224	0.132
MS2	0.19	0.37	4.89	0.306	0.190
MS3	0.05	0.16	11.5	0.539	0.451
CM	*0.00*	*0.11*	*22.8*	*1.00*	$\rightarrow \infty$

An evaluation of the values of the dispersion number shown in Table 6.3 indicated that the experimental flow patterns of this work could be classified as having intermediate to large amounts of dispersion, based on the Dispersion Model framework of Levenspiel (1999).

Some deviation coefficients were calculated for the experimental data, in relation to the corresponding PFwD results. These parameters were: i) the Percentile Area Deviation (PAD) coefficient between RTD curves, and ii) the deviation coefficients between values of the HEI parameters ($D_{\theta i}$, $D_{\theta 10}$, D_{Mo} and D_σ^2) and between values of d (D_d). The PAD coefficient has been defined as a measure of non-coincidence between the areas of a pair of RTD curves (Rauen, 2001). Calculated PAD values can vary between 0% and 100%, which indicate total coincidence and no coincidence of the curve areas respectively. The D_{HEI} coefficients represented the relative deviation of a HEI value in

comparison to the corresponding PFwD value. The results obtained for the deviation coefficients are shown in Table 6.4.

Table 6.4 Deviation coefficients for RTD curves and HEI parameters in relation to the corresponding PFwD results

Setup Code		θ_i	θ_{10}	Mo	σ^2	d
PFwD	---	*0.50*	*0.81*	*1.52*	*0.027*	*0.014*
	PAD	$D_{\theta i}$	$D_{\theta 10}$	D_{Mo}	D_σ^2	D_d
MS4-P	11%	0.4%	1.5%	13%	89%	108%
MS4-C	10%	4.2%	2.9%	11%	100%	101%
OS-C	27%	5.0%	13%	39%	246%	259%
OS-P	28%	39%	15%	40%	253%	280%
MS1	51%	43%	38%	122%	715%	847%
MS2	58%	62%	54%	222%	1013%	1263%
MS3	67%	90%	80%	653%	1860%	3135%
CM	*70%*	*100%*	*86%*	*1400%*	*3537%*	$\to \infty$

In analysing the results in Table 6.4 for the experimental setups considered, it can be seen that the highest value of the deviation coefficients involved in this assessment were associated with setup MS3, which suggests that the flow pattern of this setup presented the most significant deviation from PFwD condition, among the experimental results. This analysis indicated that setup MS3 had the worst level of hydraulic efficiency verified experimentally in this work. In connection with the corresponding hydrodynamic results shown in section 6.2.3, it can be inferred that the relatively high levels of short-circuiting and mixing measured for this setup were due to the recirculating flow regions occupying almost the entirety of the tank. The RTD and F curves, as well as the values of HEI parameters obtained for setup MS3, were more closely associated with the corresponding results for the CM flow pattern, as shown in Figure 6.12 and Tables 6.3 and 6.4.

The lowest values of the deviation coefficients were associated either with setup MS4-P or MS4-C, as shown in Table 6.4. The latter presented the lowest PAD value, indicating that the respective RTD curve was the closest match to the corresponding PFwD curve. This fact suggested that setup MS4-C presented the highest level of hydraulic efficiency amongst the experimental setups of PT. However, the levels of short-circuiting were higher in this setup than in setup MS4-P, as indicated by the relatively higher values of $D_{\theta i}$ and $D_{\theta 10}$.

With regard to the mixing levels, Table 6.4 shows that setup MS4-P gave rise to the lowest value of D_{σ}^2 but, on the other hand, the lowest value of D_{Mo} was associated with setup MS4-C. However, Teixeira and Siqueira (2005) recommended that preference should be given to the use of the Morrill index (Mo) in situations where the mixing levels were low (i.e. where $\sigma^2 < 0.27$), since high statistical variability of σ^2 can be expected in such cases. The experimental results for σ^2 appear in Table 6.3, where it can be seen that setups MS4-C and MS4-P, among others, presented a low mixing level (based on Teixeira and Siqueira's classification). A comparison based on the values of D_{Mo} suggested that the lowest mixing levels occurred for setup MS4-C. This fact was consistent with the indication provided by the PAD parameter, which took into consideration the whole area of the RTD curve.

In comparing the values shown in Table 6.4 for the deviation coefficients for setups OS-P and OS-C, it can be seen that the results for the former configuration were consistently higher than for the latter setup, indicating that the use of the pipe inlet had a prejudicial effect on the hydraulic efficiency of the tank. This effect could be linked to

an increased influence of the inflow jet on the flow pattern for setup OS-P in relation to setup OS-C, as shown in section 6.2. However, it can be inferred that such an effect was not very significant, since the observed discrepancies for all but one of the deviation coefficients involved in this analysis were of the same order of magnitude between the two setups. The exception for this was the coefficient $D_{\theta i}$, which showed a substantial increase due to the change of inlet device in setup OS-P (from 5% to 39%, as shown in Table 6.3), thus suggesting that the use of the pipe inlet in the original setup of PT caused an earlier start of the tracer passage through the outlet section. However, the relatively low difference in the values of the coefficient $D_{\theta 10}$ (13% and 15%, for setups OS-C and OS-P respectively) indicated that the amount of tracer that followed short-circuiting routes through the tank did not increase substantially.

An evaluation of influences exerted by the type of baffling arrangement on the short-circuiting and mixing characteristics of the flow in PT involved comparing the results for setups MS4 and OS, regardless of the type of inlet device. It can be seen in Table 6.3 that the values of the deviation coefficients obtained for setup MS4 were significantly lower than the corresponding values for setup OS. This fact indicated that the use of transversal baffling generated lower levels of short-circuiting and mixing in the tank and, thus, a better hydraulic efficiency. This effect was mainly regarded as a consequence of the reduction in the volume occupied by the vertically reversed flow zones in setup MS4, as suggested from the results for the mean velocity measurements shown in Section 6.3.

Summary

The design configurations of the Prototype Tank (PT) described in Chapter 3 have been assessed by ADV measurements and tracer techniques, and the results obtained were discussed in this Chapter. The main features of the three-dimensional (3-D) mean velocity field measured in the original setup of PT were characterised, which included recirculating flows in the vertical and in the horizontal planes. The effects of the type of inlet device and baffling arrangement on the three-dimensionality of the mean flow through the tank were evaluated. Further ADV results were analysed for the unbaffled setup of PT, which showed that a strongly three-dimensional flow field occurred throughout the tank in this setup. Following these results, the Retention Time Distribution (RTD) curves and Hydraulic Efficiency Indicators (HEI) obtained from tracer experiments were discussed. An analysis of these results indicated that a relatively wide range of flow patterns, expressed in terms of the mixing levels, was assessed in this study. Comparisons were made with the RTD and HEI results corresponding to the idealised flow pattern for PT, i.e. the plug flow with dispersion. The analyses suggested that the highest level of hydraulic efficiency for the tank, among the configurations assessed in this study, was found in the setup with a cross-baffling arrangement, which presented the lowest levels of short circuiting and mixing. Such a behaviour was regarded as a consequence of the reduction of the region occupied by three-dimensional flow in the tank, relatively to the other assessed setups and as shown in the results of the ADV assessments. The hydrodynamic and solute transport results included in this Chapter were used in the validation analysis of the corresponding numerical model predictions, as discussed in Chapter 8.

Chapter 7

Benchmark Validation

of Numerical Model Results

7.1. INTRODUCTION

Results are given herein that were obtained in the validation analysis of the numerical model described in Chapter 5, and which included comparisons with analytical solutions and experimental evidence for a number of benchmark open channel flow problems. The main aim of the analyses included herein was to validate the hydrodynamic module of the numerical model, which included the corresponding discretised equations, boundary conditions, solution method and other aspects of the numerical scheme. The analyses were carried out for the laminar, transient and turbulent flow regimes. In section 7.2 a validation analysis is carried out for the developing and fully-developed laminar flow problem. Then, in section 7.3 the analysis is extended to turbulent channel flows with varying levels of turbulence.

7.2. HAGEN-POISEUILLE FLOW

The results included in this section were obtained with the numerical model being used under the laminar flow mode, i.e. without the use of a turbulence model, so that the eddy viscosity (v_t) was set to zero.

7.2.1 Problem description

A two-dimensional (2-D) horizontal laminar flow scenario was simulated using the numerical model for an open channel with two parallel flat stationary walls. This type of flow is known as the Hagen-Poiseuille (H-P) flow, for which a schematic representation is shown in Figure 7.1.
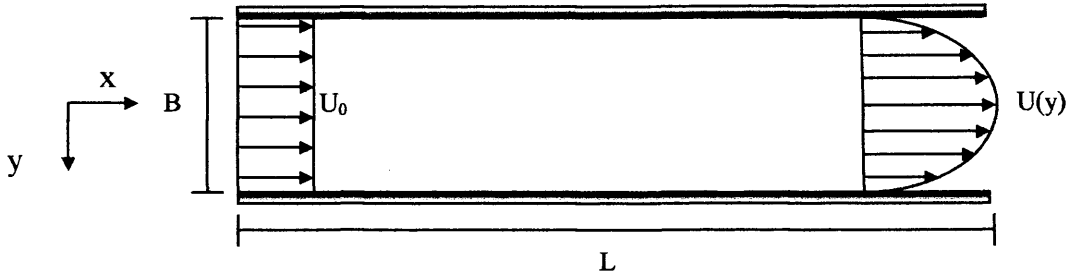
Figure 7.1 Schematic representation of the Hagen-Poiseuille channel flow problem

The fully-developed velocity distribution, i.e. U(y), of the H-P flow is parabolic in shape and the corresponding exact solution can be expressed as (Schlichting, 1979): –

$$U(y) = U_m \left(1 - \frac{4y^2}{B^2} \right)$$ (7.1)

where U(y) is the velocity at a distance y from the channel centreline, U_m is the maximum velocity of the profile and B is the channel width.

The length required for the establishment of fully-developed H-P flow, where a uniform velocity distribution (i.e. U(y) = U_0) is given at the channel inlet, is known as the entrance length (EL). This parameter can be calculated as a function of B and the Reynolds number, such as: –

$$EL = 0.06 \, \text{Re} \, B$$ (7.2)

where Re is the bulk Reynolds number of the flow.

7.2.2 Simulation conditions

The value of the Reynolds number for the H-P flow simulations in this study was Re = 150, which was calculated as: –

$$Re = \frac{U_0 B}{\nu_l} \qquad\qquad (7.3)$$

where the kinematic viscosity of water was $\nu = 1.004\text{mm}^2/\text{s}$, the channel width B = 100mm and the bulk velocity $U_0 = 1.506\text{mm/s}$. Under such conditions, the value of EL, calculated using Equation (7.2), was EL = 9B. The length of the channel designed for the numerical simulations was L = 20B, which corresponded to more than twice the EL value in order to provide the conditions for the establishment of fully-developed flow, while avoiding any potential influences from the outflow boundary.

The numerical simulations were performed for a "cold start" condition, where the values of all variables were set to zero in the interior of the solution domain. At the inlet section (i.e. for x = 0), use was made of the Dirichlet boundary condition to establish a uniform velocity distribution, so that $U(0,y) = U_0$, while the value of the lateral velocity component and all other variables were initially set to zero. The lateral walls were simulated as no-slip boundaries and the Neumann boundary condition was imposed at the outlet section (i.e. for x = L) for all variables. The computational mesh configurations used to simulate the H-P flow problem involved five mesh spacing values in the cross-width (y) channel direction and one in the streamwise (x) direction. The mesh specifications for the H-P flow problem are listed in Table 7.1.

Table 7.1 Mesh specifications and calculated numerical errors of the fully-developed velocity distributions for the Hagen-Poiseuille channel flow problem

Simulation code	Δx	Δy	N_x	N_y	Mean RDE	Mean RDE-bulk
HP1	0.2B	0.25B	100	4	4.1%	4.7%
HP2	0.2B	0.2B	100	5	3.6%	3.5%
HP3	0.2B	0.1B	100	10	1.6%	1.0%
HP4	0.2B	0.05B	100	20	1.0%	0.4%
HP5	0.2B	0.025B	100	40	0.7%	0.4%

In Table 7.1 it can be seen that the coarsest grid defined for the y direction had four cells (i.e. N_y = 4), which corresponded to a cross-width mesh size (Δy) of 0.25B. Further simulations were carried out for N_y = 5, 10, 20 and 40, where the grid spacing was halved, so that the mesh spacings were Δy = 0.2B, 0.1B, 0.05B and 0.025B respectively. In the streamwise direction, the grid spacing adopted was Δx = 0.2B and, thus, the number of grid points used in the x direction was N_x = 100.

7.2.3 Fully-developed flow velocity distribution

The numerical and analytical results obtained for the fully-developed velocity distribution of the H-P channel flow problem are shown in Figure 7.2. The analytical velocity profile was calculated using Equation (7.1), where the maximum velocity of U_m/U_0 = 1.49 was applied. The fully-developed state of the velocity profile was attested by an analysis of the developing flow velocity profiles, as discussed in section 7.2.4. The numerical results corresponding to the fully-developed velocity profile were taken at the channel length corresponding to x = 15B.
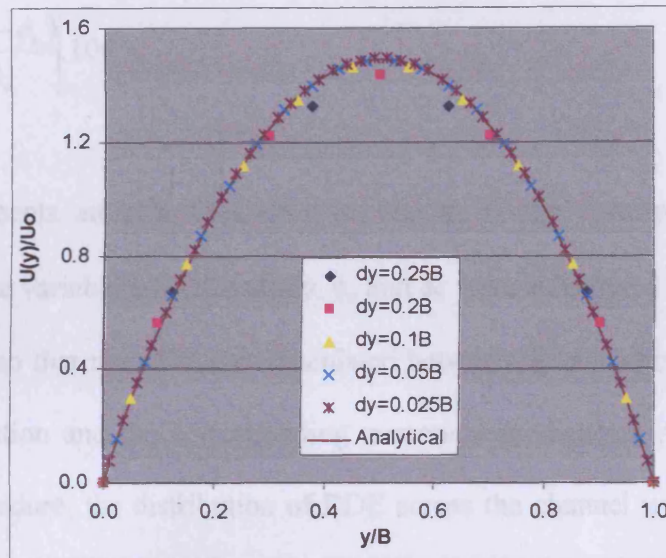
Figure 7.2 Fully-developed velocity distributions and the corresponding analytical
solution for the Hagen-Poiseuille channel flow problem

It can be seen in Figure 7.2 that the analytical solution for the fully-developed H-P
velocity profile was generally well represented by the corresponding numerical results,
except, perhaps, for the results for $\Delta y = 0.25B$ and $0.2B$. An error analysis was carried
out for the results of the fully-developed velocity distributions, as discussed below.

A mesh independence study was carried out for the results of Figure 7.2, involving the
Relative Discretisation Error (RDE) parameter proposed by Roache (1998). This
parameter has also been referred to as the Relative Grid Refinement Error and it has
been used as an error estimate of numerical results (Celik and Zhang, 1995). The
calculation of RDE was based on the generalised Richardson Extrapolation Method, and
was performed according to: –

$$RDE(\%) = \left| \frac{(\phi_a - \phi_n)}{\phi_a} \right|.100 \qquad\qquad (7.4)$$

where ϕ_a represents an analytical solution and ϕ_n is the corresponding numerical prediction for the variable ϕ. In this study, ϕ_a and ϕ_n were substituted by the appropriate values of U(y), so that the RDE was calculated between the analytical fully-developed velocity distribution and the corresponding numerical predictions. As a result of this calculation procedure, the distribution of RDE across the channel width was obtained, as shown in Figure 7.3a.
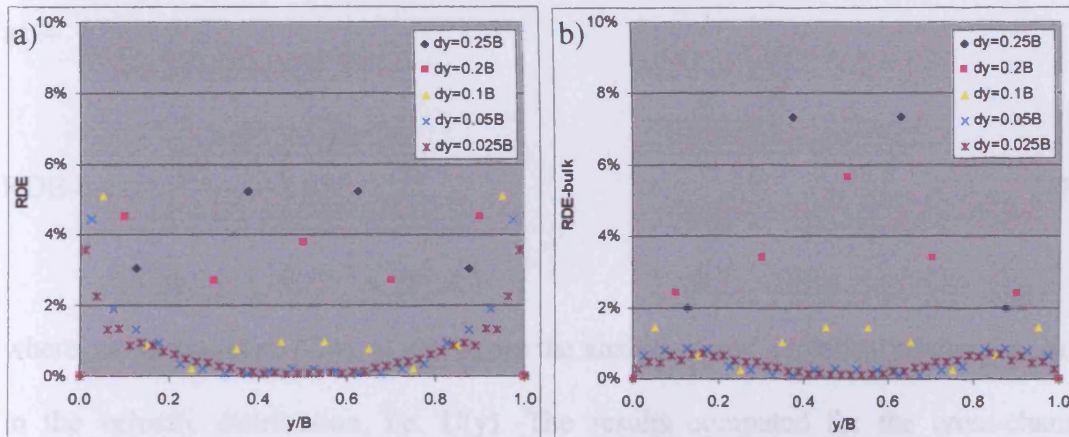
Figure 7.3 Cross-channel distribution of the Relative Discretisation Error parameters for the Hagen-Poiseuille channel flow problem, illustrating: a) distribution of RDE; and b) distribution of RDE-bulk

It can be noticed in Figure 7.3a that the RDE values associated with the three finest mesh sizes, i.e. $\Delta y = 0.025B$, $0.05B$ and $0.1B$, were generally lower than the corresponding results for the coarser meshes, i.e. $\Delta y = 0.2B$ and $0.25B$. Also evidenced in Figure 7.3a is the fact that the error distributions for the former group of mesh sizes showed a clear trend of growth towards the walls (i.e. towards y/B = 0.0 and y/B = 1.0),

in comparison with the respective RDE values for the central region of the channel. This effect was regarded as a consequence of the relative nature of the error parameter used, and the comparatively lower velocities occurring near the channel walls (see Figure 7.2).

In order to avoid inconsistencies in the evaluation of the error distributions, another error parameter was included in this analysis, namely, the RDE-bulk parameter. The formulation of this error estimate differed from the original RDE parameter, in that the differences between the analytical and numerical solutions were divided by a constant parameter, i.e. the bulk velocity (U_0). Therefore, the RDE-bulk values were calculated as: –

$$\text{RDE-bulk} = \left| \frac{(\phi_a - \phi_n)}{U_0} \right| . 100 \qquad (7.5)$$

where, as for Equation (7.4), ϕ_a and ϕ_n are the analytical and numerical results for points in the velocity distribution, i.e. $U(y)$. The results computed for the cross-channel distribution of the RDE-bulk parameter are shown in Figure 7.3b.

It can be seen in Figure 7.3b that the RDE-bulk results for $\Delta y = 0.1B$, $0.05B$ and $0.025B$ did not show a trend of increased near-wall values, as observed for the corresponding RDE results. This observation confirmed the hypothesis made previously concerning the RDE distribution (see discussion on Figure 7.3a) and, thus, both error parameters were used in the remainder of the error analysis.

The results shown in Figures 7.3a and 7.3b were used to calculate the mean RDE value and the mean RDE-bulk value associated with each grid size. The results thus obtained appear in Table 7.1 and, in Figure 7.4, the mean errors were plotted as a function of the non-dimensional grid spacing, i.e. $\Delta y/B$. It can be noted from these results that the values of both mean error parameters decreased monotonically with mesh refinement in the y direction, i.e. with the reduction of the value of dy. This type of behaviour for the computational errors has been related to the occurrence of a monotonic grid convergence pattern for the numerical solutions (Stern et al., 2001).
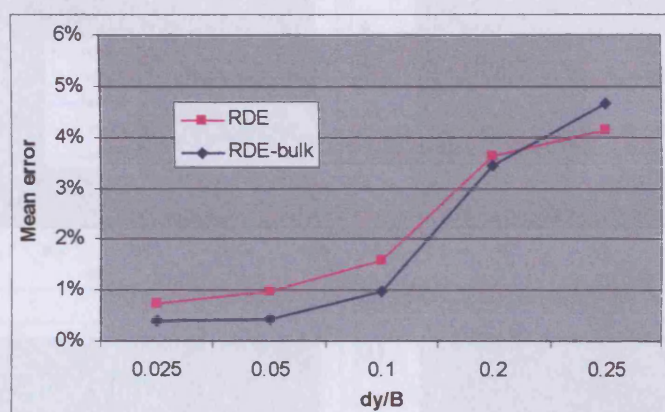
Figure 7.4 Variation of the mean RDE and RDE-bulk values as a function of the grid spacing for the Hagen-Poiseuille channel flow problem

Furthermore, a qualitative analysis of Figure 7.4 suggested that the error values for $\Delta y = 0.05B$ might have been within the asymptotic range of the respective curve, which is normally associated with the solution becoming mesh independent (Roache, 1998). It can be seen in Table 7.1 that the mean RDE and RDE-bulk values for $\Delta y = 0.05B$ were 1.0% and 0.4% respectively, while the maximum value of RDE-bulk corresponded to less than 1.0%, as shown in Figure 7.3b.

7.2.4 Developing flow velocity distributions

An analysis of the developing velocity profiles calculated with the numerical model was made for the simulations HP2, HP3, HP4 and HP5 (see Table 7.1). The velocity distributions calculated for five locations along the channel length are illustrated in Figures 7.5a to 7.5d, for the respective values of dy.
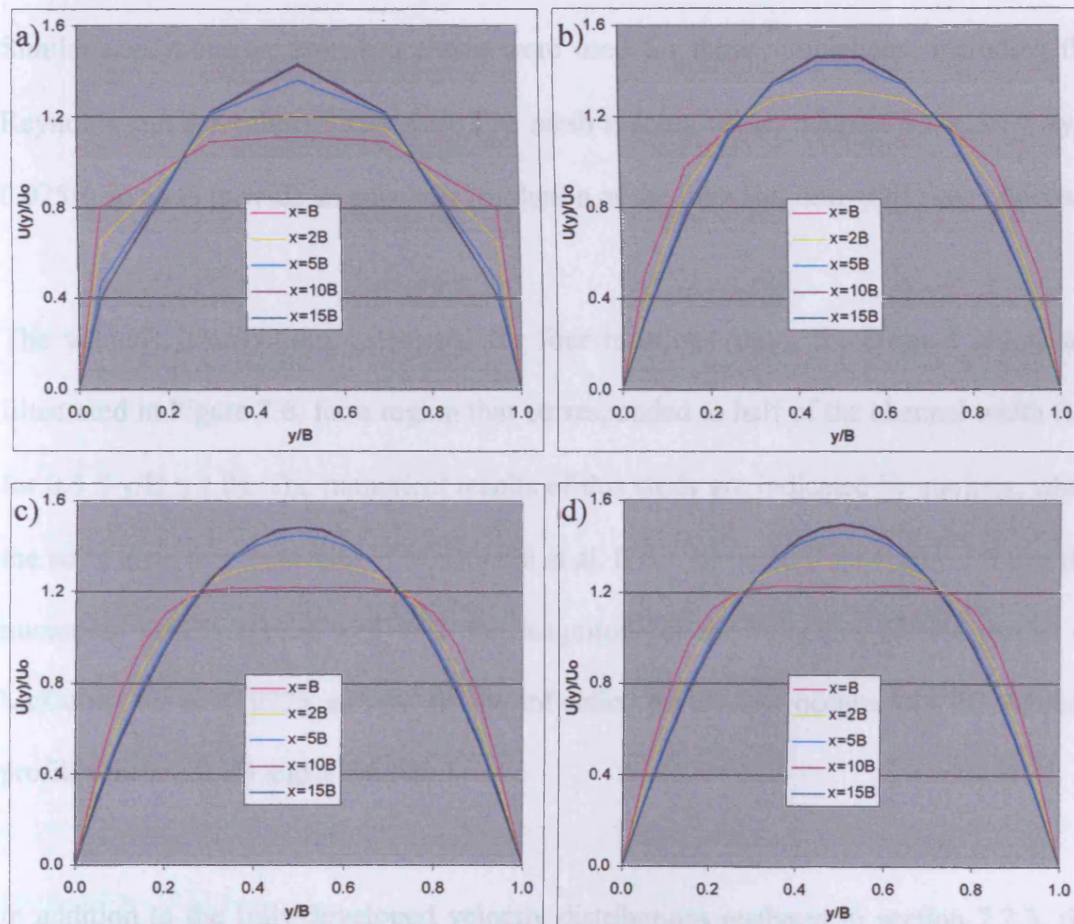
Figure 7.5 Numerical results for the developing and fully-developed velocity distributions of the Hagen-Poiseuille channel flow problem, for $\Delta x = 0.2B$ and:
a) $\Delta y = 0.2B$; b) $\Delta y = 0.1B$; c) $\Delta y = 0.05B$; d) $\Delta y = 0.025B$

It can be noticed in Figure 7.5 that the developing velocity profiles calculated by the numerical model experienced pronounced variations within the initial part of the simulated channel, i.e. for x ≤ 5B. On the other hand, the distributions calculated for x = 10B and x = 15B were practically coincident, for each corresponding value of Δy.

The numerical model predictions for the developing velocity distributions of the H-P channel flow were verified for the corresponding results of McDonald et al. (1972). Similar conditions as described above were used for these simulations, including the Reynolds number value of Re = 150. The mesh spacing values adopted were Δx = Δy = 0.025B, so as to provide an adequate resolution of the inlet and near-wall flow regions.

The velocity distributions calculated for four locations along the channel length are illustrated in Figure 7.6, for a region that corresponded to half of the channel width (i.e. for 0.5 ≤ y/B ≤ 1.0). The numerical results of this study are indicated by markers, while the solid lines represent data of McDonald et al. It can be noted from Figure 7.6 that the numerical results agreed well with the magnitude of the velocities for the results of McDonald et al. (1972), as well as the inflection points that occurred in the velocity profiles for x = 0.1B and x = 0.5B.

In addition to the fully-developed velocity distributions analysed in section 7.2.3, the numerical model was able to predict accurately the developing velocity distributions for the laminar channel flow problem, as discussed in this section. In the following section, the model verification analysis was extended to the transient and turbulent flow regimes, where the turbulent flow version of the hydrodynamic module was tested.
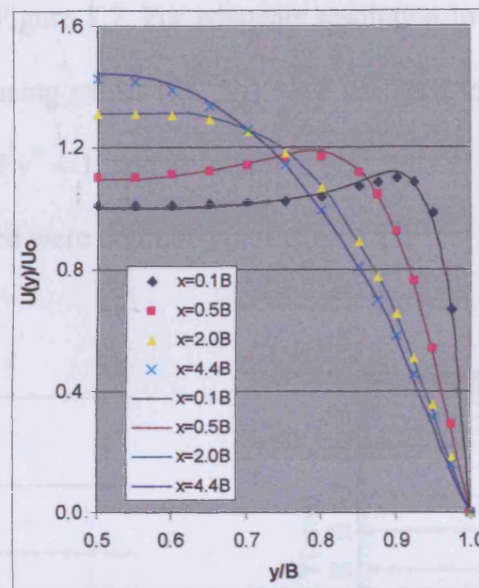
Figure 7.6 Velocity distributions of the developing Hagen-Poiseuille channel flow problem, where solid lines represent data of McDonald et al. (1972)

7.3. TURBULENT CHANNEL FLOW

The results discussed herein include the fully-developed flow results calculated from the numerical model setup for 2-D open channel flows, under the transient and turbulent flow regimes. The results analysed included the distributions of the mean streamwise velocity (U), eddy viscosity (v_t), turbulent kinetic energy (k) and the dissipation rate (ε). The corresponding numerical solutions were verified against analytical results and experimental data obtained from the literature, for both the near wall region and for depth-wise profiles.

The turbulence model used was the low Reynolds number k-ε model of Lam and Bremhorst (1981), i.e. the LB model, as described in Chapter 4. The numerical simulations were carried out using a non-uniform computational grid defined for the y

direction, as shown in Figure 7.7. For adequate resolution in the near wall region, the corresponding mesh spacing values (i.e. Δy) were designed to include at least one grid cell within the region of $y^+ < 1$, and at least five grid cells in the region $y^+ < 11.3$. The boundary conditions used were described in section 4.2.3.
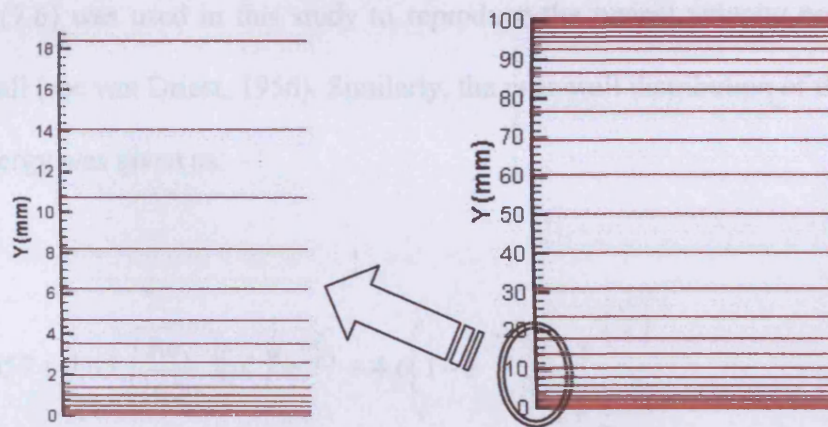
Figure 7.7 Detail of the non-uniform mesh used in the numerical model simulations of turbulent channel flow scenarios

7.3.1 Near wall flow profiles

As shown by Hinze (1975), the so-called near wall region is formed by three sub-regions, where their approximate theoretical limits defined as: i) a viscous or laminar sub-layer, for $0 < y^+ < 11.3$; ii) a buffer zone, for $11.3 < y^+ < 30–100$; and iii) a fully turbulent or logarithmic region, for $30–100 < y^+ < 300–1000$. The upper limit of the buffer zone and the limits of the logarithmic region depend on the turbulence levels in the flow.

Boyer and Laurence (2002) provided the shape function for the velocity distribution in the near wall region as being: –

$$U^+ = \frac{1}{\kappa}\ln\left(1+0.41y^+\right)+7.8\left(1-e^{-\frac{y^+}{11}}-\frac{y^+}{11}e^{-\frac{y^+}{3}}\right)$$ (7.6)

where $\kappa = 0.4187$ is the von Kármán constant, $U^+ = U/U_f$ is the normalised velocity and $y^+ = yU_f/\nu_l$ is the normalised distance to the wall, where U_f is the friction velocity. Equation (7.6) was used in this study to reproduce the typical velocity profile near a smooth wall (see van Driest, 1956). Similarly, the near-wall distribution of the turbulent kinetic energy was given as: –

$$k^+ = \left(0.057+0.05\sqrt{\frac{Re_t}{1600}}\right)\left(y^+\right)^2 e^{-\frac{y^+}{7.3}}+4.6\left(1-e^{-\frac{y^+}{20}}\right)\frac{1-e^{-\left(\frac{y^+}{3}\right)^2}}{1+\frac{4y^+}{Re_t}}$$ (7.7)

where $k^+ = k/U_f^2$ is the normalised k parameter and $Re_t = BU_f/\nu_l$ is the turbulence Reynolds number. The corresponding shape function for the dissipation rate reads: –

$$\varepsilon^+ = \frac{1}{\kappa\left[\left(y^+\right)^4+15^4\right]^{0.25}}$$ (7.8)

where $\varepsilon^+ = \nu_l\varepsilon/U_f^4$ is the normalised ε parameter. As pointed out by Boyer and Laurence (2002), Equation (7.8) reproduces the theoretical behaviour of $\varepsilon^+ \approx 1/\kappa y$ in the logarithmic region. However, in the viscous sub-layer a different pattern of variation normally occurs for the ε^+ vs. y^+ relationship, as shown by Hinze (1975), and which is not represented by Equation (7.8).

The numerical model predictions for the distributions of U^+, k^+ and ε^+ for a 2-D horizontal channel (see Figure 7.1) are shown in Figure 7.8. These results were verified against the corresponding shape functions for the transient and turbulent flow regimes, where the Reynolds number values were Re = 5,000 and Re = 30,000 respectively. The channel width was B = 600mm, while the channel length required for fully-developed flow corresponded to L = 160B. Two modelling approaches were used to calculate the parameter C_μ of the k-ε model and these approaches have been verified in this section for: i) C_μ as a constant parameter, where C_μ = 0.09; and ii) C_μ as a variable parameter, where C_μ was computed as explained in section 5.3.2.

The numerical results obtained for the U^+ profiles for Re = 5,000 and Re = 30,000 are shown in Figures 7.8a and 7.8d respectively, where a semi-log scale has been used. The analytical results shown in these figures were calculated using the shape function of Equation (7.6). An analysis of these results indicated that the numerical model predictions obtained using the variable C_μ approach provided the closest representation of the shape function for U^+. This is due to the fact that the numerical model set up for the constant C_μ approach failed to provide an accurate prediction of the velocities, mainly in the logarithmic region of the respective velocity profile.

An explanation for this finding was derived from an analysis of the calculated distribution for the normalised viscosity parameter (i.e. v_t/v_l). As shown in Figure 7.9, the use of the constant C_μ approach generated higher values of v_t/v_l in the flow, in comparison with the results for the variable C_μ approach, which increased the effects of turbulent diffusion and, thus, the flow velocities were reduced in the former case.
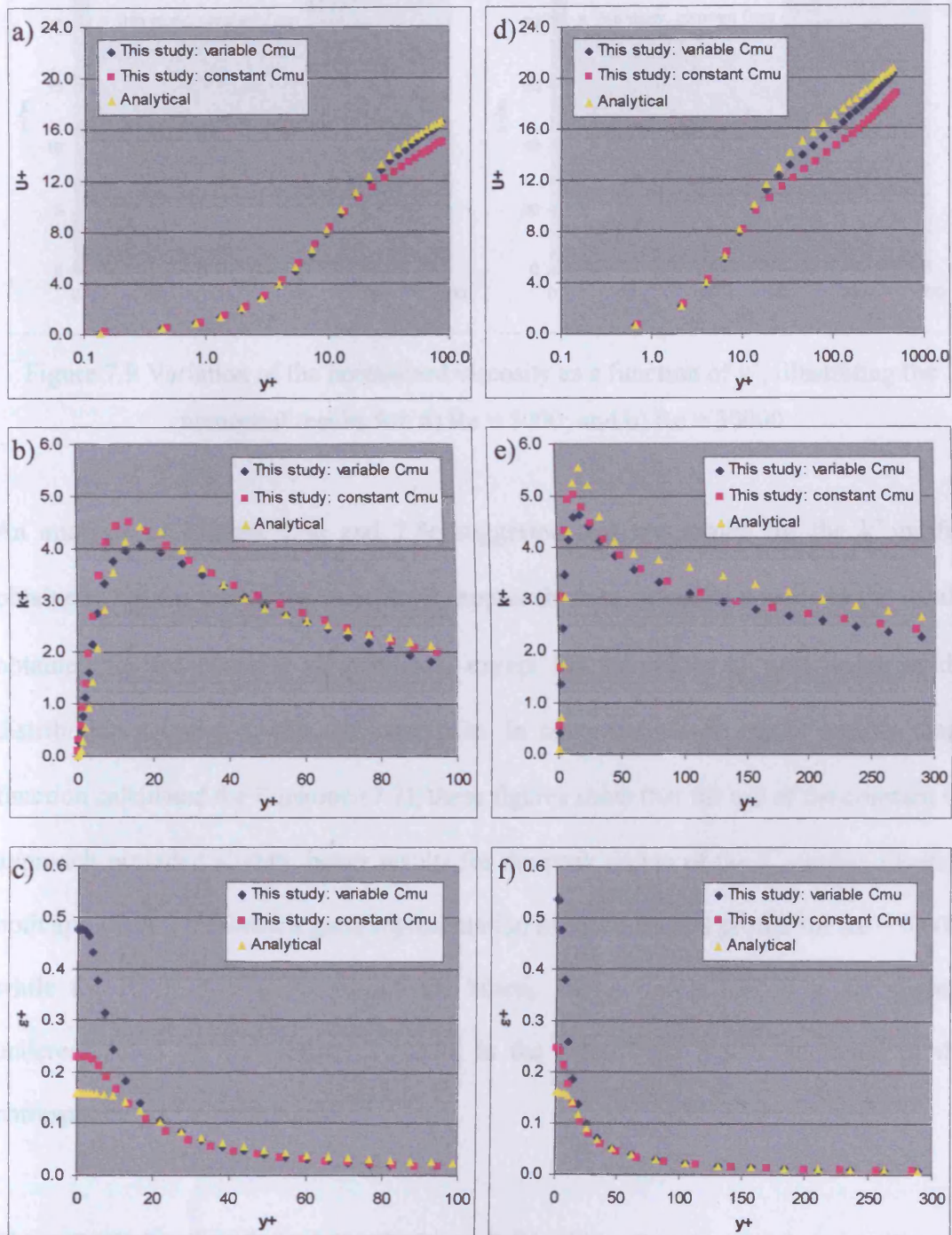
Figure 7.8 Results for the variation of flow quantities as a function of y^+ in the wall region of a 2-D turbulent channel flow, illustrating the distribution of: for Re = 5,000: a) U^+; b) k^+; and c) ε^+; and for Re = 30,000: d) U^+; e) k^+; and f) ε^+
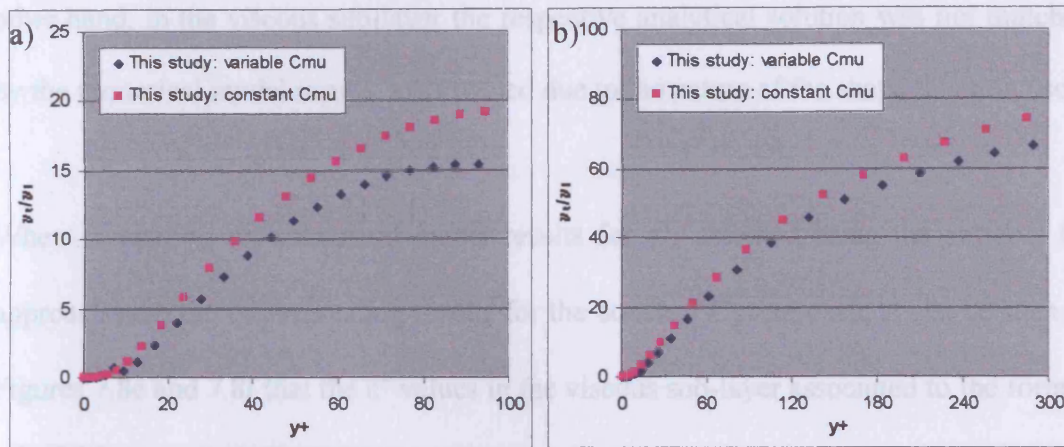
Figure 7.9 Variation of the normalised viscosity as a function of y^+, illustrating the numerical results for: a) Re = 5000; and b) Re = 30000

An analysis of Figures 7.8b and 7.8e suggested that the results for the k^+ profile obtained with the use of the variable C_μ approach were generally similar to the results obtained for the constant C_μ approach, except for the higher k^+ peak value of the distribution associated with the latter case. In comparison with the respective shape function calculated for Equation (7.7), these figures show that the use of the constant C_μ approach provided slightly better results for the peak region of the k^+ profile. Overall, both approaches provided a good representation of the analytical profile for Re = 5,000, while for Re = 30,000 the turbulence kinetic energy levels tended to be slightly underestimated by the numerical model in the logarithmic region, as found in the corresponding k^+ distributions.

The numerical and analytical distributions of ε^+ in the wall region are shown in Figures 7.8c and 7.8f, for Re = 5,000 and Re = 30,000 respectively. In both Figures, it can be seen that the values of ε^+ predicted by the numerical model for the logarithmic region were very good representations of the shape function given in Equation (7.8). On the

other hand, in the viscous sub-layer the respective analytical solution was not matched by the numerical model results, as expected due to the nature of the shape function used.

When comparing the numerical model results for ε^+, obtained using the variable C_μ approach with the corresponding results for the constant C_μ approach, it can be seen in Figures 7.8c and 7.8f that the ε^+ values in the viscous sub-layer associated to the former approach were generally higher than the corresponding results for the latter approach. In order to investigate such an effect further, the calculated C_μ values were plotted as a function of y^+ and the results are shown in Figure 7.10.
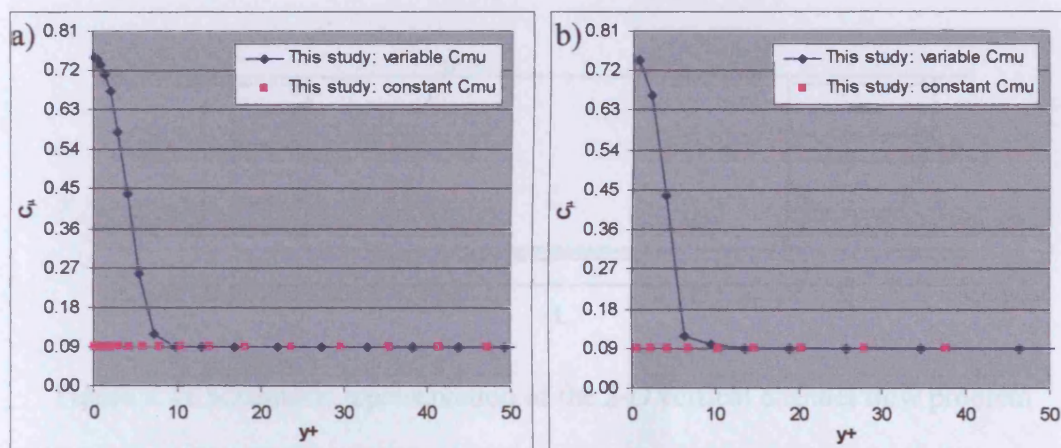
Figure 7.10 Variation of C_μ as a function of y^+, illustrating the numerical results for: a) Re = 5,000; and b) Re = 30,000

It can be seen in Figure 7.10 that the calculated values of C_μ in the viscous sub-layer were higher than the C_μ base value of $C_\mu = 0.09$, as recommended by Rodi (1993). The maximum value of $C_\mu \approx 0.74$ occurred within the region $y^+ < 1$, which was almost one order of magnitude higher than the base value. The fact that such higher values of C_μ occurred in the viscous sub-layer had a localised incremental effect on the source term

of the discretised ε equation [see Equation (5.37)]. This source term influence, combined with indirect effects, e.g. on the damping functions of the LB model, was a key factor for the increase of ε^+ in the viscous sub-layer, verified in the results for the variable C_μ approach relative to the corresponding results for the constant C_μ approach, as shown in Figure 7.8.

7.3.2 Depth-wise distributions

The numerical model results for the 2-D vertical fully-developed channel flow problem are discussed in this section, for which an illustration is given in Figure 7.11.
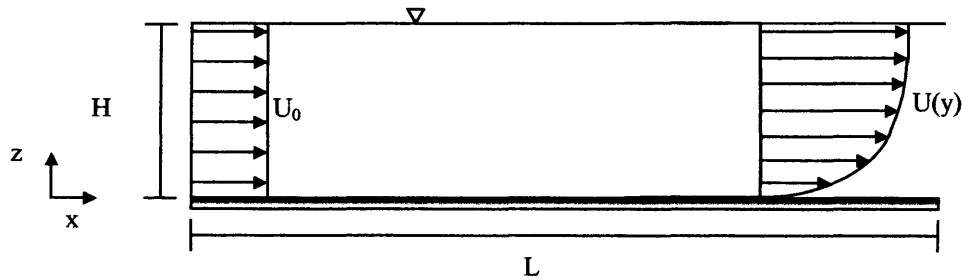
Figure 7.11 Schematic representation of the 2-D vertical channel flow problem

In Figure 7.11 U(y) represents a hypothetical fully-developed velocity profile, the water depth in the channel was H = 100mm and the channel length corresponded to L = 60H. Numerical predictions for this flow problem were compared with Direct Numerical Simulation (DNS) results and Laser Doppler Anemometry (LDA) data published in the literature. The validation analyses undertaken involved low, moderate and high turbulent intensity flows. The LB model was used and the computational mesh for these simulations was similar to the mesh illustrated in Figure 7.7.

151

For the low turbulent intensity flow case, the DNS results of Lam and Banerjee (1992) were used in the verification of the numerical model results, where the bulk Reynolds number was Re = 2,750, which was calculated as Re = $U_0 H / \nu_l$. Comparisons were carried out with the corresponding numerical solutions, as shown in Figure 7.12, for the results plotted as a function of the normalised depth (i.e. z/H).
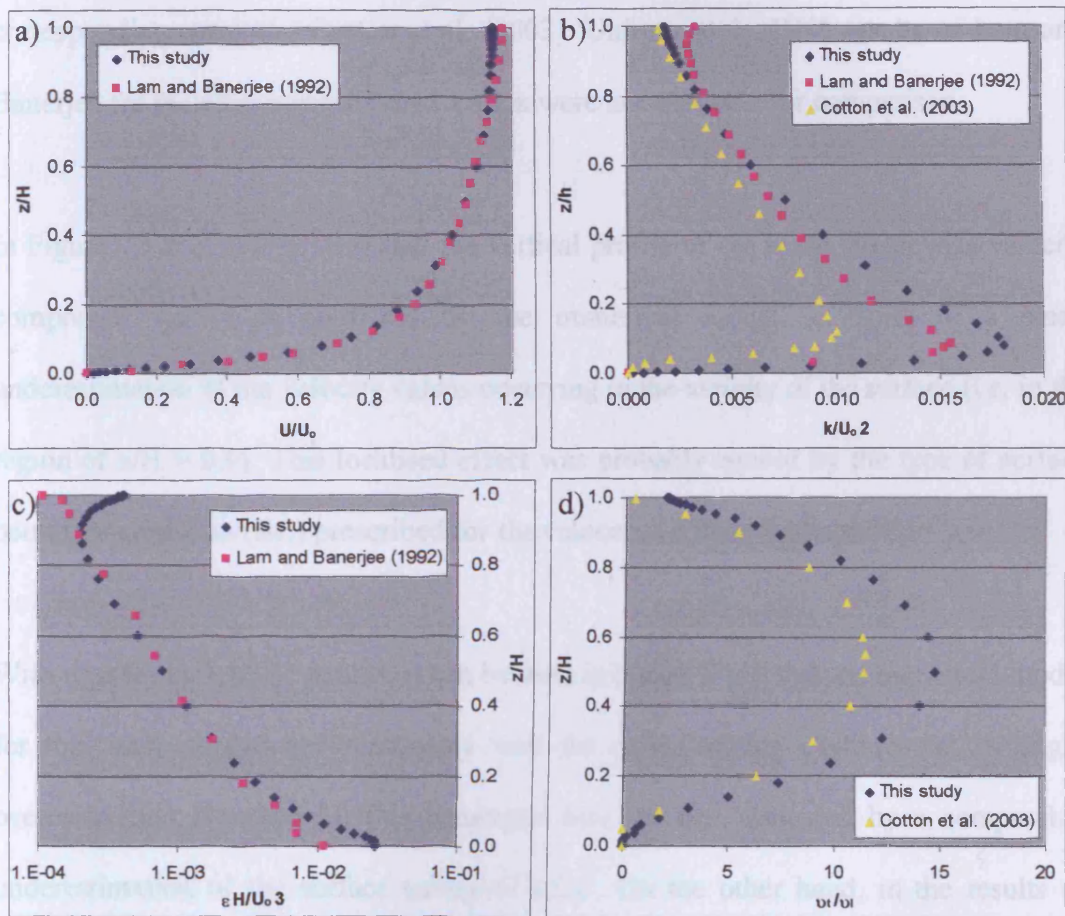
Figure 7.12 Validation of numerical model results for a low turbulence flow (Re = 2,750), illustrating the normalised vertical distributions of: a) mean streamwise velocity; b) turbulent kinetic energy; c) dissipation rate; and d) eddy viscosity

The results obtained for the normalised mean streamwise velocity component (U/U_0) are shown in Figure 7.12a, while Figure 7.12b illustrates the vertical profiles of the

normalised turbulent kinetic energy parameter (k/U_0^2). Also included in Figure 7.12b is the vertical distribution of k/U_0^2, calculated by Cotton et al. (2003), who used the low Reynolds number k-ε model of Launder and Sharma (1974) (i.e. the LS model) to simulate Lam and Banerjee's channel. In Figure 7.12c the results for the normalised dissipation rate parameter ($\varepsilon H/U_0^3$) are shown, while in Figure 7.12d the results of this study for the normalised viscosity parameter (v_t/v_l) are compared with the corresponding results of Cotton et al. (2003). Unfortunately, DNS results of Lam and Banerjee for the eddy viscosity distribution were not available for comparison.

In Figure 7.12a it can be seen that the vertical profile of the mean streamwise velocity component was well predicted by the numerical model, in spite of a small underestimation of the velocity values occurring in the vicinity of the surface (i.e. in the region of z/H > 0.9). This localised effect was probably caused by the type of surface boundary condition (BC) prescribed for the velocity, i.e. the Neumann BC.

With regard to the k/U_0^2 results, it can be seen in Figure 7.12b that the numerical model for this study reproduced reasonably well the corresponding DNS results. A slight overestimation occurred for this parameter near the bed, followed by a comparable underestimation of the surface values of k/U_0^2. On the other hand, in the results of Cotton et al. (2003) the distribution of this parameter was generally underestimated in comparison with Lam and Banerjee's results.

An explanation for the discrepancies verified between the results of this study and that of Cotton et al. may be related to a tendency for the LS model to underestimate the peak

level of the k/U_0^2 distribution occurring in the wall region, while the use of the LB model tended to provide a more accurate prediction for the corresponding values (Patel et al., 1985). In connection with this result, it was shown in the previous section that the peak of the analytical solution for the k^+ profile in the wall region was reasonably well predicted using the numerical model with the LB model.

In Figure 7.12c it can be seen that the agreement between the DNS results for the $\varepsilon H/U_0^3$ distribution and the corresponding numerical model prediction of this study was generally good in the approximate region $0.1 < z/H < 0.9$. There was an overestimation of the values calculated for the near bed and near surface zones (i.e. for the regions of $z/H < 0.1$ and $z/H > 0.9$ respectively). These discrepancies may have been as a consequence of the choice of the boundary conditions for the ε equation, which is an issue that still requires further research (Cotton et al., 2003). Nevertheless, the calculated ε distribution can be regarded overall as a satisfactory representation of Lam and Banerjee's results.

In comparing the results for the vertical distribution of v_t/v_l, found in Figure 7.12d, it can be inferred that the calculated viscosity values of this study were generally higher than the corresponding results of Cotton et al. (2003). This was probably due to the effect of the higher turbulent kinetic energy values calculated in this study, and using the LB model, as discussed above. Qualitatively speaking, however, both sets of results for the vertical profile of v_t/v_l were approximately parabolic in shape, thus mimicking the corresponding typical eddy viscosity distribution (Wilcox, 1998).

The numerical modelling of the 2-D vertical channel flow of moderate turbulence intensity was carried out for Re = 7,716, for which Laser Doppler Anemometry (LDA) data were available from Nezu and Rodi (1986). The corresponding numerical model results obtained in this study are plotted in Figure 7.13, together with the available LDA data and the results of Cotton et al. (2003).
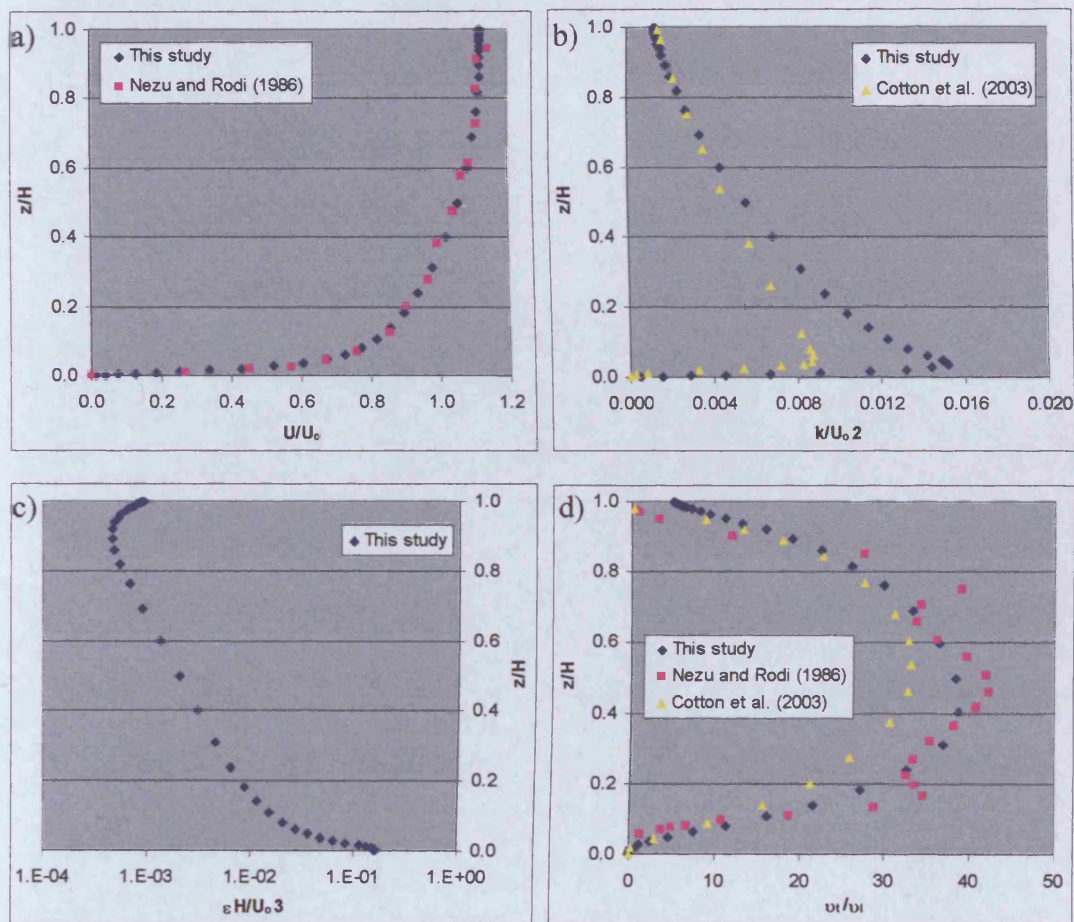
Figure 7.13 Verification of numerical results for a moderate turbulence flow (Re = 7,716), illustrating the normalised vertical distributions of: a) mean streamwise velocity; b) turbulent kinetic energy; c) dissipation rate; and d) eddy viscosity

The LDA data were available for the vertical distribution of the mean streamwise velocity component, as well as for the viscosity profile along the flow depth. These

results are shown in Figures 7.13a and 7.13d respectively. In comparison with the corresponding results of this study, it can be seen from these Figures that the data of Nezu and Rodi (1986) were very closely matched by the numerical model predictions. On the other hand, the results of Cotton et al. for the v_t/v_l profile generally smaller than the measured data, except in the region of z/H > 0.8.

With regard to the numerical model results obtained for the k/U_0^2 distribution, Figure 7.13b shows that the turbulence kinetic energy levels predicted by Cotton et al. were generally lower than the corresponding results of this study. Such a discrepancy also occurred for the low turbulence intensity case, as illustrated in Figure 7.12b. The surface values of k/U_0^2 calculated for both studies were similar, which was possibly due to the type of surface BC for k being the same, i.e. the Neumann BC.

The results of this study for the vertical distribution of $\varepsilon H/U_0^3$ are shown in Figure 7.13c. Unfortunately, no data or other numerical model results were available to verify the accuracy of these results. However, the general trend of the profile followed that calculated for the low turbulence intensity case, shown in Figure 7.12c, i.e. with local maximum values of the dissipation rate occurring near the bed and surface.

For the high turbulence intensity case, the bulk Reynolds number of the simulations was Re = 68,860. The numerical predictions of the normalised mean velocity and viscosity distribution were verified with the LDA data obtained by Nezu and Rodi (1986). A comparison of these results can be seen in Figure 7.14.
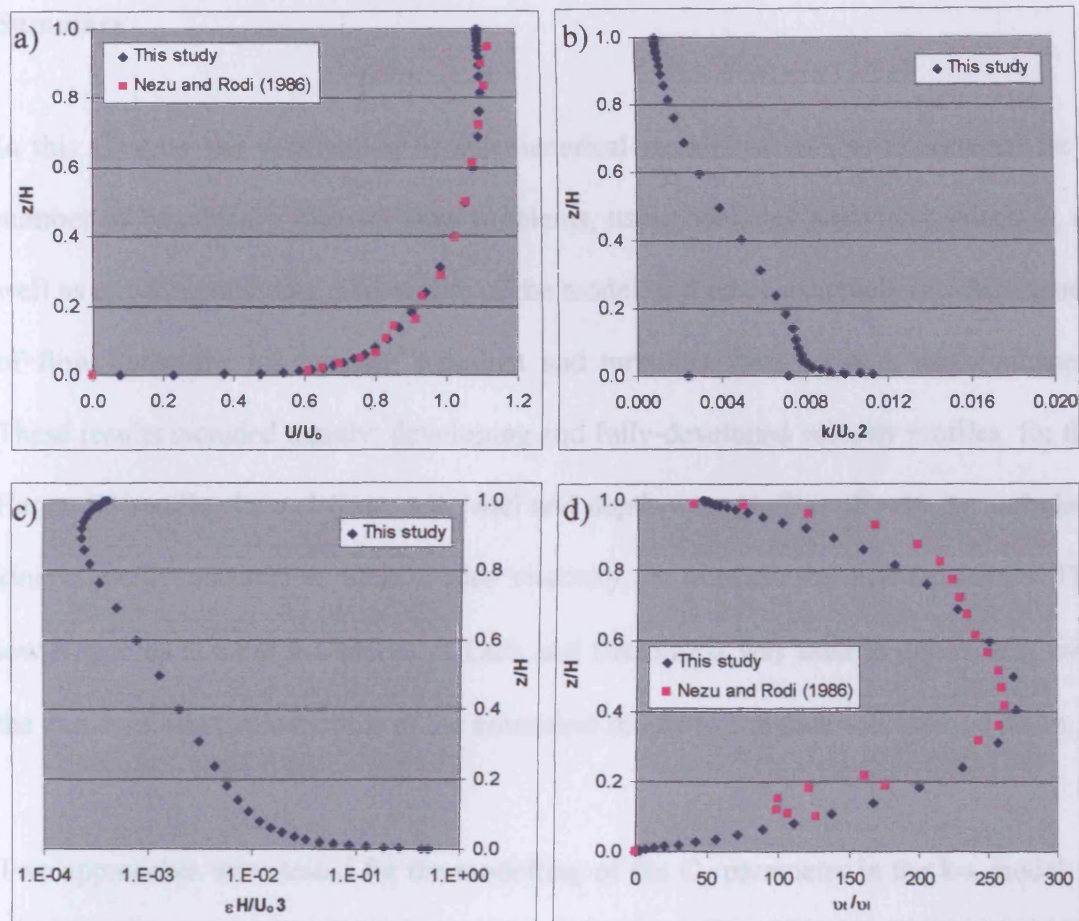
Figure 7.14 Validation of numerical model results for a high turbulence flow
(Re = 68,860), illustrating the normalised vertical distributions of: a) mean streamwise
velocity; b) turbulent kinetic energy; c) dissipation rate; and d) eddy viscosity

It can be seen in Figures 7.14a and 7.14d that the agreement with the numerical model results of this study and the corresponding data were very good, for both the mean streamwise velocity and the viscosity distributions. The numerical results of this study for the vertical distributions of k/U_0^2 and $\varepsilon H/U_0^3$ are shown in Figures 7.14b and 7.14c respectively. Unfortunately, no corresponding data were available to verify the accuracy of such numerical model predictions. Nonetheless, the general trend of the k/U_0^2 and

$\varepsilon H/U_0^3$ distributions was similar to that of the results for the low and moderate

turbulence intensity flows, as shown above.

Summary

In this Chapter the verification of the numerical model results was undertaken for a number of benchmark channel flow problems, using available analytical solutions, as well as experimental data. The ability of the model to predict accurately the distribution of flow quantities for laminar, transient and turbulent flow regimes was evaluated. These results included mainly: developing and fully-developed velocity profiles, for the Hagen-Poiseuille channel flow; near wall and depth-wise profiles of velocity, turbulent kinetic energy, dissipation rate and eddy viscosity, for transient and turbulent flows. The low Reynolds number k-ε model of Lam and Bremhorst was used in connection with the core hydrodynamic module of the numerical model to simulate non-laminar flows.

Two approaches were tested for the modelling of the C_μ parameter in the k-ε model: i) as a constant quantity, where C_μ = 0.09; and ii) as a variable quantity, where the variation of C_μ was a function of the ratio between turbulence production and dissipation. The results for the variable C_μ approach were found to better represent the distribution of turbulence quantities in the near wall region of the flow, which had a positive effect on the corresponding velocity distribution results. Overall, the numerical model was able to predict accurately the mean velocity distributions and eddy viscosity profiles of the channel flows tested, which consisted of the main flow quantities of interest in this study. In Chapter 8 the validation analysis of the numerical model results is extended, using experimental data acquired in prototype contact tanks.

Chapter 8

Numerical Model Application to Contact Tanks

8.1. INTRODUCTION

This Chapter includes the validation analyses of the hydrodynamic and solute transport modules of the numerical model described in Chapter 5, which were carried out using physical experimentation results for scaled hydraulic models of contact tanks (CTs).

In section 8.2 the results of the two-dimensional (2-D) numerical simulations have been compared with measured mean velocity field and tracer experimentation data. Likewise, in section 8.3 the three-dimensional (3-D) ADV results and tracer transport data acquired in the model of the Prototype Tank (PT) were used to validate the numerical model predictions for two design setups of the tank. An analysis of sensitivity of the results obtained was carried out, which involved two turbulence modelling approaches and the variation of the turbulent Schmidt number.

8.2. TWO-DIMENSIONAL FLOW AND SOLUTE TRANSPORT

This section includes the results of the 2-D numerical simulations carried out for two different baffled CTs. Experimentation data from the studies of Teixeira (1993) and Rauen (2001) were used in the comparisons with the respective numerical model predictions. For the prototype tank of the former, a comparison was performed that involved the numerical and measurement results, for the depth mean velocity field in a region of 2-D horizontal flow. Tracer experimentation data for the latter tank were used to validate the simulation results of the 2-D solute transport module.

8.2.1   Hydrodynamic results

Hydrodynamic numerical simulations were carried out for the prototype CCT investigated experimentally by Teixeira (1993), for which a schematic representation is shown in Figure 8.1. Laser Doppler Anemometry (LDA) data from that study were used to verify the ability of the numerical model to predict the mean 2-D velocity field in the tank. Specifically, the numerical model results were evaluated for the cross-section of the tank represented by the shaded area in Figure 8.1 and where a horizontally reversed flow occurred (Teixeira, 1993).
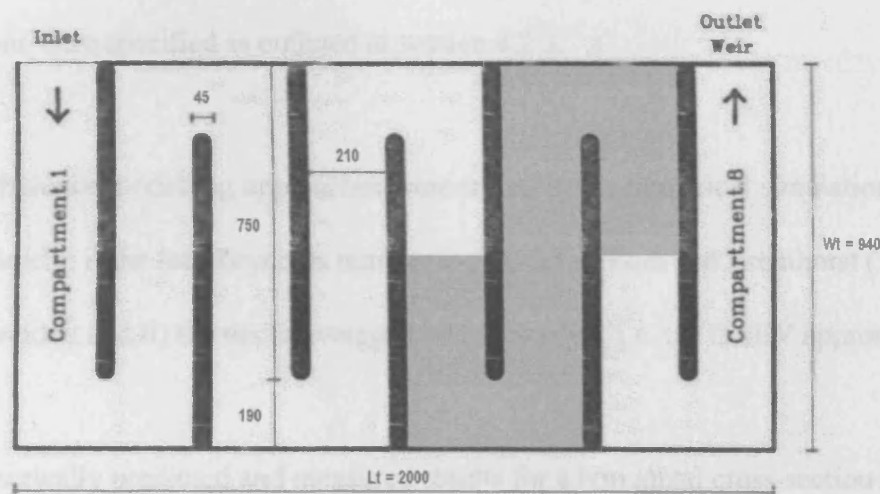
Figure 8.1 Schematic representation of the contact tank of Teixeira (1993), where the shaded area represents the assessed cross-section of the 2-D flow (dimensions in mm)

The numerical simulations of Teixeira's unit were carried out for two non-uniform mesh configurations, namely mesh A and mesh B, which had the characteristics listed in Table 8.1. The number of grid cells in the x and y directions were represented by the parameters N_x and N_y respectively, while the corresponding finest and coarsest mesh spacings were given as Δx_{min}, Δx_{max}, Δy_{min}, Δy_{max}.

Table 8.1 Mesh characteristics for the prototype contact tank of Teixeira (1993)

Mesh configuration	Δx_{min}	Δx_{max}	Δy_{min}	Δy_{max}	N_x	N_y
A	2.0mm	40mm	1.0mm	25mm	40	209
B	2.0mm	25mm	2.0mm	25mm	52	177

The flow rate per unit depth (Q_H) was used as the inlet boundary condition for the 2-D hydrodynamic simulations of Teixeira's tank, where $Q_H = 2,183 mm^3/s/mm$. This parameter was calculated as the ratio between the experimentation flow rate (Q) and the water depth in the tank (H), as reported by Teixeira, where $Q = 1.17 l/s$ and $H = 536 mm$. Consequently, the bulk velocity in the compartments was $U_0 \approx 10 mm/s$, which corresponded to the value found in the experimentation tank. The other boundary conditions were specified as outlined in section 4.2.3.

Two turbulence modelling approaches were tested in the numerical simulations for this CCT, namely: i) the low Reynolds number k-ε model of Lam and Bremhorst (1981), i.e. the LB model; and ii) the depth-averaged eddy viscosity, i.e. the DAEV approach.

The numerically predicted and measured results for a horizontal cross-section located in the region of the 2-D flow in the tank are shown in Figure 8.2. The assessed region included Compartment 6 and a portion of Compartments 5 and 7, as well as the corresponding transition regions between the compartments. The x and y direction coordinates were normalised by including the respective tank dimension, as shown in Figure 8.1. Likewise, the mean resultant velocity was normalised by including the bulk velocity, giving $\vec{UV}/U_0$.

The numerical model predictions obtained using the LB model for meshes A and B are shown in Figures 8.2b and 8.2c respectively, while Figure 8.2d shows the results obtained using the DAEV approach and mesh B. The corresponding mean velocity field measured by Teixeira is shown in Figure 8.2a.
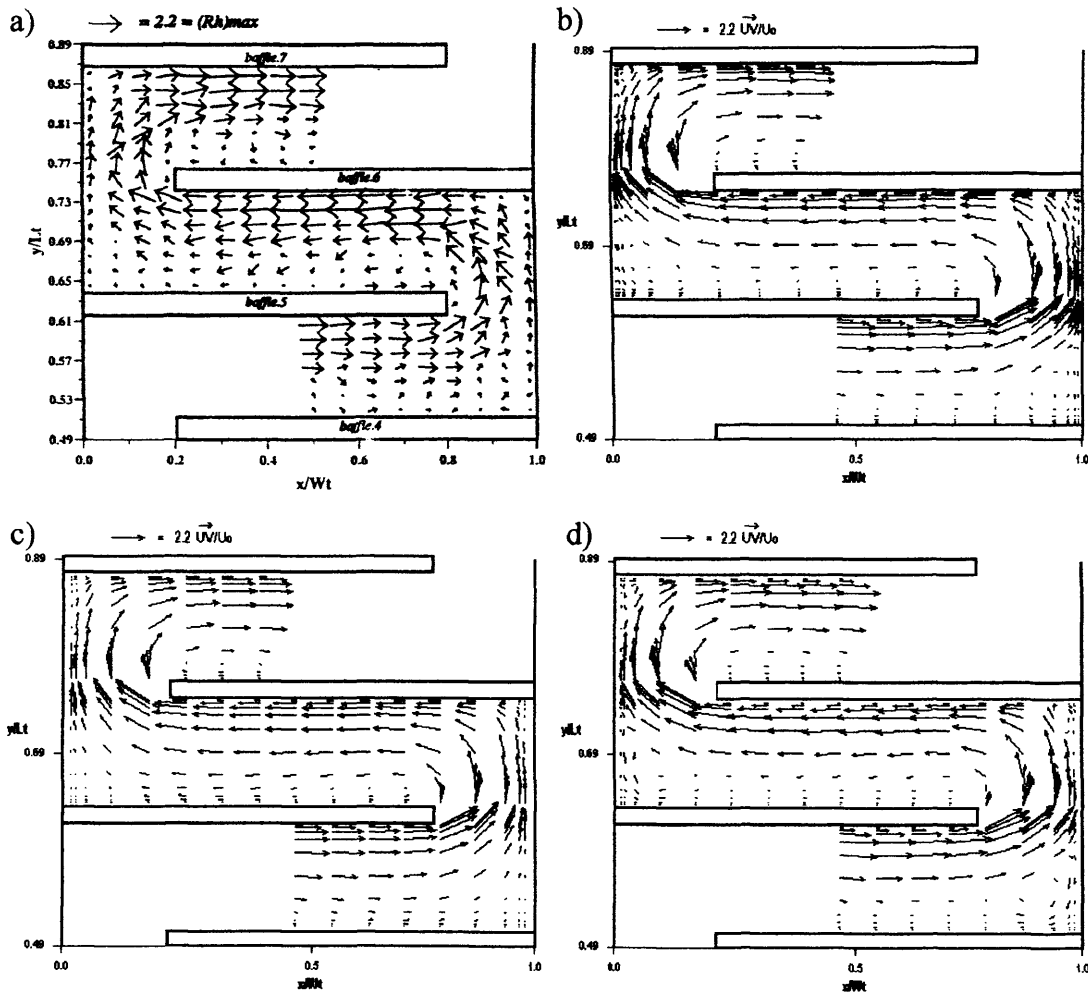
Figure 8.2 Mean 2-D velocity field for the contact tank of Teixeira (1993), illustrating: a) measured results; and the numerical predictions for: b) LB model with mesh A; c) LB model with mesh B; d) DAEV approach with mesh B

A comparison of the results presented in Figure 8.2 indicated that overall the numerical model predictions were in satisfactory agreement with the measured data for this mean

2-D velocity field. It can be seen that the main advective flow path was generally well represented in Figures 8.2b, 8.2c and 8.2d, as occupying approximately half of the compartment width next to the corresponding downstream baffle. In addition, the location of the dead zones in the flow domain were correctly predicted, as occurring at the upstream and downstream corners of the transition regions, as well as behind the baffles. Nevertheless, not all of the numerical model setups tested in this analysis provided an accurate prediction of the size of the recirculating flow zone behind Baffle 5, as highlighted in the following discussion.

As can be seen in Figure 8.2a for Teixeira's results, a recirculation zone occurred in the experimentation tank in the region of $0.45 < x/Wt < 0.8$ and $0.64 < y/Lt < 0.69$ approximately. In comparing this region with the corresponding numerical model results in Figures 8.2, 8.2c and 8.2d, it can be seen that the recirculating flow structure was better represented by the numerical model results of Figure 8.2c, which corresponded to the use of the LB model with mesh B. With this numerical model setup the approximate location predicted for the recirculating flow reattachment point was $x/Wt \approx 0.5$, as depicted by the streamtrace plot of Figure 8.3b. On the other hand, as shown in Figures 8.3a and 8.3c, when using the other numerical model setups the predicted length of the recirculation zone was extended up to the transition region leading to Compartment 7, indicating that there was an overestimation of the size of the recirculation zone under consideration, with the use of the corresponding numerical model setups.
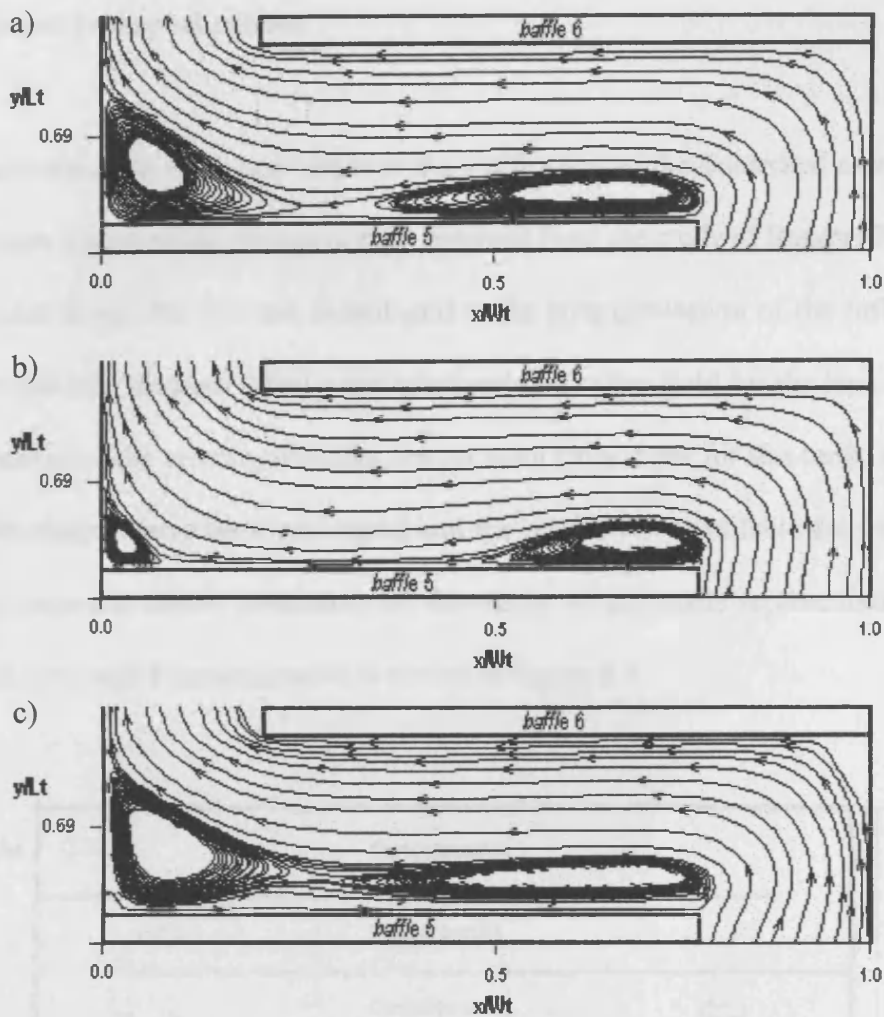
Figure 8.3 Streamtrace plots predicted by the numerical model for Compartment 6 of the contact tank of Teixeira (1993), illustrating the results for: a) LB model with mesh A; b) LB model with mesh B; c) DAEV approach with mesh B

The main causes identified for the discrepancies in the prediction of the size of the horizontal recirculation zone were twofold: i) in Figures 8.2b and 8.3a, a lack of resolution of the computational mesh in the streamwise (i.e. x) direction of the flow; and ii) in Figures 8.2d and 8.3c, a relatively poor representation of the local turbulence effects on the mean flow when using the DAEV approach. Therefore, this analysis suggested that the use of the LB model with a relatively fine mesh in the streamwise direction was recommended for a better performance of the 2-D hydrodynamic module.

8.2.2 Solute transport results

The experimentation data used herein in the verification of the numerical model results for the conservative solute transport were obtained from the study of Rauen (2001). The type of inlet design for this unit contributed to the homogenisation of the inflow along the water column, thus providing a predominantly 2-D flow field for the tank. Whereas an assessment of the velocity field has not yet been carried out for this tank, a series of tracer experiments have been performed and the results were available for comparison with the numerical model predictions of this study. A schematic representation of the simulated tank with 6 compartments is shown in Figure 8.4.
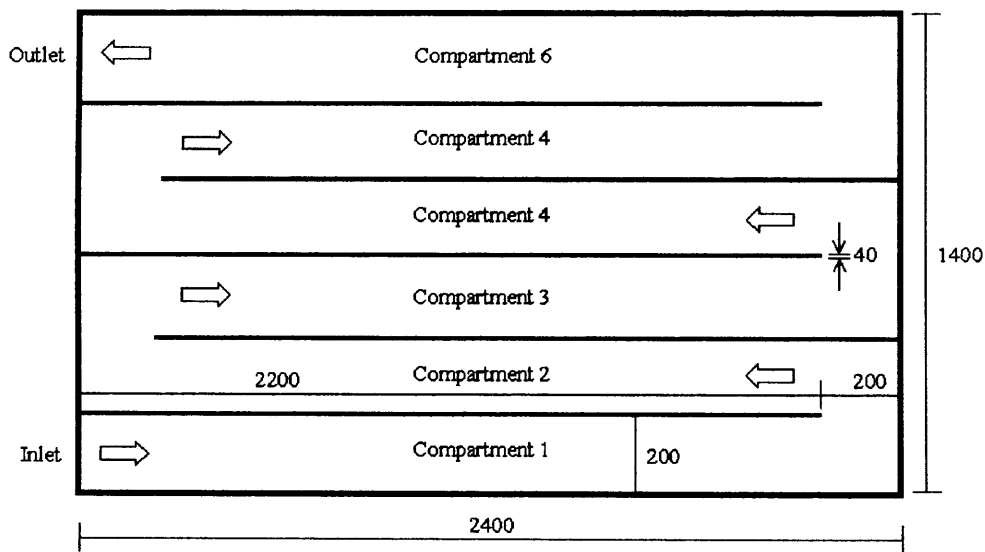
Figure 8.4 Schematic representation of the model contact tank of Rauen (2001)
(dimensions in mm)

The experimentation flow rate used by Rauen (2001) was Q = 1.16l/s, which gave a mean water depth in the tank of H = 500mm. The bulk mean velocity was $U_0 \approx 12$mm/s and the bulk Reynolds number was Re $\approx 1,000$.

166

The computational grid defined for the prototype CCT of Rauen (2001) was modelled using 17,270 cells, with 110 cells in the x direction and 157 cells in the y direction. The corresponding mesh spacings were specified similarly to those of mesh B in section 8.2.1, as shown in Table 8.1.

The steady-state mean velocity field and viscosity distribution in the tank were predicted using the hydrodynamic module, with the turbulence modelling being simulated using either one of two approaches, i.e. the LB model or the DAEV approach. The flow rate per unit depth was used as the inflow boundary condition for the hydrodynamic simulation of the tank, such that $Q_h = 2,320 mm^3/s/mm$. Figure 8.5 illustrates the simulation results obtained with the use of the LB model.
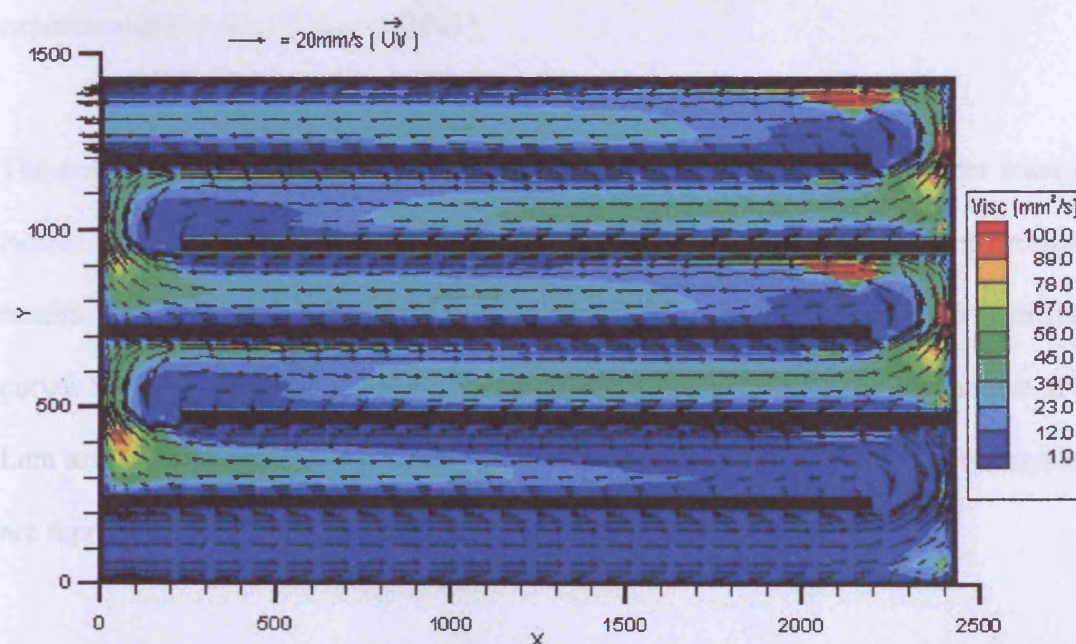
Figure 8.5 Steady-state velocity field and distribution of effective viscosity as calculated for the contact tank of Rauen (2001), using the LB model (dimensions in mm)

Using the steady-state flow field solution obtained for each turbulence modelling approach, the transient solute transport module was used to simulate "black box" tracer experiments (see section 3.4.2), where the solute input and the corresponding output readings were recorded at the inlet and outlet sections of the tank respectively. The initial and boundary conditions for these numerical simulations were prescribed as in section 4.3.3. The duration of the simulated tracer injection was 5s, while the value of the average tracer concentration in the tank was $C_0 = 7.0$mg/l.

Three values of the Schmidt number, i.e. Sch = 0.75, 1.0 and 1.25, were tested in the simulations of the solute transport module, in order to evaluate the effect of this parameter on the predicted hydraulic behaviour of the tank. The results obtained were normalised to allow comparisons to be made with the corresponding tracer experimentation data of Rauen (2001).

The obtained retention time distribution (RTD) curves and accumulated tracer mass (F) curves are illustrated in Figure 8.6, together with the corresponding experimental results. The values of the hydraulic efficiency indicators (HEI) associated with these curves are shown in Table 8.2. The solute transport results associated with the use of the Lam and Bremhorst turbulence model and the depth-averaged eddy viscosity approach are represented as the LBM and DAEV approaches respectively.

As can be seen in Figure 8.6a, the results obtained using the DAEV approach were not a particularly good representation of the experimental data for these numerical simulations. It can be seen from the figure that, despite the variation in the Schmidt

number, the tracer curves for the DAEV approach showed an earlier rise time and a larger overall spread in comparison with the experimental curve, indicating that unduly high levels of short-circuiting and mixing were predicted by the numerical model for the tank. Significant discrepancies between the experimental results and the numerical model results associated with the DAEV approach can also be seen in Figure 8.6b for the F curves.
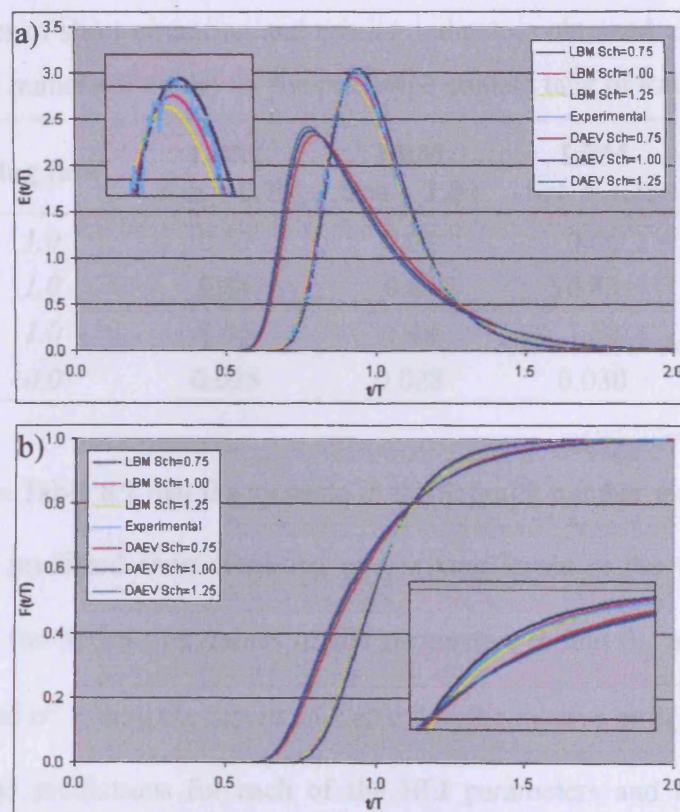
Figure 8.6 Experimental and numerical tracer curves for the contact tank of Rauen (2001), illustrating: a) RTD curves; and b) accumulated tracer mass curves

On the other hand, good agreement was observed between the experimental RTD curve and the corresponding numerical model prediction associated with the use of the LB model. Furthermore, it can be seen in Figure 8.6a that the peak concentration level of

the curve was better predicted with the use of Sch = 0.75. With regard to Figure 8.6b, the experimental F curve was closely matched by the corresponding numerical model results, while any influence of the Schmidt number on the behaviour of the numerical F curves could not be detected. The effects of this parameter on the levels of short-circuiting and mixing predicted using the LB model, were further investigated using the corresponding HEI results, as shown below.

Table 8.2 Values of short-circuiting and mixing indicators obtained experimentally and predicted by the numerical model for the prototype contact tank of Rauen (2001)

HEI	Plug flow	LBM Sch = 0.75	LBM Sch = 1.00	LBM Sch = 1.25	Experimental
θ_i	1.0	0.67	0.67	0.66	0.70
θ_{10}	1.0	0.84	0.83	0.83	0.84
Mo	1.0	1.45	1.48	1.50	1.47
σ^2	0.0	0.025	0.028	0.030	0.029

It can be seen in Table 8.2 that the increase in the Schmidt number tended to lead to an increase in the predicted short-circuiting and mixing levels in the tank, as indicated respectively by the decreasing values of the parameters θ_i and θ_{10} and the increasing values of Mo and σ^2. Using the results of Table 8.2, the relative error (RE) between the numerical model predictions for each of the HEI parameters and the corresponding experimental results are given in Table 8.3.

In Table 8.3 the lowest error value calculated for each HEI parameter is shown in bold. As can be seen for these results, the numerical model simulations, as undertaken for the prototype tank of Rauen (2001) with Sch = 0.75, provided the best predictions for the parameter θ_i, which represents the start of the tracer passage through the outlet of the

tank. On the other hand, the lowest error value obtained for θ_{10} occurred for Sch = 1.0.

As discussed in section 6.3.2, and recommended by Teixeira and Siqueira (2005), preference should be given to the use of θ_{10} as a short-circuiting indicator, which suggested that the use of Sch = 1.0 was related to a more accurate prediction of the short-circuiting levels for the tank. With regard to the mixing levels, the use of Sch = 1.0 was also related to the lowest error values being calculated for the parameters Mo and σ^2, as can be seen in Table 8.3.

Table 8.3 Relative errors of the predictions for the short-circuiting and mixing indicators for the prototype contact tank of Rauen (2001)

HEI	LBM Sch = 0.75	LBM Sch = 1.0	LBM Sch = 1.25
RE-θ_i	-3.6%	-4.4%	-5.2%
RE-θ_{10}	0.7%	-0.1%	-0.8%
RE-Mo	-1.8%	0.1%	1.6%
RE-σ^2	-13.8%	-3.4%	3.4%

It can be concluded from this analysis that the use of Sch = 1.0 in the numerical model simulations, with the 2-D solute transport module for the prototype CCT of Rauen (2001), generated the best predictions for the short-circuiting and mixing levels relative to the corresponding experimental data. Furthermore, the results obtained using the LB model were significantly better than the corresponding predictions obtained for the DAEV approach. This was probably due to a more accurate prediction being made for the size of the horizontally reversed flow zones in the tank, as discussed in section 8.2.1. In the following section the verification of numerical model results was extended to predictions of the 3-D hydrodynamic and solute transport modules, where the effect of the type of turbulence model on the predicted results was again investigated further.

8.3. THREE-DIMENSIONAL FLOW AND SOLUTE TRANSPORT

The three-dimensional (3-D) versions of the hydrodynamic and solute transport modules of the numerical model described in Chapter 5 were used to calculate the steady-state flow field and transient solute transport processes for two configurations of the Prototype Tank (PT) of this study, namely setups OS-C and MS4-C. The physical experimentation data used to verify the numerical model results were the 3-D ADV results and tracer curves as introduced in Chapter 6.

The 3-D numerical simulations were carried out for similar conditions as those established during the experimentation, which included a steady state flow, a flow rate value of Q = 3.7l/s and a mean water depth in the tank of H = 1010mm. The bulk velocity in the compartments was $U_0 \approx$ 10mm/s, which resulted in a bulk Reynolds number of $Re_b \approx$ 1540. At the inlet section the bulk velocity was $U_{0in} \approx$ 92mm/s, while the corresponding Reynolds number was $Re_{in} \approx$ 6290.

8.3.1 Setup OS-C

8.3.1.1 Hydrodynamic results

The hydrodynamic results for this section included the mean velocity fields measured in the vertical and horizontal planes for the OS-C experimentation tank setup. This setup was represented schematically in Figure 3.3.

Two turbulence modelling approaches were used in the simulations in the hydrodynamic module, with these approaches being described in section 4.2.2 as: i) the depth-averaged eddy viscosity, i.e. the DAEV approach; and ii) the low Reynolds number k-ε model of Lam and Bremhorst (1981), i.e. the LB model. For the application of the LB model, the coefficient C_μ, which is part of the k-ε turbulence model, was regarded as a variable parameter, being expressed as a function of the ratio between the turbulence production and dissipation rate, as explained in Chapter 5.

Three mesh configurations were used to represent the computational domain for setup OS-C, namely meshes A, B and C. These meshes had a total of 194,922, 365,344 and 506,432 cells respectively, with their specifications being given in Table 8.4. The numerical model simulations using the DAEV approach were carried out for mesh A, while the simulations using the LB model were performed for all three meshes.

Table 8.4 Computational mesh characteristics for setup OS-C

Mesh	Δx_{min}	Δx_{max}	Δy_{min}	Δy_{max}	Δz_{min}	Δz_{max}	N_x	N_y	N_z
A	10mm	50mm	5mm	40mm	5mm	100mm	49	153	26
B	10mm	50mm	1mm	40mm	2mm	100mm	49	233	32
C	2mm	30mm	2mm	45mm	2mm	100mm	82	193	32

The physical and computational domains of setup OS-C are illustrated in Figure 8.7. The computational mesh shown in Figure 8.7b corresponds to mesh A, as defined in Table 8.4.
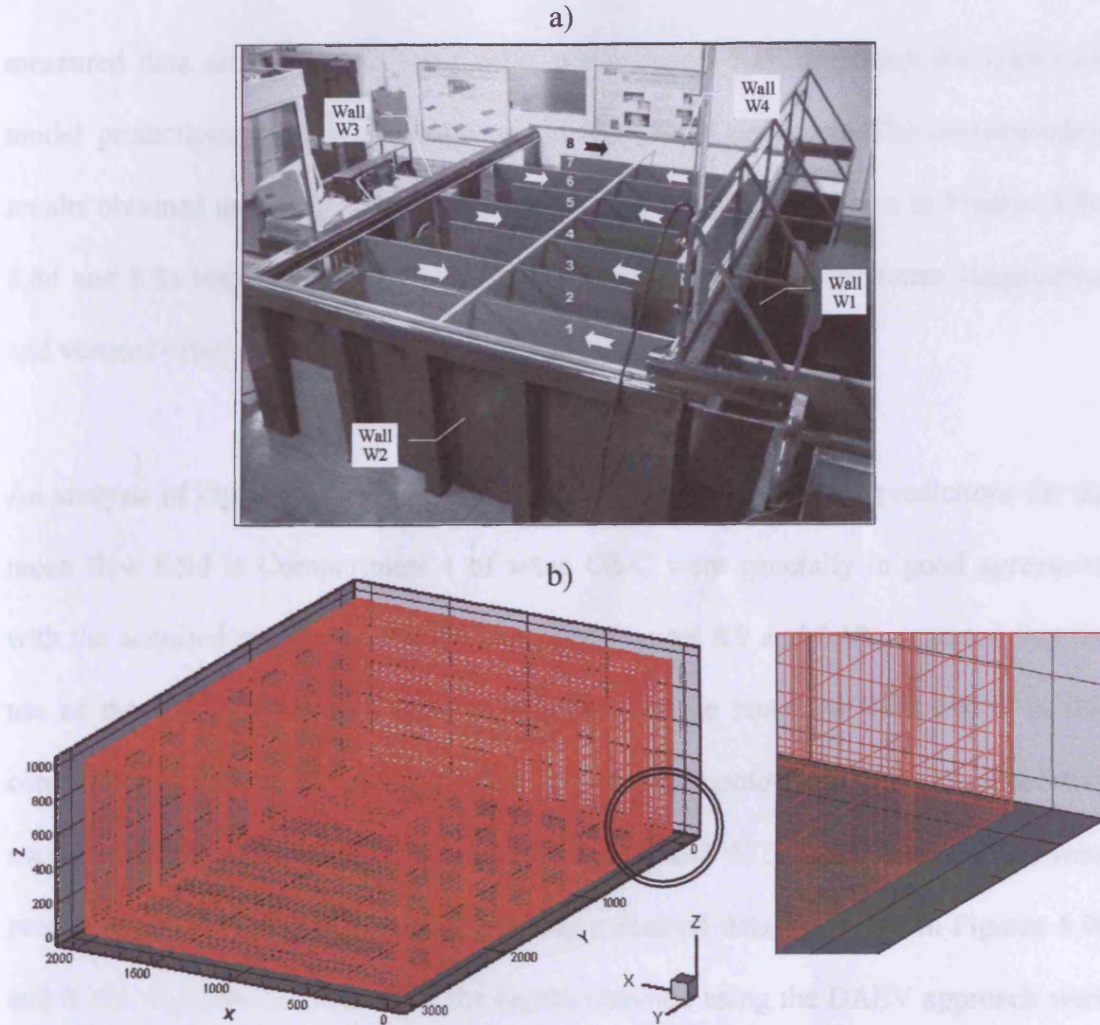
Figure 8.7 Illustration of setup OS-C of the experimentation tank, showing:
a) photographic representation; and b) non-uniform mesh A

The ADV data obtained from Assessment OS-A1 were compared with the corresponding numerical model results for Compartment 1 of setup OS-C. As shown in section 6.2.1, the flow field in this region of the tank was dominated by a vertically reversed flow structure, which was caused by the relative position of the inlet section associated to flow deflection by the wall W3 and the tank bed. Figure 8.8 illustrates the experimental data and the corresponding numerical results for the normalised mean velocity field (i.e. $\vec{UW}/U_0$) along the mid-width vertical plane of Compartment 1. The

measured data are shown in Figure 8.8a, while Figure 8.8b illustrates the numerical model predictions obtained with the use of the DAEV approach. The corresponding results obtained using the LB model for meshes A, B and C are shown in Figures 8.8c, 8.8d and 8.8e respectively. The corresponding contour plots of the mean longitudinal and vertical velocity components are shown in Figures 8.9 and 8.10.

An analysis of Figures 8.8, 8.9 and 8.10 indicated that the numerical predictions for the mean flow field in Compartment 1 of setup OS-C were generally in good agreement with the acquired experimental data. However, Figures 8.9 and 8.10 suggested that the use of the LB model caused an overestimation of the reversing flow region in this compartment. As can be seen from these figures, the contour areas for the respective maximum reversed flow velocities (i.e. $U/U_0 = -3.5$ and $W/U_0 = 1.0$ respectively) were predicted to be larger than the corresponding measured data, as shown in Figures 8.9a and 8.10a respectively. Therefore, the results obtained using the DAEV approach were in closer agreement with the experimental data for this particular cross-section.

The experimental results for Assessment OS-A2 have been compared with the numerical model predictions for the vertical profiles of the mean resultant velocity in the compartments for setup OS-C, as shown in Figure 8.11. In comparing the experimental results in Figure 8.11a with the corresponding numerical model predictions, it can be seen from Figure 8.11b that the use of the DAEV approach provided a better prediction of the data, relative to the results obtained using the LB model.
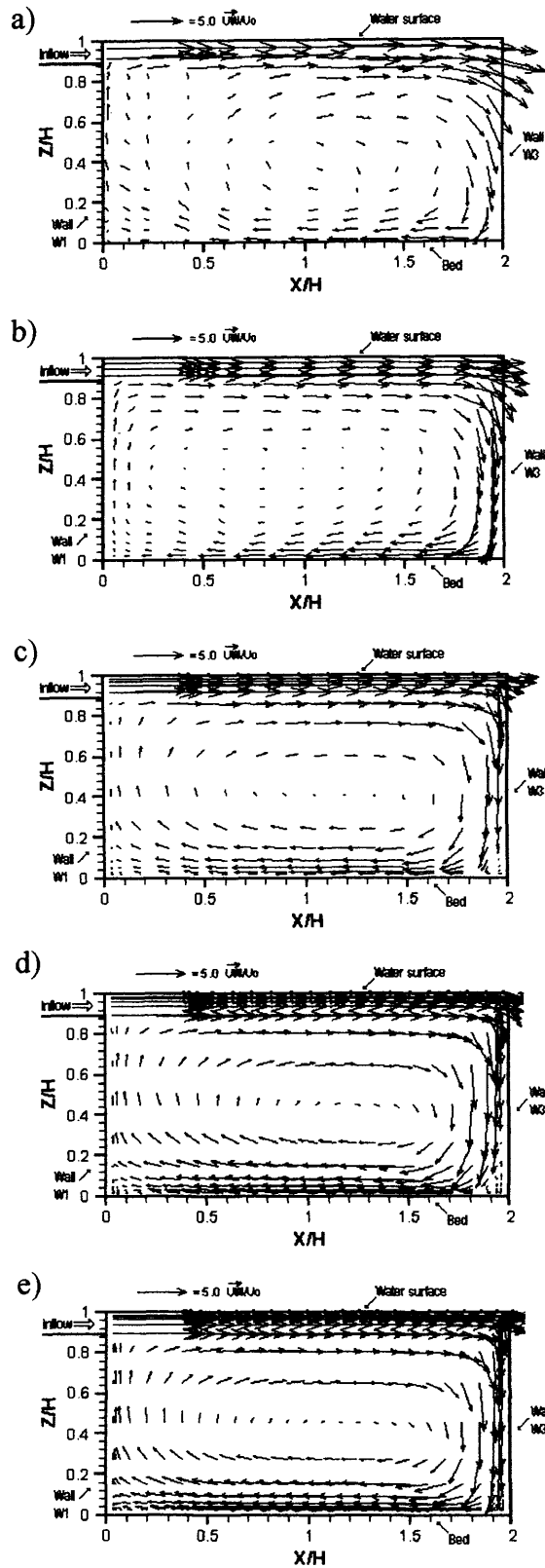
Figure 8.8 Mean resultant velocity field in Compartment 1 for setup OS-C, obtained for:

a) ADV measurements; and numerical simulations using: b) the DAEV approach for

mesh A; and the LB model for: c) mesh A; d) mesh B; and e) mesh C
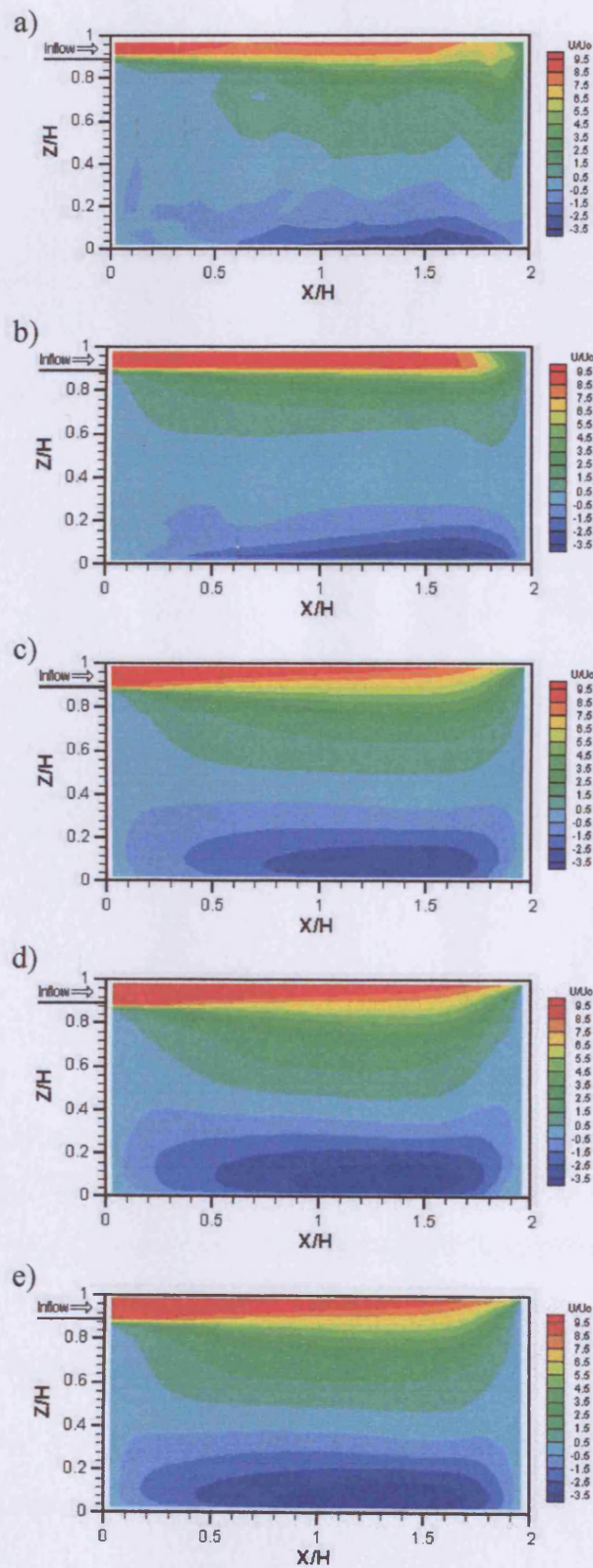
Figure 8.9 Contour plot of mean longitudinal velocity in Compartment 1 for setup OS-C obtained for: a) ADV measurements; and numerical simulations using: b) the DAEV approach for mesh A; and the LB model for: c) mesh A; d) mesh B; and e) mesh C
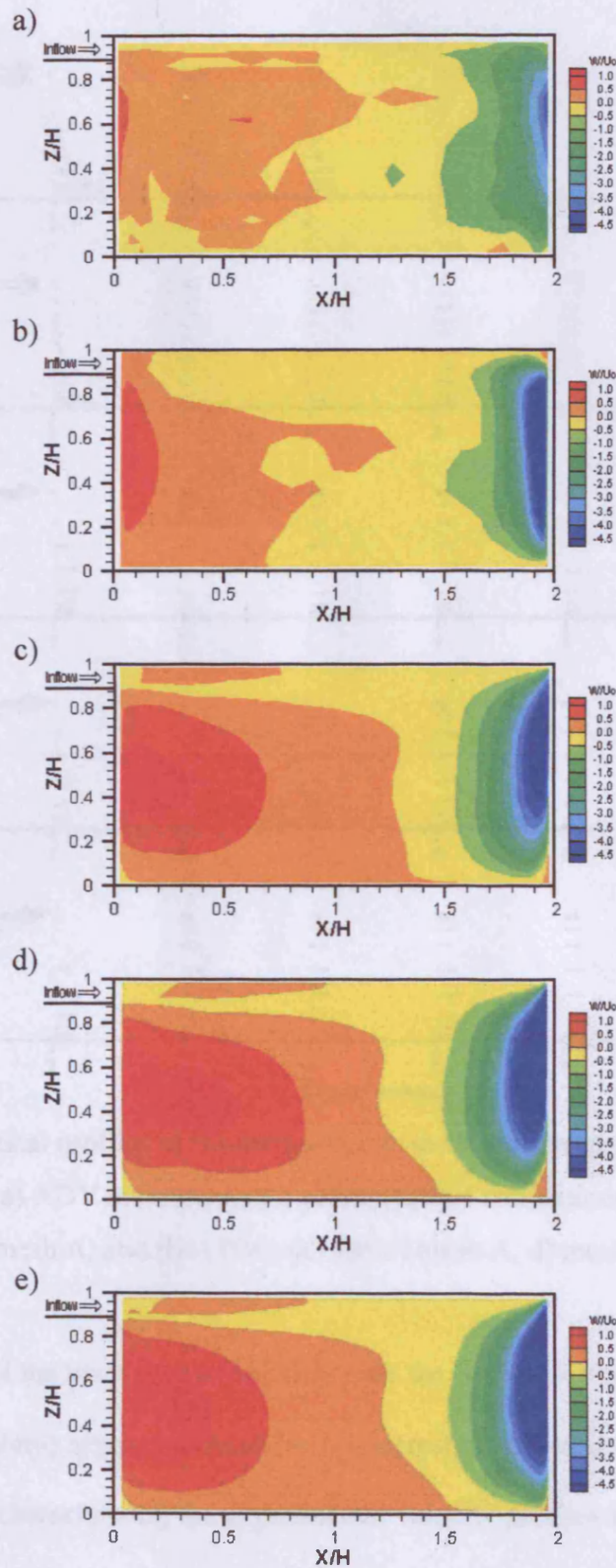
Figure 8.10 Contour plot of mean vertical velocity in Compartment 1 for setup OS-C obtained for: a) ADV measurements; and numerical simulations using: b) the DAEV approach for mesh A; and the LB model for: c) mesh A; d) mesh B; and e) mesh C
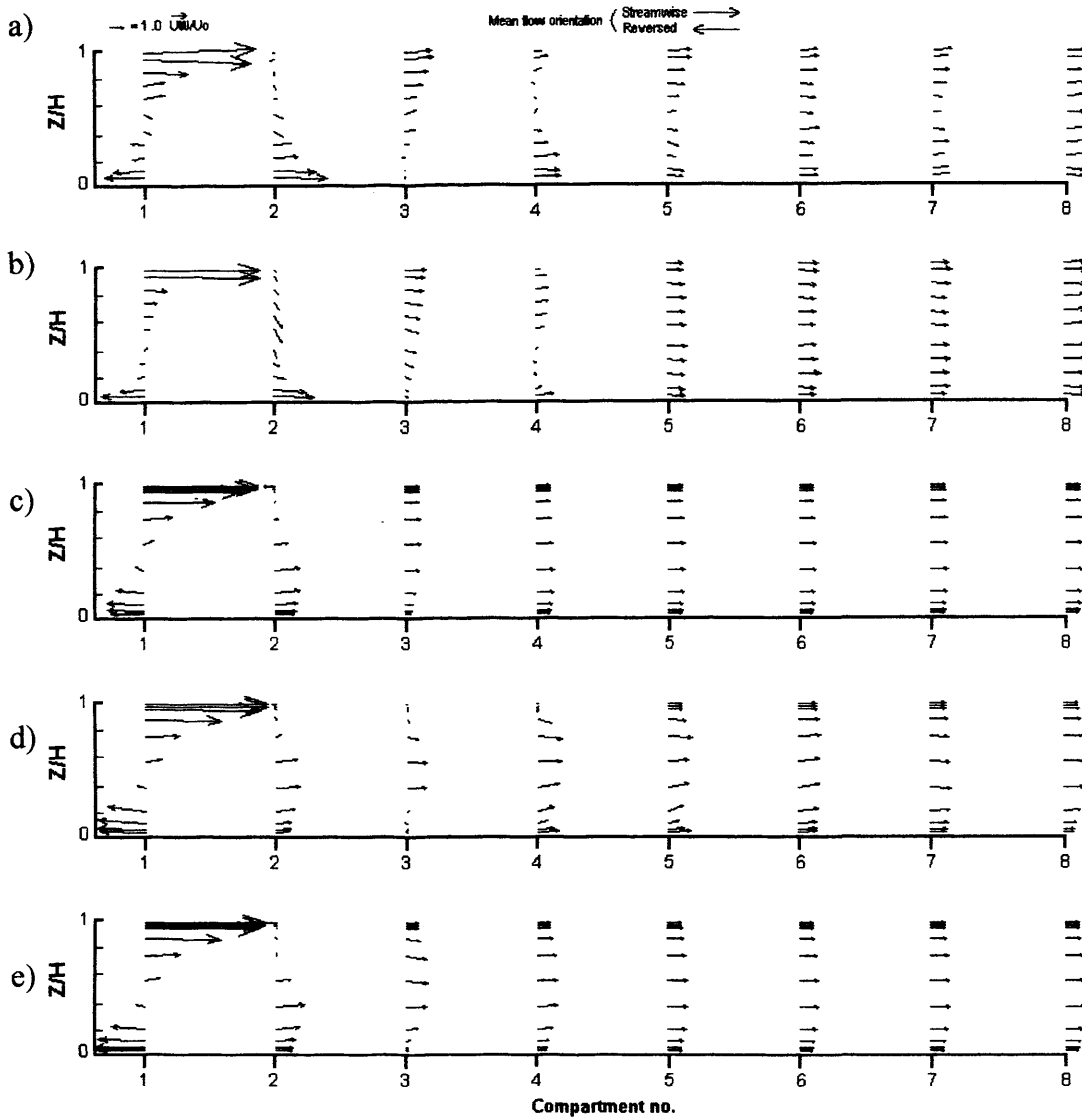
Figure 8.11 Vertical profiles of resultant velocity in Compartments 1 to 8 for setup OS-C, obtained for: a) ADV measurements; and numerical simulations using: b) the DAEV approach for mesh A; and the LB model for: c) mesh A; d) mesh B; and e) mesh C

The magnitude of the main streamwise flow near the bed of Compartment 2 (i.e. for z/H < 0.2 approximately) appears to have been underestimated when using the LB model. Furthermore, in characterising the experimental velocity profiles in section 6.2.1 it was found that the magnitude of the velocities measured in this region was of the order of 400% of U_0, while in the corresponding numerical model prediction obtained using the LB model this parameter was not higher than 200% of U_0. This analysis indicated that

179

the use of the LB model caused an underestimation of the extension of the 3-D flow in the tank.

These underestimated numerical model predictions may have been caused by an overestimation of the eddy viscosity values calculated from the numerical model using the LB model. The reason for this underestimation was thought to be due to the eddy viscosity consisting of the only turbulence parameter being included in the momentum equations and, thus, having an influence on the predicted results for the mean velocity field [see Equation (4.6)].

In order to illustrate this hypothesis, the corresponding numerical model results obtained for the distribution of the effective viscosity in various cross-sections of the tank simulated using the LB model and mesh A are shown in Figure 8.12. In this figure it can be seen that the predicted values for the effective viscosity parameter were consistently of the order of 100mm^2/s in the cross-sections shown. Such a magnitude was two orders higher than the value of the kinematic viscosity (i.e. $v_l \approx$ 1.0mm^2/s) and around one order of magnitude higher than the calculated depth-averaged eddy viscosity value in some regions, as used in the numerical model simulations with the DAEV approach. The near-bed and near-surface cross-sections in the tank were situated 30mm away from the corresponding boundary, or around z/H $\approx$ 0.03 and z/H $\approx$ 0.97 respectively. It is worth mentioning that even for these regions, where generally the eddy viscosity tended to be considerably lower than around the mid-depth in open-channel flows (see section 7.3.2), the predicted values for this parameter were consistently one order of magnitude higher than the depth-averaged value of v_t.
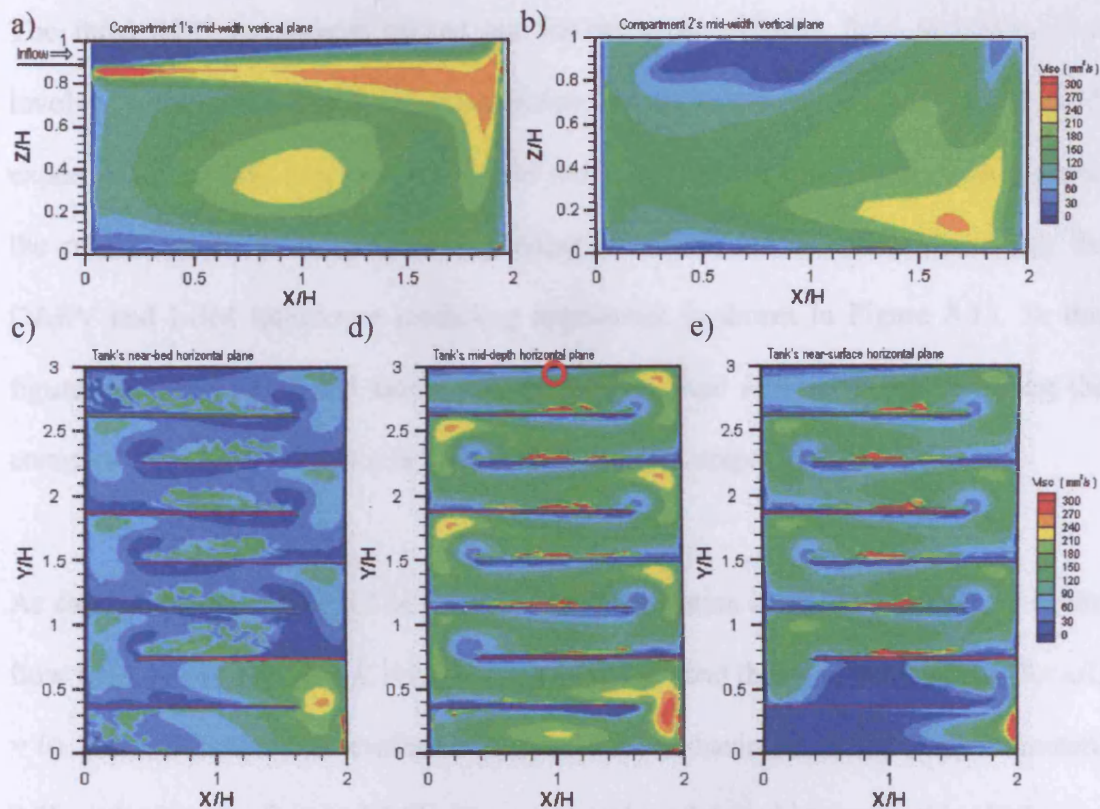
Figure 8.12 Numerical model prediction for the effective viscosity distribution in various regions for setup OS-C, illustrating: a) Compartment 1 at mid-width in the vertical plane; b) Compartment 2 at mid-width in the vertical plane; c) near-bed horizontal plane; d) mid-depth horizontal plane; and e) near-surface horizontal plane

Therefore, this analysis indicated that the use of the LB model in the 3-D hydrodynamic simulations carried out for setup OS-C predicted unduly high levels of the eddy viscosity, which may have compromised the corresponding numerical model predictions for the mean velocity field in the simulated tank. The reason for such an overestimation was thought to be due to insufficient mesh refinement near the tank solid boundaries, which may have lead to inaccurate predictions being made for the turbulence parameters using the LB model. This effect has been investigated further and the results obtained are discussed later in this section.

The third ADV assessment carried out for the mean velocity field in setup OS-C involved a mid-depth horizontal cross-section located in the region of 2-D flow in the experimentation tank (see section 6.2.1 for Assessment OS-A3). A comparison between the measured results and the corresponding numerical model predictions using the DAEV and LBM turbulence modelling approaches is shown in Figure 8.13. In this figure the longitudinal and lateral coordinate axes were normalised by including the compartment width L = 364.5mm, giving X/L and Y/L respectively.

As can be seen in Figure 8.13a, a horizontal recirculation zone (HRZ) occurred in the flow field in Compartment 8, with flow separation around the tip of Baffle 7 (i.e. for x/L = 0). This HRZ was characterised in section 6.2.1 as having a width of approximately 0.5L and a length of around 1.6L. The numerical model predictions for this HRZ were generally underestimated in comparison with the measured results, as shown in Table 8.5. A comparison between the measured and the corresponding numerically predicted results for the width and length of the HRZ indicated that the best estimates were obtained with the use of the LB model and mesh B, followed by the DAEV approach using mesh A.

Table 8.5 Numerical model and experimental dimensions of a horizontal recirculation zone for the region of the 2-D flow in setup OS-C

HRZ Dimension	Measured	DAEV mesh A	LBM mesh A	LBM mesh B	LBM mesh C
Width	0.5L	0.4L	0.3L	0.4L	0.4L
Length	1.6L	0.9L	0.7L	1.0L	0.8L
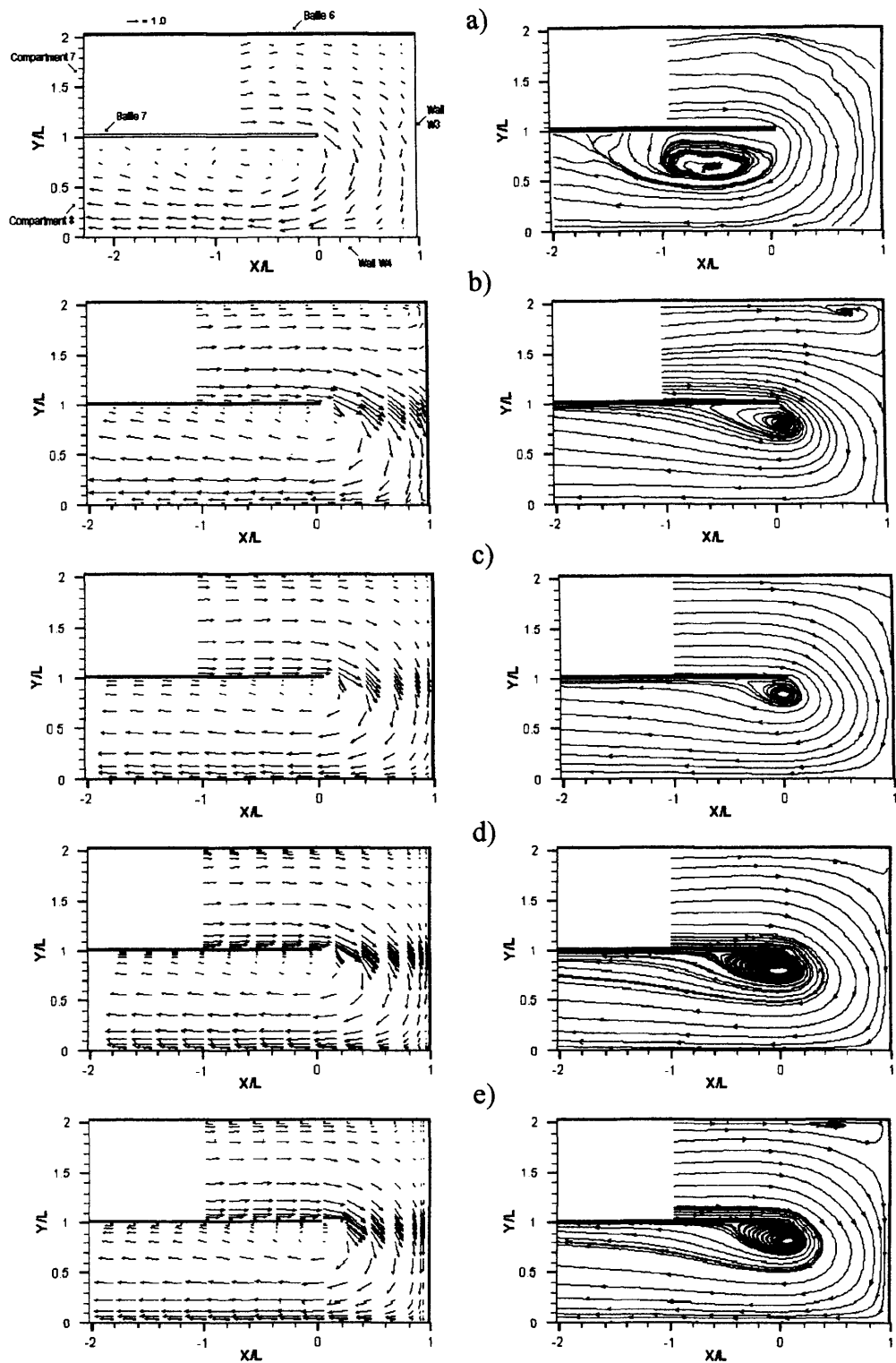
Figure 8.13 Mean velocity field and respective streamtrace plot for the 180° bend between Compartments 7 and 8 for setup OS-C, illustrating: a) ADV measurements; and numerical predictions using: b) the DAEV approach for mesh A; and the LB model for: c) mesh A; d) mesh B; and e) mesh C

The underestimation observed for the predicted HRZ size when using the LBM approach was probably due to an overestimation of the eddy viscosity values in the simulated flow field. In order to investigate this hypothesis, a comparison was carried out involving the numerically calculated near-wall distributions of the turbulent kinetic energy (k) and the dissipation rate (ε), for the mesh configurations used in the simulations for setup OS-C. The respective numerical model predictions were evaluated for the region $x/H = 1.0$, $z/H = 0.5$, $2.9 < y/H < 3.0$, which corresponded to a location at the centre of Compartment 8, at mid-depth and near wall W4, as indicated by the red circle in Figure 8.12d. The results obtained from this analysis are illustrated in Figure 8.14, where the y axis indicates the normal distance to the wall.
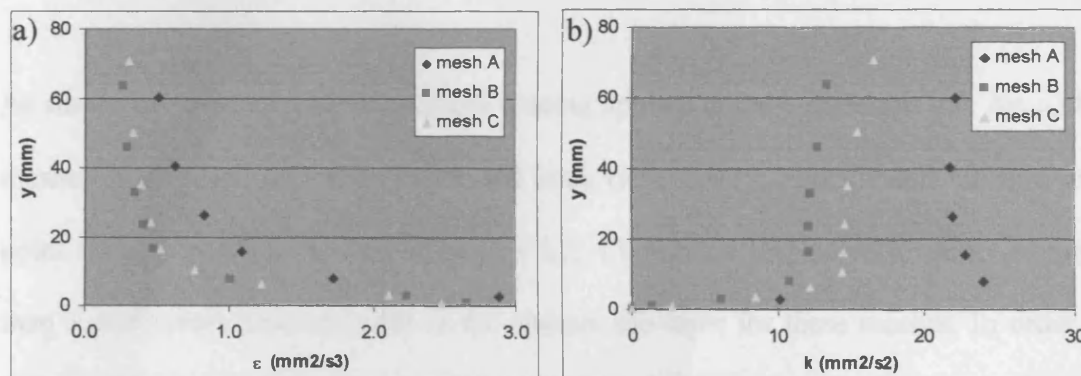
Figure 8.14 Near wall distributions of turbulence parameters obtained using the mesh configurations for setup OS-C, illustrating: a) ε profile; and b) k profile

Unfortunately, no measured data was available for comparison with the results of Figure 8.14. Nonetheless, Figure 8.14a shows that the calculated values for the ε distribution for mesh A were generally higher than the respective results for meshes B and C, and that the results for meshes B and C were similar. Thus, the results shown in Figure 8.14a suggested that the ε profile was not affected by the grid spacing halving applied to

Δy_{min} from mesh C to mesh B, which suggested that a mesh independent solution was obtained for the ε distribution.

On the other hand, the k distribution calculated by the numerical model for meshes A, B and C was affected by the corresponding mesh refinement. As can be seen from Figure 8.14b, the trend for the k values followed that of the decrease of Δy_{min}, indicating that the numerical model solution for the k field may not have become mesh independent in this analysis. As a consequence, unduly high k values may have been predicted by the numerical model using the LB model for these mesh configurations and, hence, the advective effects may have been depleted due to unduly high turbulent diffusion levels being predicted by the numerical model.

As shown in Table 8.4, the finest mesh spacing applied in the y direction (i.e. Δy_{min}) for meshes A, B and C was 5mm, 1mm and 2mm respectively. This yielded the first grid point for each mesh to be located at $y^+ = 3.2$, 1.0 and 1.4 respectively, while no more than 3 grid points were included in the viscous sub-layer for these meshes. In order to improve the numerical model predictions, further refinement of the computational mesh would have been required, followed by an assessment of the mesh independence of the solution for the mean flow parameters, as well for the turbulence quantities. However, the 3-D numerical model simulations for such a refined mesh would have demanded an impracticably long computational time, considering the present-day processing power of desktop computers. For instance, it has been estimated that the computational time required for a converged hydrodynamic solution for setup OS-C, where a refined mesh having twice the number of grid cells of mesh B would have been used, would have

been of approximately 15 days on a Pentium IV 2.4GHz computer. In addition, it is worth mentioning that the need for such a high number of grid cells is due to two main factors: i) the use of a low Reynolds number k-ε model, which requires solving the governing equations for the viscous sub-layer, as well as for the remainder of the near-wall region and beyond; and ii) the presence and number of baffles in the contact tank, which tends to increase the area of flow in contact with solid boundaries.

In the following section the representativeness of the discrepancies observed for the hydrodynamic results was analysed in terms of their effects on the numerical model predictions for the solute transport processes for setup OS-C.

8.3.1.2 Solute transport results

In this section the 3-D numerical model predictions for the solute transport processes for setup OS-C of the prototype tank were verified against the corresponding tracer experimentation results. The solute transport simulations were carried out using the steady-state 3-D hydrodynamic solution for each setup of the tank and the initial and boundary conditions used were described in section 4.3.3.

The duration of the simulated tracer injection was 5s, while the value of the average tracer concentration in the tank was $C_0 = 7.0mg/l$. Qualitative and semi-quantitative analyses were carried out with the normalised results, which included the retention time distribution (RTD) curves, accumulated tracer mass (F) curves and hydraulic efficiency indicators (HEI) of the simulated prototype tank configuration.

The RTD and F curves predicted by the numerical model for setup OS-C using the DAEV and LBM approaches were compared with the corresponding measured curves, as shown in Figures 8.15a and 8.15b respectively. These curves have been obtained for a turbulent Schmidt number value of Sch = 1.0.
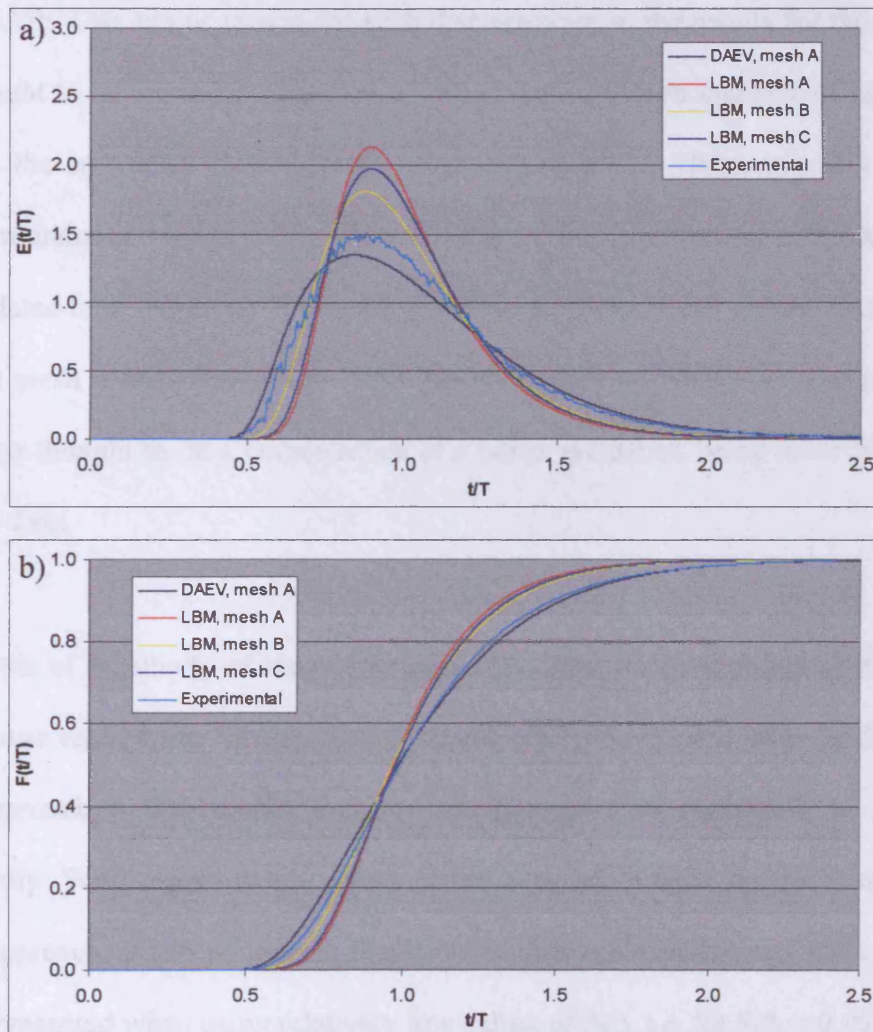
Figure 8.15 Numerical model and experimental tracer curves obtained for setup OS-C with Sch = 1.0, illustrating: a) RTD curves; and b) F curves

By comparing the RTD curves in Figure 8.15a it can be seen that the curve associated with the DAEV approach was in closer agreement with the experimental data than the

respective LBM results. The relatively narrow spread and higher peak concentration level of the latter curves indicated that lower levels of short-circuiting and mixing were predicted for setup OS-C using the hydrodynamic results for the LBM approach, which was not consistent with the experimental results. Likewise, the discrepancy between the results for the LBM approach for the F curve and the corresponding data can be seen in Figure 8.15b. One major reason for such discrepancies in the results for the LB model was thought to be an underestimation of the advective effects and size of recirculation zones in the respective flow patterns, as discussed above. Ultimately this may have caused an undue reduction in the volume occupied by flow reversal and dead zones in the simulated tank, affecting the mixing levels in the flow. It can also be seen in Figure 8.15 that mesh refinement overall had a positive effect on the RTD curve predictions, which was thought to be a consequence of a better prediction being made for the eddy viscosity field.

An analysis of sensitivity of the estimated RTD curves to the variation of the Schmidt number was carried out for the hydrodynamic results associated with the DAEV and LBM approaches. The results obtained are illustrated in Figures 8.16a and 8.16b respectively. With regard to the effect of the Schmidt number on the results for the DAEV approach, it can be seen in Figure 8.16a that the experimental RTD curve was better represented when using relatively low values of Sch, i.e. for Sch = 0.10 and Sch = 0.20. For the results associated with the LB model a 20-fold increase of the Schmidt number lowered the predicted peak concentration level, relative to the corresponding curve for Sch = 1.0. However, this increase did not seem to have a strong influence on the overall curve spreading, as can be seen in Figure 8.16b.
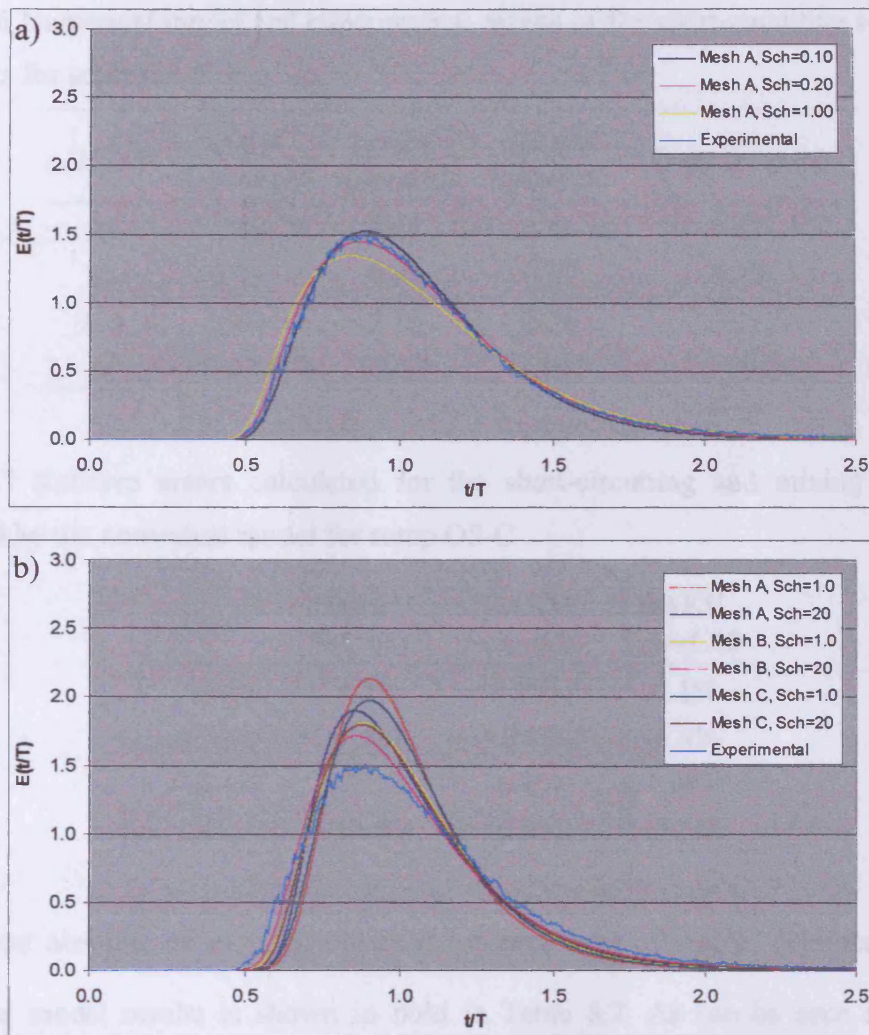
Figure 8.16 Effect of the Schmidt number on the RTD curves predicted for setup OS-C

using: a) the DAEV approach; and b) the LBM approach

An analysis of the numerical model predictions using the DAEV approach for the levels of short-circuiting and mixing for setup OS-C was carried out, in order to further evaluate the effect of the Schmidt number on the estimated solute transport results. The results calculated for the short-circuiting indicators θ_i and θ_{10}, and the mixing indicators Mo and σ^2, are presented with the corresponding experimental results in Table 8.6, while the respective relative errors (RE) are shown in Table 8.7.

Table 8.6 Numerical model and experimental results of the short-circuiting and mixing indicators for setup OS-C

HEI	DAEV Sch=0.10	DAEV Sch=0.20	DAEV Sch=1.00	Experimental
θ_i	0.49	0.47	0.46	0.47
θ_{10}	0.71	0.69	0.67	0.70
Mo	2.04	2.10	2.26	2.12
σ^2	0.079	0.089	0.107	0.095

Table 8.7 Relative errors calculated for the short-circuiting and mixing indicators predicted by the numerical model for setup OS-C

Error	DAEV Sch=0.10	DAEV Sch=0.20	DAEV Sch=1.00
$RE\text{-}\theta_i$	4.3%	**0.0%**	-2.1%
$RE\text{-}\theta_{10}$	**1.4%**	-1.4%	-4.3%
$RE\text{-}Mo$	-3.8%	**-0.9%**	6.6%
$RE\text{-}\sigma^2$	-16.8%	**-6.3%**	12.6%

The lowest absolute error value obtained for each HEI parameter obtained from the numerical model results is shown in bold in Table 8.7. As can be seen from these results, the use of Sch = 0.20 in the solute transport numerical model simulations for setup OS-C overall generated the lowest errors for the HEI parameters. This finding indicated that the corresponding results were the best representation of the experimental data, for the Sch values tested in this analysis. Although such a value of the Schmidt number could be regarded as unnaturally low, the technique of applying a variation to this parameter to encourage an adjustment in the numerically predicted solute transport results is a useful means to counteract the influence of an inaccurately predicted eddy viscosity field, as shown by Shiono et al. (2003).

In order to investigate further the ability of the numerical model to predict the hydrodynamic and solute transport processes in contact tanks with 3-D flow, an analysis was undertaken for the results obtained for setup MS4-C of the experimentation tank, as discussed below.

8.3.2 Setup MS4-C

This configuration of the experimentation tank consisted of 6 compartments and had similar inlet and outlet sections to setup OS-C. As can be seen in Figure 3.8, for this setup Compartments 1 to 5 were orientated transversally in relation to the main inflow direction, whilst Compartment 6 was aligned longitudinally.

A non-uniform mesh configuration was constructed for the numerical model simulations for setup MS4-C, consisting of 220,584 cells and with 101, 84 and 26 cells in the x, y and z directions respectively. The finest mesh spacing used was 5.0mm in all directions, while the coarsest mesh spacing corresponded to 50mm for the horizontal directions and 100mm for the vertical direction. A schematic representation of the computational mesh used is shown in Figure 8.17.

8.3.2.1 Hydrodynamic results

In a similar manner to setup OS-C, the hydrodynamic simulations for setup MS4-C were carried out using two turbulence modelling approaches, namely the depth-averaged eddy viscosity (i.e. DAEV) approach and the low Reynolds number k-ε model

of Lam and Bremhorst (i.e. LBM). The LB model calculations were made with C_μ as a variable parameter (see section 5.3.2). The flow rate of Q = 3.7l/s was used as the inlet boundary condition for the hydrodynamic module simulations, while a turbulence level of 1% was assumed for the inflow (see section 4.2.3).
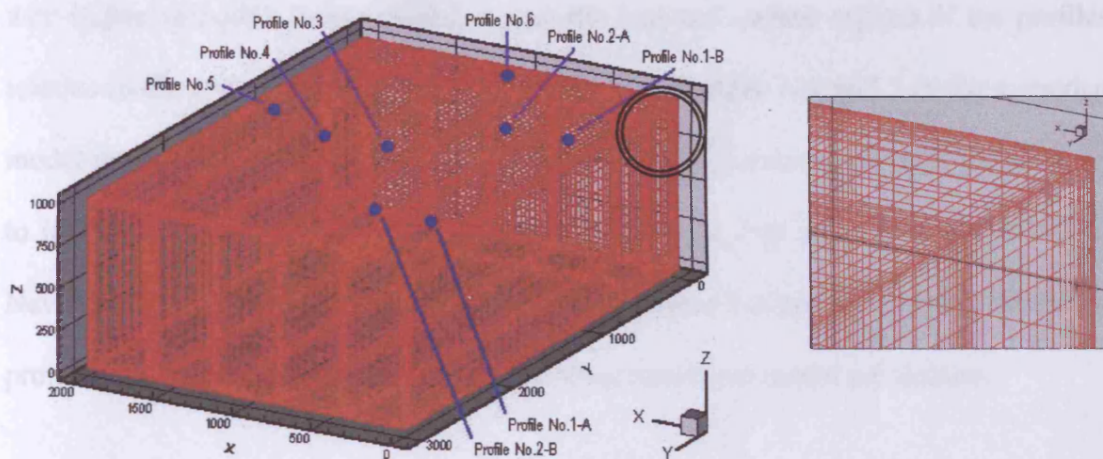
Figure 8.17 Illustration of non-uniform computational mesh used in the numerical simulations for setup MS4-C of the prototype tank

The hydrodynamic data available for the verification of the numerical model results for this setup consisted of results from the ADV measurements of the mean resultant velocities along the vertical direction in the compartments. A characterisation of these results was made in section 6.2.2.

In Figure 8.18 the measured data is illustrated, together with the corresponding numerical model predictions obtained using the DAEV and LBM approaches. The mean resultant velocity was calculated using the streamwise and vertical velocity components for each compartment, and the location of the assessed profiles has been indicated in Figure 8.17.

192

A comparison of the measured results shown in Figure 8.18a with their numerical counterparts in Figures 8.18b and 8.18c indicated that when using the LBM approach the numerical model generated a better prediction of the velocity distribution in profiles 2-A to 6, than in comparison with the use of the DAEV approach. The respective results obtained using the DAEV approach showed a higher non-uniformity over the depth, with higher velocities being predicted near the bed and surface regions of the profiles, relative to the corresponding mid-depth region. For profiles 1-A and 1-B the numerical model predictions were not accurate representations of the measured data, possibly due to insufficient mesh refinement in a region of complex 3-D flows (see section 6.2.2). Nevertheless, the upward velocities measured in profile 1-A and the streamwise flow in profile 1-B generally matched the corresponding numerical model predictions.
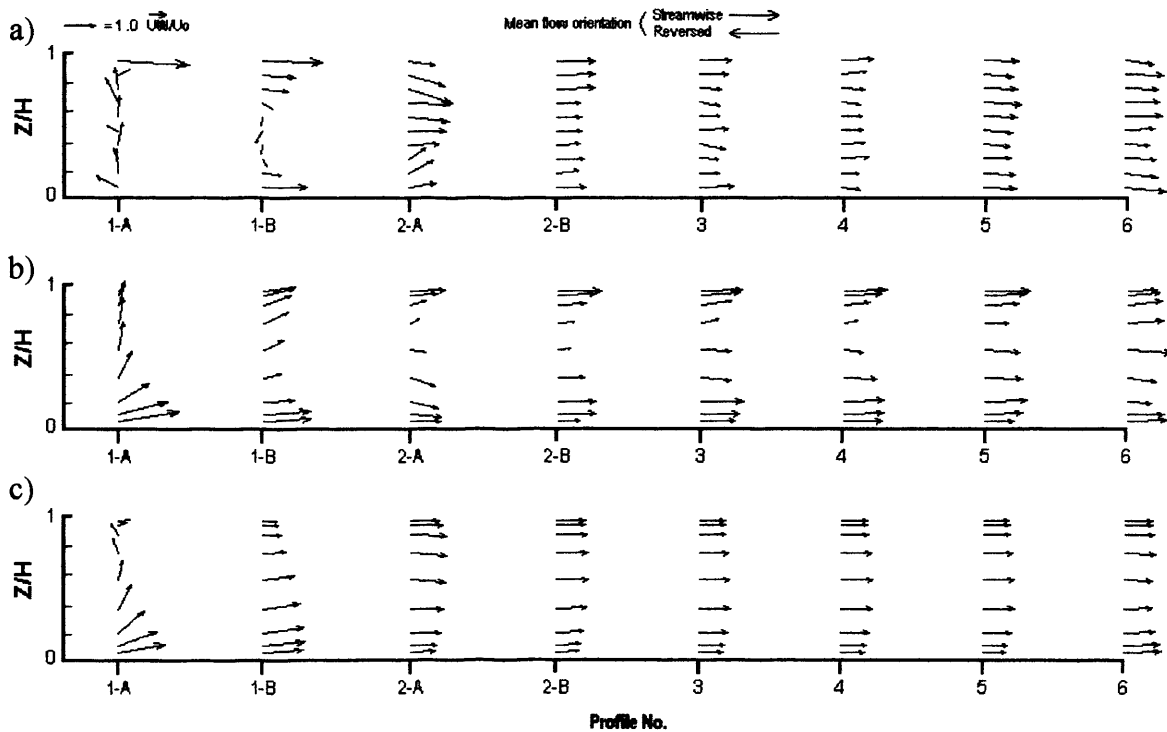
Figure 8.18 Vertical profiles of mean resultant velocity for setup MS4-C, obtained from: a) ADV measurements; b) numerical simulations using the DAEV approach; and c) numerical simulations using the LB model

The numerical model results obtained using each of the turbulence modelling approaches were compared in terms of the predicted size of a horizontal recirculation zone (HRZ) for setup MS4-C. The predicted streamtraces for the mean velocity field obtained in the 90° bend between Compartments 5 and 6 using the DAEV approach are shown in Figure 8.19a, whereas Figure 8.19b illustrates the corresponding prediction for the use of the LB model.
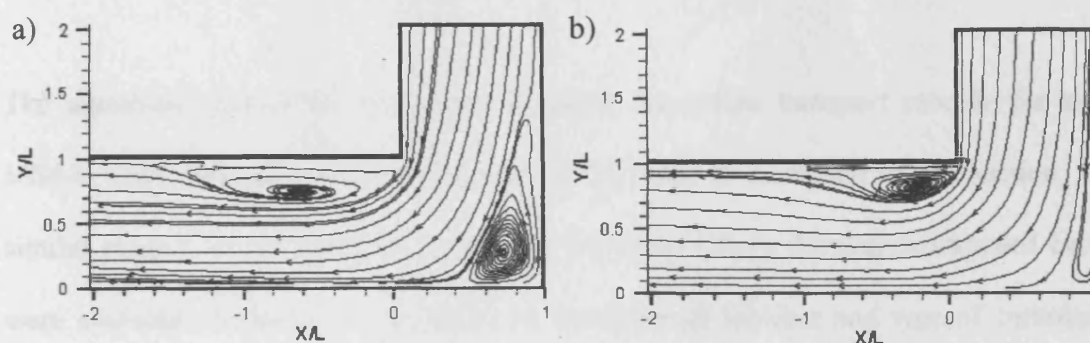
Figure 8.19 Streamtrace plot of the numerical model predictions for a 90° bend in setup MS4-C, illustrating the results for: a) DAEV approach; and b) LB model

The longitudinal and lateral coordinate axes in Figure 8.19 have been normalised by including the compartment width, giving X/L and Y/L respectively. As can be seen in Figure 8.19a, when using the DAEV approach the numerical model predicted the HRZ to be approximately 1.6L long and 0.4L wide. On the other hand, with the use of the LB model the predicted dimensions of the HRZ were 1.0L and 0.3L respectively, which were around 40% and 25% smaller than the DAEV predicted values. A comparison between Figures 8.19a and 8.19b also indicated that the results for the DAEV approach showed a larger HRZ for the region of x/L > 0.5 and y/L < 0.5 approximately. Such an effect of the type of turbulence modelling approach on the HRZ size corresponded to the trend verified for setup OS-C for the use of mesh A (see Figure 8.13).

Therefore, this analysis suggested that the region occupied by recirculation zones in the flow field predicted for setup MS4-C using the LB model is smaller than for the corresponding predictions for the DAEV approach. In the following section the influence of this discrepancy on the predicted levels of short-circuiting and mixing in the tank are assessed and discussed.

8.3.2.2 Solute transport results

The numerical model results calculated using the solute transport module for setup MS4-C were compared with the corresponding data, as discussed in this section. In a similar manner to the analysis carried out for setup OS-C, the results included herein were evaluated in terms of the effect of the Schmidt number and type of turbulence modelling approach on the predicted levels of short-circuiting and mixing in the tank.

The RTD and F curves obtained experimentally and predicted using the numerical model for setup MS4-C are shown in Figure 8.20a and 8.20b respectively, whilst the respective values of HEI parameters are presented in Table 8.8.

As can be seen in Figure 8.20a, the RTD curve associated with the LBM approach was not in good agreement with the experimental data for setup MS4-C. In a similar manner as to the corresponding results for setup OS-C, the aspect of the numerical curve indicated that the predicted levels of short-circuiting and mixing associated with the LBM approach were unduly low. This fact may be explained by the tendency shown by

the respective numerical model setup to underestimate the size of flow reversal and dead zones in the tank as predicted by the 3-D hydrodynamic simulations.
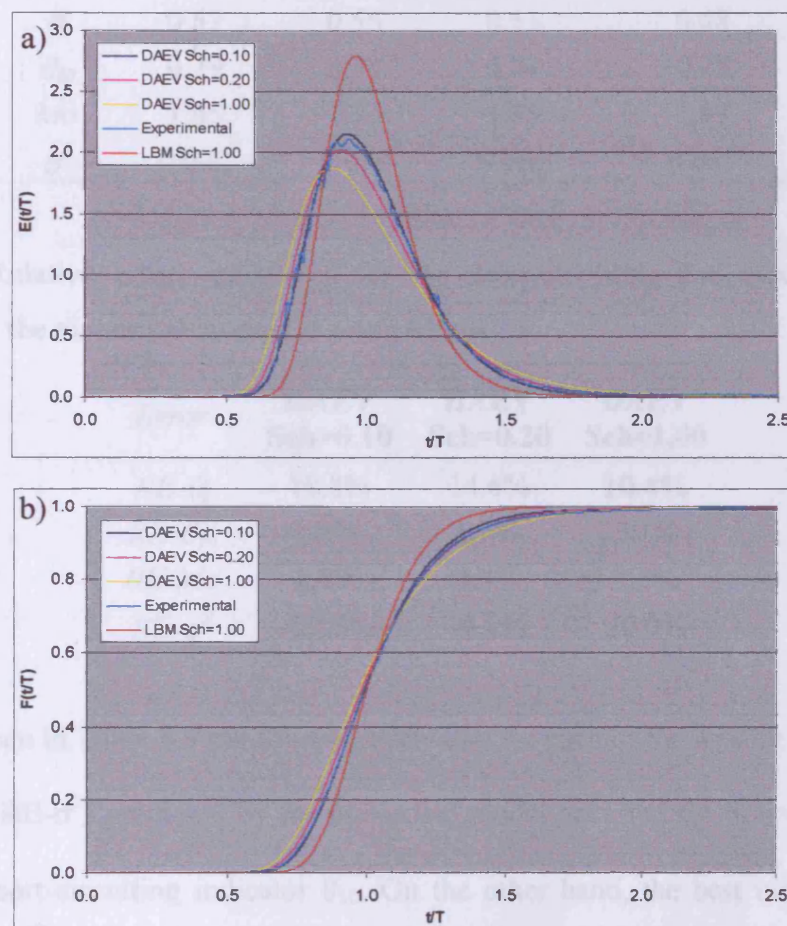
Figure 8.20 Numerical model and experimental tracer curves obtained for setup MS4-C, illustrating: a) RTD curves; and b) F curves

On the other hand, good agreement with the experimental data can be seen in Figure 8.20 between the RTD and F curves associated with the DAEV approach, particularly for the curves for Sch = 0.10 and Sch = 0.20. The effect of the Schmidt number on the predicted levels of short-circuiting and mixing for setup MS4-C using the DAEV approach was evaluated further, based on the results obtained for the HEI parameters and respective errors relative to the experimental results, as shown in Table 8.9.

196

Table 8.8 Numerical model and experimental results of the short-circuiting and mixing indicators for setup MS4-C

HEI	DAEV Sch=0.10	DAEV Sch=0.20	DAEV Sch=1.00	Experimental
θ_i	0.57	0.55	0.53	0.48
θ_{10}	0.79	0.77	0.74	0.78
Mo	1.65	1.73	1.85	1.69
σ^2	0.040	0.050	0.066	0.055

Table 8.9 Relative errors calculated for the short-circuiting and mixing indicators predicted by the numerical model for setup MS4-C

Error	DAEV Sch=0.10	DAEV Sch=0.20	DAEV Sch=1.00
RE-θ_i	18.8%	14.6%	10.4%
RE-θ_{10}	1.3%	1.3%	5.1%
RE-Mo	2.4%	2.4%	9.5%
RE-σ^2	-27.3%	-9.1%	20.0%

As can be seen in Table 8.9 the lowest error value for each of the mixing indicators (i.e. RE-Mo and RE-σ^2) predicted by the numerical model occurred for Sch = 0.20, as well as for the short-circuiting indicator θ_{10}. On the other hand, the best numerical model predictions for θ_i occurred for Sch = 0.10, although the corresponding result for Sch = 0.20 showed a similar order of magnitude. Further reduction of Sch would have caused higher discrepancies for the predicted short-circuiting and mixing levels, as suggested by the trend in the results presented in Table 8.8. Therefore, this analysis indicated that the best estimate of the tracer experiments results for setup MS4-C occurred for the Schmidt number value of 0.20, in a similar manner to the results for setup OS-C.

Summary

In this Chapter the numerical model application to the modelling of chlorine contact tanks (CCT) was evaluated for units with 2-D and 3-D flows. The ability of the 2-D numerical model to predict accurately measured results was evaluated, where two turbulence modelling approaches were tested. It was found that the use of a depth-averaged eddy viscosity approach (DAEV) caused an overestimation of the size predicted for a horizontal recirculation zone, which was linked in the analysis to an overestimation of the corresponding mixing levels predicted for the simulated tank. On the other hand, when using the low Reynolds number k-ε model of Lam and Bremhorst (i.e. the LB model) the 2-D numerical model predictions gave good agreement with the corresponding hydrodynamic and solute transport results.

In the analysis carried out for the 3-D flow results it was found that the use of the LB model caused an underestimation of the advective effects on the mean velocity field, as well as of the size of a horizontal recirculation zone, measured in the prototype tank. There was an indication that such phenomena was caused by an overestimation of the eddy viscosity values. As a consequence, the levels of short-circuiting and mixing in the simulated setups were greatly underestimated when the hydrodynamic results associated with the LB model were used in the solute transport simulations. On the other hand, the use of the DAEV approach in the hydrodynamic module, together with manipulation of the value of the Schmidt number in the solute transport simulations, provided very good numerical model predictions for the tracer experimentation results obtained for various configurations in the prototype tank with complex 3-D flow.

Chapter 9

Conclusions and Recommendations

for Further Research

9.1. CONCLUSIONS

A review of the main results obtained and the conclusions derived from this study are presented below.

9.1.1 Physical experimentation

The physical experimentation carried out in this study involved the measurement of mean velocities by acoustic Doppler velocimetry (ADV) and assessments of the hydraulic efficiency of the Prototype Tank (PT) using fluorescent tracer techniques.

A number of design setups of the PT have been assessed experimentally, for which the levels of dispersion were identified as ranging from intermediate to high. The ADV assessments provided data for the validation of the hydrodynamic predictions made by numerical models, while the tracer tests results can be used to validate numerical predictions of solute transport processes. The main outcomes of the physical experimentation carried out are outlined below.

From the mean velocity measurements carried out in the original setup of the PT, i.e. setup OS-C, regions with recirculating flow structures in both the vertical and horizontal planes were characterised. The progression of the three-dimensional (3-D) effects in the mean flow through the tank was assessed based on the vertical distributions of the resultant velocity measured in compartments. An analysis of these results indicated that the deleterious influence of the inlet configuration to the flow pattern in the tank was

felt at least until Compartment 5 of a total of 8 compartments for the original setup, which corresponded to the condition observed for a similar prototype contact tank in a previous study.

Mean velocity measurements were also carried out for a modified configuration of the PT, i.e. setup MS4-C, which comprised a transversal baffling arrangement for the first 5 of a total of 6 compartments. An analysis of the corresponding ADV results indicated that 3-D flow occurred mainly in Compartments 1 and 2 of this setup. For the remainder of the compartments there was an indication that the flow had a 2-D horizontal character. This fact suggested that the modification promoted to the type of baffling arrangement induced an improvement of the flow pattern for the tank, since the extension of the 3-D effects was lower than in the original configuration. This may have been a consequence of the deflection of the inflow jet by the baffle located opposite to the inlet section, and subsequently by the inlet wall. As a consequence of this, it is possible that the advective effects of the inflow jet were dampened mostly within Compartment 1 of this setup, which would then have contributed towards the homogenisation of the mean flow along the depth.

The hydraulic efficiency of setup MS4-C was assessed using tracer techniques. As expected from the analysis of the ADV results, the modification promoted to the type of baffling arrangement generated a higher hydraulic efficiency for the tank, with lower levels of short-circuiting and mixing occurring in the flow in comparison with the original setup. Such an improvement of the hydraulic efficiency was regarded as a consequence mainly of the reduction of the 3-D effects in this tank configuration.

9.1.2 Numerical model validation for benchmark flow problems

9.1.2.1 Hagen-Poiseuille flow

Numerical simulations of the Hagen-Poiseuille channel flow problem were carried out as part of the validation process of the core hydrodynamic module of the numerical model, where no turbulence modelling approach was used. The results thus obtained for the developing and fully-developed velocity distributions were compared with data from the literature and the analytical solution respectively.

A mesh independence study was performed with the numerical results for the fully-developed velocity profile, where mesh refinement was applied in the direction perpendicular to the main streamwise flow direction. Two error parameters were calculated between the predicted velocity distributions and the corresponding analytical solution, namely: i) the relative discretisation error (RDE), which was based on the Richardson extrapolation method; and ii) a modified RDE that was not affected by the relatively low velocities calculated for the vicinity of the channel walls.

A trend analysis carried out for the variation of the error parameters indicated that a monotonic convergence pattern occurred with mesh refinement. The start of the asymptotic range of the error curves indicated the mesh independent solution, for which the maximum error value involved in the predicted fully-developed velocity profile was of the order of 1%. It was pointed out that such an error magnitude corresponded to the uncertainty typically involved in mean velocity measurements by ADV. Furthermore,

the velocity distributions calculated for the developing Hagen-Poiseuille flow in four locations along the channel were in good agreement with the corresponding data.

9.1.2.2 Turbulent open channel flow

The analysis undertaken for the validation of the numerical model for 2-D turbulent open channel flow involved two types of results. Firstly, numerical hydrodynamic simulations were carried out for a horizontal channel for the Reynolds number values of Re = 5,000 and 30,000. These numerical simulations were performed using the low Reynolds number k-ϵ model of Lam and Bremhorst, i.e. the LB model. The parameter C_μ was modelled using two distinct approaches, i.e. as a constant quantity where C_μ = 0.09, and as a variable quantity where C_μ was a function of the ratio between the turbulence production and the dissipation rate. The numerical predictions thus obtained for the fully-developed near wall distribution of the mean streamwise velocity, turbulent kinetic energy and dissipation rate were compared with the corresponding shape function that describe the variation of these quantities in the near wall region.

For the results associated with either value of the Reynolds number, a good agreement occurred between the predicted results and the corresponding shape functions with the use of the variable C_μ approach. On the other hand, for the constant C_μ approach there was an underestimation of the mean streamwise velocity values outside the viscous sublayer of the near wall region. This was probably caused by higher eddy viscosity values being calculated using the constant C_μ approach than with the variable C_μ approach, which in turn was associated to a lower dissipation rate being calculated for

the viscous sublayer and buffer zone using the former approach. This analysis suggested that the use of the LB model for the modelling of turbulence should be accompanied by adopting the variable C_μ approach in the numerical model simulations, since the value of this quantity can vary substantially within the viscous sublayer.

The second stage of the analysis of the numerical model predictions for turbulent open channel flows was undertaken for the 2-D vertical flow problem, for Re = 2,750, Re = 7,716 and Re = 68,860. The numerical hydrodynamic simulations were carried out using the LB model in conjunction with the variable C_μ approach. Comparisons of the numerical results were made against published data of a direct numerical simulation (DNS) study, laser Doppler anemometry (LDA) and numerical results external to this study obtained using the low Reynolds number k-ε model of Launder and Sharma, i.e. the LS model. The analysis of these results was undertaken for the normalised mean streamwise velocity, turbulent kinetic energy, dissipation rate and eddy viscosity parameters.

The validation analysis undertaken for the vertical profiles of these quantities indicated that the numerical model was able to accurately predict the depth-wise velocity and eddy viscosity distributions, independently of the flow regime. Furthermore, the comparisons carried out with the published results obtained using the LS model and the traditional constant C_μ approach indicated that the results of the present study were generally in closer agreement with the data. This analysis suggested that the use of the LB model with the variable C_μ approach was appropriate for the modelling of non-laminar open channel flows in both the horizontal and vertical directions.

9.1.3 Numerical model application to contact tanks

9.1.3.1 Two-dimensional hydrodynamic simulations

The 2-D hydrodynamic simulations of Contact Tanks (CT) were carried out using two turbulence modelling approaches, namely: i) a depth-averaged eddy viscosity (DAEV) approach; and ii) the low Reynolds number k-ε model of Lam and Bremhorst, i.e. the LB model. When using the LB model, the numerical simulations were performed with the parameter C_μ as a variable quantity, since this approach was found to provide a better representation of the near wall turbulent channel flow distributions than with the constant C_μ approach (see above).

The main outcomes of the hydrodynamic simulations were the steady-state mean velocity field and the effective viscosity distribution for the simulated CT configurations. The effective viscosity parameter included the kinematic viscosity of the fluid and the eddy viscosity calculated using the turbulence model.

The results obtained with the use of the LB model in the 2-D hydrodynamic simulations were in good agreement with the corresponding experimentation data, as evaluated from comparisons of the mean velocity field for a region of 2-D flow in a prototype CT. A satisfactory representation of a measured recirculating flow region was verified when using the LB model, whilst with the use of the DAEV approach the numerical model failed to predict the reattachment, thus overestimating the size, of the recirculation zone. Since the size of the recirculating and stagnant flow regions are generally associated to

the amount of mixing that takes place in a CT, it was anticipated that the tracer experimentation results would be better represented by the solute transport results associated to the use of the LB model, rather than for the DAEV approach.

9.1.3.2   Two-dimensional solute transport simulations

The 2-D solute transport simulations were carried out with the steady-state hydrodynamic results obtained for each turbulence modelling approach, i.e. the DAEV approach and the LB model, for a CT with 2-D flow.

Tracer experiments of the "black box" type were simulated where an instantaneous tracer injection was mimicked at the inlet and the mean tracer concentration with time was calculated for the outlet section of the simulated tank. As a result of this procedure the numerical model generated the retention time distribution (RTD) curve, accumulated tracer mass (F) curve and hydraulic efficiency indicators (HEI) for each simulation scenario. An analysis of sensibility of these results was carried out for the variation of the type of turbulence model and value of the turbulent Schmidt number (σ_t). The values of the Schmidt number tested were $\sigma_t = 0.75$, 1.00 and 1.25.

A good agreement occurred between the empirical data and the corresponding numerical model results associated with the use of the LB model, for the RTD and F curves, as well as for the HEI parameters. On the other hand, the results associated to the use of the DAEV approach showed that the short-circuiting and mixing levels in the tank were overestimated. This fact was probably a consequence of an overestimation of

the size of recirculation zones in the simulated tank as predicted by the numerical model using the DAEV approach, as reported above.

With regard to the effect of the Schmidt number on the solute transport results associated to the LB model, an analysis of the RTD curves showed that the measured peak tracer concentration level was better represented in the numerical model results obtained with $\sigma_t = 0.75$. On the other hand, an analysis of the relative errors of the numerical predictions for the HEI parameters showed that the best estimate for the short-circuiting indicator θ_{10} as well as the mixing indicator Mo, occurred for $\sigma_t = 1.00$, where the relative errors found were of the order of 0.1%.

The results of the 2-D numerical simulations carried out using the LB model were in good agreement with the corresponding experimental data, indicating the appropriateness of applying the low Reynolds number k-ε model of Lam and Bremhorst to simulate the hydrodynamics of Contact Tanks with 2-D flow. Relatively good estimates of the disinfection efficiency in the tank could be expected, should the solute transport results be used for such a purpose.

9.1.3.3   Three-dimensional hydrodynamic simulations

The 3-D numerical hydrodynamic simulations were performed in this study for two design setups of the experimentation tank, namely setups OS-C and MS4-C. Setup OS-C was the original setup of the prototype tank, which comprised 8 compartments longitudinally oriented in relation to the main streamwise inflow direction. On the other

hand, setup MS4-C had 6 compartments, the first 5 of which were transversally oriented in relation to the inflow. Both configurations had an open channel as the inlet device and a rectangular sharp-crested weir was located at the outlet section.

In a similar way to the 2-D simulations of contact tanks, the numerical simulations of these setups were performed using two turbulence modelling approaches, i.e. the DAEV approach and the LB model. The results thus obtained were compared with the ADV results obtained for the respective configurations.

A comparative analysis of the hydrodynamic results indicated the use of the DAEV approach in the numerical model was generally associated to a better reproduction of the measured velocity results for both tank configurations, in comparison with the corresponding results obtained with the LB model. The use of the LB model generally caused an underestimation of the mean resultant velocity along the main advective flow path in the tank, as well as of the size of a horizontally reversed flow structure. This fact was interpreted as being an underestimation of the advective effects in the flow field calculated with the LB model, probably as a consequence of an overestimated eddy viscosity field.

9.1.3.4 Three-dimensional solute transport simulations

The steady-state solution for the mean velocity and eddy viscosity fields calculated using the DAEV approach and the LB model were respectively used in the 3-D solute transport simulations for setups OS-C and MS4-C. These numerical simulations were

performed so as to mimic "black box" tracer experiments, generating the RTD and F

curves, as well as the HEI parameters for the simulated tank configurations. Variation of

the turbulent Schmidt number was promoted, where the values tested for this parameter

were Sch = 1.00, 0.20 and 0.10. The numerical predictions were compared with the

corresponding experimentation results for validation.

An analysis of the numerical results for Sch = 1.00 associated with each turbulence

modelling approach indicated that the results obtained for the DAEV approach were in

closer agreement with the data than the corresponding results for the LB model. For the

predicted results associated to the DAEV approach a good agreement was obtained for

complex 3-D flow patterns, in specific for relatively low Schmidt number values, i.e. for

Sch = 0.20 and Sch = 0.10. The errors calculated for the respective values of the short-

circuiting and mixing indicators were of the order of 1%, for the parameters θ_{10} and Mo.

9.2. RECOMMENDATIONS FOR FURTHER RESEARCH

The following recommendations are made for further research:

- Carry out turbulence measurements in the prototype tank using ADV, in order to
  provide data for validation analyses of numerical model predictions for turbulent
  parameters.

- Further investigate the observed tendency of the numerical model to underestimate the advective effects and the size of recirculating flow regions in the 3-D hydrodynamic simulations with the LB model.

- Extend the validation of the numerical model developed in this study for a wider range of flow patterns in contact tanks, using hydrodynamic as well as solute transport experimentation results for configurations with relatively high levels of short-circuiting and mixing.

- Carry out numerical hydrodynamic simulations using other types of higher order turbulence models for contact tanks with 3-D flow, on the prototype scale, as well as field scale, in order to further assess the conditions under which the application of specific types of models is appropriate to the modelling of these tanks.

- Extend the numerical model so as to include different types of advection-diffusion scheme, such as the QUICK scheme and other higher order schemes, in order to investigate the effect of each scheme on the numerical model predictions of the hydrodynamic and solute transport processes in contact tanks with a complex 3-D flow structure.

- Extend the numerical model so as to include different types of solution method for the systems of discretised equations, in order to investigate the effect of each method on the rate of convergence of the hydrodynamic simulations.

- Extend the mesh generator programme, as well as the numerical model to include the option of cylindrical coordinates, which would allow for the simulation of treatment units with a circular cross-section.

- Develop a user-friendly interface for the numerical model, in order to facilitate the input of simulation parameters, as well as the utilisation of the model by non-Fortran-proficient users.

- Modify the solute transport module so as to allow for the simulation of non-conservative solutes, in order to be allow for predictions of phenomena such as chlorine decay, inactivation of bacteria and formation of by-products of disinfection.

References

References

Abbott, M. B. and Basco, D. R. (1989). Computational Fluid Dynamics: an Introduction for Engineers. Longman Scientific and Technical, Essex, UK.

Adams, E. W. and Rodi, W. (1990). Modelling Flow and Mixing in Sedimentation Tanks. Journal of Hydraulic Engineering, ASCE, 116, 7, 895-913.

Balaras, E. and Benocci, C. (1994). Subgrid Scale Models in Finite Difference Simulations of Complex Wall Bounded Flows. Proceedings of the 74th AGARD Fluid Dynamics Symposium: Application of Direct and Large Eddy Simulation to Transition and Turbulence, Chania, Greece.

Batchelor, G. K. (1967). An Introduction to Fluid Dynamics. Cambridge University Press, Cambridge.

Beier, R. A., de Ris, J. and Baum, H. R. (1983). Accuracy of Finite-Difference Methods in Recirculating Flows. Numerical Heat Transfer, 6, 283-302.

Binnie, C., Kimber, M. and Smethurst, G. (2002). Basic Water Treatment. 3rd ed., Thomas Telford, London.

Biron, P., Roy, A. G. and Best, J. L. (1995). A Scheme for Resampling, Filtering and Subsampling Unevenly Spaced Laser Doppler Anemometer Data. Mathematical Geology, 27, 6, 731-748.

Biswas, G., Breuer, M. and Durst, F. (2004). Backward-Facing Step Flows for Various Expansion Ratios at Low and Moderate Reynolds Numbers. Journal of Fluids Engineering, ASME, 126, 3, 362-374.

Boyer, V. and Laurence, D. (2002). A Shape Function Approach for High- and Low-Reynolds Near-Wall Turbulence Models. International Journal for Numerical Methods in Fluids, 40, 241-251.

Braaten, M. E. and Patankar, S. V. (1989). A Block-Corrected Sub-Domain Solution Procedure for Recirculating Flow Calculations. Numerical Heat Transfer B, 15, 1-20.

BSI (2003). Wastewater Treatment Plants – Part 14: Disinfection. British Standard BS EN 12255-14. [WWW] <URL http://www.bsonline.bsi-global.com/server/index.jsp> [Accessed 27/07/04]

Celik, I. and Rodi. W. (1984). Simulation of Free-Surface Effects in Turbulent Channel Flows. Physicochemical Hydrodynamics, 5, 217-227.

Celik, I. and Zhang, W. (1995). Calculation of Numerical Uncertainty Using Richardson Extrapolation: Application to Some Simple Turbulent Flow Calculations. Journal of Fluids Engineering, ASME, 117, 439-445.

Chow, V. T. (1959). Open-Channel Hydraulics. McGraw-Hill, New York.

Cotton, M. A., Reedha, D. and Stansby, P. K. (2003). Open Channel Flow Computed Using a Low-Reynolds Number k-ε Turbulence Model. Proceedings of XXX IAHR Congress, Thessaloniki, Greece.

Danckwerts, P. V. (1953). Continuous Flow Systems. Distribution of Residence Times. Chemical Engineering Science, 2, 1, 1-13.

de Bruin, I. C. C. (2001). Direct and Large Eddy Simulation of the Spatial Turbulent Mixing Layer. Ph.D. Thesis, University of Twente, The Netherlands.

Deaner, D. G. (1973). Effect of Chlorine on Fluorescent Dyes. Journal of the Water Pollution Control Federation, 45, 3, 507-514.

Demuren, A. O. and Rodi, W. (1983). Side Discharges into Open Channels: Mathematical Model. Journal of Hydraulic Engineering, ASCE, 109, 12, 1707-1722.

Droste, R. L. (1997). Theory and Practice of Water and Wastewater Treatment. John Wiley & Sons, New York.

Elder, J. W. (1959). The Dispersion of Marked Fluid in Turbulent Shear Flow. Journal of Fluid Mechanics, 5, 4, 544-560.

Falconer, R. A. (1991). Review of Modelling Flow and Pollutant Transport Processes in Hydraulic Basins. Proceedings of 1st International Conference on Water Pollution: Modelling, Measuring and Prediction, Southampton, UK.

Falconer R. A. and Ismail A. I. B. M. (1997). Numerical Modelling of Tracer Transport in a Contact Tank. Environment International, 23, 6, 763-773.

Falconer, R. A. and Liu, S. Q. (1987). Mathematical Model Study of Plug Flow in a Chlorine Contact Tank. Journal of Water and Environmental Management, 1, 3, 3279-3290.

Falconer, R. A. and Liu, S. Q. (1988). Modelling Solute Transport Using QUICK Scheme. Journal of Environmental Engineering, ASCE, 114, 1, 3-20.

Falconer, R. A., Lin, B., Wu, Y. and Harris, E. L. (1999). DIVAST Model User Manual. Hydroenvironmental Research Centre, Cardiff University, UK.

Faure, J.-B., Buil, N. and Gay, B. (2004). 3-D Modeling of Unsteady Free-Surface Flow in Open Channel. Journal of Hydraulic Research, 42, 3, 263-272.

Finelli, C. M., Hart, D. D. and Fonseca, D. M. (1999). Evaluating the Spatial Resolution of an Acoustic Doppler Velocimeter and the Consequences for Measuring Near-Bed Flows. Limnology and Oceanography, 44, 7, 1793-1801.

Fischer, H. B. (1973). Longitudinal Dispersion and Turbulent Mixing in Open Channel Flow. Annual Review of Fluid Mechanics, 5, 59-78.

French, R. H. (1985). Open Channel Hydraulics. McGraw-Hill, Singapore.

Goring, D. G. and Nikora, V. I. (2002). Despiking Acoustic Doppler Velocimeter Data. Journal of Hydraulic Engineering, ASCE , 128, 1, 117-126.

Gray, N. F. (1999). Water Technology – an Introduction for Environmental Scientists and Engineers. Arnold, London.

Grayman, W. M., Deininger, R. A., Green, A., Boulos, P. F., Bowcock, R. W. and Godwin, C. C. (1996). Water Quality and Mixing Models for Tanks and Reservoirs. Journal of the American Water Works Association, 88, 7, 60-73.

Gyürék, L. L. and Finch, G. R. (1998). Modeling Water Treatment Chemical Disinfection Kinetics. Journal of Environmental Engineering, ASCE, 124, 9, 783-793.

Hannoun, I. A. and Boulos, P. F. (1997). Optimizing Distribution Storage Water Quality: a Hydrodynamic Approach. Applied Mathematical Modelling, 21, 495-502.

216

Hannoun, I. A., Boulos, P. F. and List, E. J. (1998). Using Hydraulic Modelling to Optimize Contact Time. Journal of the American Water Works Association, 90, 8, 77-87.

Hart, F. L. (1979a). Modifications for the Chlorine Contact Chamber. Journal of the New England Water Pollution Control Association, 13, 2, 135-151.

Hart, F. L. (1979b). Improved Hydraulic Performance of Chlorine Contact Chambers. Journal of the Water Pollution Control Federation, 51, 12, 2868-2875.

Hart, F. L. and Gupta, S. K. (1978). Hydraulic Analysis of Model Treatment Units, Journal of the Environmental Engineering Division, ASCE, 104, EE4, 785-798.

Hart, F. L. and Vogiatzis, Z. (1982). Performance of Modified Chlorine Contact Chamber. Journal of the Environmental Engineering Division, ASCE, 108, EE3, 549-561.

Hart, F.L., Allen, R., Dialesio, J. and Dzialo, J. (1975). Modifications Improve Chlorine Contact Chamber Performance. Water and Sewage Works, 122, 4, 73-75.

Hinze, J. O. (1975). Turbulence. 2nd ed., McGraw-Hill, New York.

Issa, R. I. (1985). Solution of the Implicitly Discretised Fluid Flow Equations by Operator-Splitting. Journal of Computational Physics, 62, 40-65.

Jang, D. S., Jetli, R. and Acharya, S. (1986). Comparison of the PISO, SIMPLER and SIMPLEC Algorithms for the Treatment of the Pressure-Velocity Coupling in Steady Flow Problems. Numerical Heat Transfer, 10, 209-228.

Johnson, P., Graham, N., Dawson, M. and Barker, J. (1998). Determining the Optimal Theoretical Residence Time Distribution for Chlorine Contact Tanks. Journal of Water Supply: Research and Technology – AQUA, 47, 5, 209-214.

Kawamura, S. (1991). Integrated Design of Water Treatment Facilities. John Wiley & Sons, New York.

Kelkar, K. M. and Patankar, S. V. (1989). Development of Generalized Block Correction Procedures for the Solution of Discretized Navier-Stokes Equations. Computer Physics Communications, 53, 329-336.

Kim, C.-K. and Lee, J.-S. (1994). A Three-Dimensional PC-Based Hydrodynamic Model Using an ADI Scheme. Coastal Engineering, 23, 271-287.

Kothandaraman, V., Southerland, H. L. and Evans, R. L. (1973). Performance Characteristics of Chlorine Contact Tanks. Journal of the Water Pollution Control Federation, 45, 4, 611-619.

Kraus, N. C., Lohrmann, A. and Cabrera, R. (1994). New Acoustic Meter for Measuring 3D Laboratory Flows. Journal of Hydraulic Engineering, ASCE,120, 3, 406-412.

Lai, Y. G., Weber, L. J. and Patel, V. C. (2003). Non-Hydrostatic Three-Dimensional Model for Hydraulic Flow Simulation, Part I: Formulation and Verification. Journal of Hydraulic Engineering, ASCE, 129, 3, 196-205.

Lam, C. K. G. and Bremhorst, K. (1981). A Modified Form of the k-ε Model for Predicting Wall Turbulence. Journal of Fluids Engineering, ASME, 103, 456-460.

Lam, K. and Banerjee, S. (1992). On the Condition of Streak Formation in a Bounded Turbulent Flow. Physics of Fluids A, 4, 306-320.

Lane, S. N., Biron, P. M., Bradbrook, K. F., Butler, J. B., Chandler, J. H., Crowell, M. D., McLelland, S. J., Richards, K. S. and Roy, A. G. (1998). Three-Dimensional Measurement of River Channel Flow Processes Using Acoustic Doppler Velocimetry. Earth Surface Processes and Landforms, 23, 1247-1267.

Launder, B. E. and Sharma, B. I. (1974). Application of the Energy-Dissipation Model of Turbulence to the Calculation of Flow Near a Spinning Disc. Letters in Heat and Mass Transfer, 1, 131-137.

Launder, B. E. and Spalding, D. B. (1972). Lectures in Mathematical Models of Turbulence. Academic Press, London.

Launder, B. E. and Spalding, D. B. (1974). The Numerical Computation of Turbulent Flows. Computer Methods in Applied Mechanics and Engineering, 3, 269-289.

Levenspiel, O. (1999). Chemical Reaction Engineering. 3rd ed., John Wiley & Sons, New York.

Lin, B. and Falconer, R. A. (1997). Three-Dimensional Layer-Integrated Modelling of Estuarine Flows with Flooding and Drying. Estuarine, Coastal and Shelf Science, 44, 737-751.

Lohrmann, A., Cabrera, R. and Kraus, N. C. (1994). Acoustic-Doppler Velocimeter (ADV) for Laboratory Use. Proceedings of Fundamentals and Advancements in Hydraulic Measurements and Experimentation. Buffalo, USA.

Lohrmann, A., Cabrera, R., Gelfenbaum, G. and Haines, J. (1995). Direct Measurements of Reynolds Stress with an Acoustic Doppler Velocimeter. Proceedings of the IEEE 5th Working Conference on Current Measurement. St. Petersburg, USA.

Louie, D. S. and Fohrman, M. S. (1968). Hydraulic Model Studies of Chlorine Mixing and Contact Chambers. Journal of the Water Pollution Control Federation, 40, 2, 1, 174-184.

Marske, D. M. and Boyle, J. D. (1973). Chlorine Contact Chamber Design – a Field Evaluation. Water and Sewage Works, 120,1, 70-77.

Moffatt, H. K. (1963). Viscous and Resistive Eddies Near a Sharp Corner. Journal of Fluid Mechanics, 18, 1-18.

Lyn, D. A. and Rodi, W. (1990). Turbulence Measurements in Model Settling Tank. J. of Environmental Engineering, ASCE, 116, 1, 3-21.

Marske, D. A. and Boyle, J. D. (1973). Chlorine Contact Tank Design – a Field Evaluation. Water and Sewage Works, 71-77.

Martin, V., Fisher, T. S. R., Millar, R. G. and Quick, M. C. (2002). ADV Data Analysis for Turbulent Flows: Low Correlation Problem. Proceedings of the ASCE Specialty Conference on Hydraulic Measurements and Experimental Methods. Estes Park, USA.

McDonald, J. W., Denny, V. E. and Mills, A. F. (1972). Numerical Solutions of the Navier-Stokes Equations in Inlet Regions. Journal of Applied Mechanics, ASME, 12, 873-878.

McLelland, S. J. and Nicholas, A. P. (2000). A New Method for Evaluating Errors in High-Frequency ADV Measurements. Hydrological Processes, 14, 351-366.

McNaughton, J. C. and Gregory, R. (1977). Disinfection by Chlorination in Contact Tanks. Technical Report TR60, Water Research Centre, UK.

Nezu, I. and Rodi, W. (1986). Open-Channel Flow Measurements With a Laser Doppler Anemometer. Journal of Hydraulic Engineering, ASCE, 112, 5, 335-335.

Nikora, V. I. and Goring, D. G. (1998). ADV Measurements of Turbulence: Can We Improve Their Interpretation. Journal of Hydraulic Engineering, ASCE, 124, 6, 630-634.

Nortek-AS (1997a). ADV Operation Manual.

Nortek-AS (1997b). ADV Software Manual.

Nortek-AS (2004). [WWW] <URL http://www.nortek-as.com/hardware/velo_ndv.php> [Accessed 15/03/04]

Olsen, N. R., Hedger, R. D. and George, D. G. (2000). 3D Numerical Modeling of Microcystis Distribution in a Water Reservoir. Journal of Environmental Engineering, ASCE, 126, 10, 949-953.

Patankar, S. V. (1980). Numerical Heat Transfer and Fluid Flow. Hemisphere, New York.

Patankar, S. V. (1981). A Calculation Procedure for Two-Dimensional Elliptic Situations. Numerical Heat Transfer, 4, 409-425.

Patankar, S. V. and Spalding, D. B. (1972). A Calculation Procedure for Heat, Mass and Momentum Transfer in Three-Dimensional Parabolic Flows. International Journal of Heat and Mass Transfer, 15, 1787-1972.

Patel, V., Rodi, W. and Scheuerer, G. (1985). Turbulence Models for Near-Wall and Low Reynolds Number Flows: a Review. American Institute of Aeronautics and Astronautics Journal, 23, 9, 1308-1319.

Peplinski, D. K. and Ducoste, J. J. (2002). Modeling of Disinfection Contactor Hydraulics Under Uncertainty. Journal of Environmental Engineering, ASCE, 128, 11, 1056-1067.

Rauen, W. B. (2001). Effects of Scale and Discharge on the Dynamic Similitude and Chlorine Disinfection Efficiency of Scaled-Down Models of Contact Tanks. M.Sc. Dissertation, Department of Environmental Engineering, UFES, Vitória, Brasil (in Portuguese).

Revstedt, J., Fuchs, L. and Trägardh, C. (1998). Large Eddy Simulations of the Turbulent Flow in a Stirred Reactor. Chemical Engineering Science, 53, 24, 4041-4053.

Roache, P. J. (1998). Fundamentals of Computational Fluid Dynamics. Hermosa Publishers, New York.

Rodi, W. (1993). Turbulence Models and Their Application in Hydraulics – A State-of-the-Art Review. 3rd ed., A.A.Balkema, Rotterdam / Brookfield.

Rodi, W., Ferziger, J. H., Breuer, M. and Pourquié, M. (1997). Status of Large Eddy Simulation: Results of a Workshop. Journal of Fluids Engineering, ASME, 119, 248-262.

Rokni, M., Olsson, C.-O. and Sundén, B. (1998). Numerical and Experimental Investigation of Turbulent Flow in a Rectangular Duct. International Journal for Numerical Methods in Fluids, 28, 225-242.

Roy, A. G., Biron, P. M. and Lapointe, M. F. (1997). Implications of Low-Pass Filtering on Power Spectra and Autocorrelation Functions of Turbulent Velocity Signals. Mathematical Geology, 29, 5, 653-668.

Sawyer, C. M. and King, P. H. (1969). The Hydraulic Performance of Chlorine Contact Tanks. Proceedings of the 24th Industrial Waste Conference, Purdue University, West Lafayette, USA.

Schlichting, H. (1979). Boundary-Layer Theory. 7th ed., McGraw-Hill, New York.

Sengupta, S. (1977). A Three-Dimensional Rigid-Lid Model for Closed Basins. Journal of Heat Transfer, ASME, 99, 11, 656-662.

Sepp, E. (1981). Optimisation of Chlorine Disinfection Efficiency. Journal of Environmental Engineering, ASCE, 107, 1, 139-153.

Shiono, K. and Teixeira, E. C. (2000). Turbulent Characteristics in a Baffled Contact Tank. Journal of Hydraulic Research, 38, 6, 403-416.

Shiono, K., Scott, C. F. and Kearney, D. (2003). Predictions of Solute Transport in a Compound Channel Using Turbulence Models. Journal of Hydraulic Research, 41, 3, 247-258.

Siqueira, R. N. (1998). Development and Refinement of Criteria to the Assessment of the Hydraulic Efficiency and Determination of the Mixing Coefficient of Water and Wastewater Treatment Units. M.Sc. Dissertation, Department of Environmental Engineering, UFES, Vitória, Brazil (in Portuguese).

Smart, P. L. and Laidlaw, I. M. S. (1977). An Evaluation of Some Fluorescent Dyes for Water Tracing. Water Resources Research, 13, 1, 15-33.

Song, T. and Chiew, Y. M. (2001). Turbulence Measurement in Non-Uniform Open-Channel Flow Using Acoustic Doppler Velocimeter (ADV). Journal of Engineering Mechanics, ASCE, 127, 3, 219-232.

SonTek (2004). [WWW] <URL http://www.sontek.com/princop/adv/advpo.htm> [Accessed 18/03/04]

Speziale, C. G. (1987). On Non-Linear k-l and k-ε Models of Turbulence. Journal of Fluid Mechanics, 178, 459-475.

Stamou, A. I. (2002). Verification and Application of a Mathematical Model for the Assessment of the Effect of Guiding Walls on the Hydraulic Efficiency of Chlorination Tanks. Journal of Hydroinformatics, 4, 4, 245-254.

Stamou, A. I. and Adams, E. W. (1988). Study of the Hydraulic Behaviour of a Model Settling Tank Using Flow-Through Curves and Flow Patterns. Report no. SFB 210/E/36, University of Karlsruhe, Karlsruhe, Germany.

Stern, F., Wilson, R. V., Coleman, H. W. and Paterson, E. G. (2001). Comprehensive Approach to Verification and Validation of CFD Simulations – Part I: Methodology and Procedures. Journal of Fluids Engineering, ASME, 123, 793-802.

Stevenson, D. G. (1995). The Design of Disinfection Contact Tanks. Journal of the Chartered Institution of Water and Environmental Management, 9, 4, 146-152.

Tannehill, J. C., Anderson, D. A. and Pletcher, R. H. (1997). Computational Fluid Mechanics and Heat Transfer. Hemisphere, New York.

Teixeira, E. C. (1993). Hydrodynamic Processes and Hydraulic Efficiency of Chlorine Contact Units. Ph.D. Thesis, Department of Civil Engineering, University of Bradford, UK.

Teixeira, E. C. (1995). Improvement of the Hydraulic Performance of a Chlorine Contact Unit by Means of Cross-Baffling. International Symposium on Technology Transfer – IAWQ/ABES, Salvador, Brasil.

Teixeira, E. C. and Siqueira, R. N. (2005). Performance Assessment of Hydraulic Efficiency Indexes. Journal of Environmental Engineering, ASCE (submitted for publication).

Teixeira, E. C., Siqueira, R. C. N. and Rauen, W. B. (2002). Automation of Acquisition and Processing of Flow-Through Curves. Proceedings of the 5th International Conference on Hydroinformatics, Cardiff, UK.

Teixeira, E. C., Chacaltana, J. T. A., Pacheco, C. G. and Siqueira, R. N. (2004). Use of Flow-Though Curves to Calibrate and Validate Numerical Models of Solute Transport in Contact Tanks. Proceedings of the 6th International Conference on Hydroinformatics, Suntec City, Singapore.

Thackston, E. L., Shields, F. D. and Schroeder, P. R. (1987). Residence Time Distributions of Shallow Basins. Journal of Environmental Engineering, ASCE, 113, 6, 1319-1332.

Thayanithy, M. (1984). Hydraulic Design Aspects of Chlorine Contact Tank. M.Sc. Dissertation, Department of Civil Engineering, University of Birmingham, UK.

Thirumurthi, D. (1969). A Break-Through in Tracer Studies in Sedimentation Tanks. Journal of the Water Pollution Control Federation, 41, 11, R405-R418.

Trussell, R. R. and Chao, J. L. (1977). Rational Design of Chlorine Contact Facilities. Journal of the Water Pollution Control Federation, 49, 4, 659-667.

Turner Designs (1998). Digital Fluorometer AU-10 Manual.

UN (1997). Comprehensive Assessment of the Freshwater Resources of the World. Report of the Secretary General, United Nations Economic and Social Council. [WWW] <URL http://www.un.org/esa/documents/ecosoc/cn17/1997/ecn171997-9.htm> [Accessed 15/03/04]

UNESCO (2003). Water for People, Water for Life: Executive Summary. The United Nations World Water Development Report. [WWW] <URL http://unesdoc.unesco.org/images/0012/001295/129556e.pdf> [Accessed 15/03/04]

van Doormaal, J. P. and Raithby, G. D. (1984). Enhancements of the SIMPLE Method for Predicting Incompressible Fluid Flows. Numerical Heat Transfer, 7, 147-163.

van Driest, E. R. (1956). On Turbulent Flow Near a Wall. Journal of the Aeronautical Sciences, 11, 1007-1036.

Versteeg, H. K. and Malalasekera, W. (1995). An Introduction to Computational Fluid Dynamics: the Finite Volume Method. Longman Scientific and Technical, Essex, UK.

Voulgaris, G. and Trowbridge, J. H. (1998). Evaluation of the Acoustic Doppler Velocimeter (ADV) for Turbulence Measurements. Journal of Atmospheric and Oceanic Technology, 15, 272-289.

Wahl, T. (2000). Analysing ADV Data Using WinADV. Proceedings of the Joint Conference on Water Resources Engineering and Water Resources Planning and Management. Minneapolis, USA.

Wang, H. (1995). Numerical Modelling of Flow and Disinfection Processes in Chlorine Contact Tanks. Ph.D. Thesis, Department of Civil Engineering, University of Bradford, UK.

Wang, H. and Falconer, R. A. (1998a). Numerical Modelling of Flow in Chlorine Disinfection Tanks, Journal of Hydraulic Engineering, ASCE, 124, 9, 918-931.

Wang, H. and Falconer, R. A. (1998b). Simulating Disinfection Processes in Chlorine Contact Tanks Using Various Turbulence Models and High-Order Accurate Difference Schemes. Water Research, 32, 5, 1529-1543.

Wehner, J. F. and Wilhelm, R. H. (1956). Boundary Conditions of Flow Reactor. Chemical Engineering Science, 6, 89-93.

White, G. C. (1998). Handbook of Chlorination and Alternative Disinfectants. 4th ed., John Wiley & Sons, New York.

WHO (2004). Guidelines for Drinking-Water Quality. Vol. 1, 3rd ed., World Health Organization. [WWW] <URL: http://www.who.int/water_sanitation_health/dwq/ GDWQ2004web.pdf> [Accessed 15/03/04]

WHO/UNICEF (2000). Global Water Supply and Sanitation Assessment Report. World Health Organization and United Nations Children's Fund. [WWW] <URL http://www.who.int/docstore/water_sanitation_health/Globassessment/Globaltoc.htm > [Accessed 15/03/04]

Wilcox, D. C. (1998). Turbulence Modeling for CFD. Birmingham Press, San Diego.

Wu, W., Rodi, W. and Wenka, T. (2000). 3D Numerical Modeling of Flow and Sediment Transport in Open Channels. Journal of Hydraulic Engineering, 126, 1, 4-15.